



**UNIVERSITÀ DEGLI STUDI DI MILANO-BICOCCA**

FACOLTÀ DI SCIENZE MATEMATICHE, FISICHE E NATURALI

CORSO DI LAUREA MAGISTRALE IN FISICA

Dipartimento di fisica G. Occhialini

*with*

**CERN, EP-DT-FS group**

---

**Characterization of RPC detectors operated with new eco friendly gas mixtures**

---

*Author:*

**Demetrio MAGATTI**

*Supervisor:*

**Dott. Gabriele CROCI**

**Dott. Beatrice MANDELLI**

**Dott. Enrico PERELLI**

March 31, 2021





**Characterization of RPC detectors operated with new eco friendly gas mixtures**

by Demetrio MAGATTI

**Abstract**

Resistive plate Chambers (RPCs) are gaseous particle detectors widely used at CERN LHC experiments thanks to their excellent time resolution and production cost. They are operated with a Freon-based gas mixture containing  $C_2H_2F_4$  and  $SF_6$ , both greenhouse gases (GHG) with a high Global Warming Potential (GWP) and therefore subject to European regulations aiming at reducing the GHG emissions. The search for new environmentally friendly gas mixtures that are compatible with the current ATLAS and CMS RPC systems is therefore determined by the need of lowering GHG emissions and, obviously, of finding alternatives to gases that could disappear in the future. The goal of this work is to characterize the RPC performance using low GWP mixtures. In the first part of the work,  $C_2H_2F_4$  was partially replaced either by inert gases or by  $C_3H_2F_4$  (also known as R-1234ze), a gas in the family of the HydroFluoroOlefin (HFO), which has already been identified by the refrigerant industry as a suitable low GWP alternative to the R-134a. Recently developed high electronegativity and electrically insulating gases, 3M<sup>TM</sup> Novec<sup>TM</sup> 4710 and 3M<sup>TM</sup> Novec<sup>TM</sup> 5110, were tested as  $SF_6$  replacements. Several gas mixtures were tested in laboratory conditions using cosmic muons, and the obtained results were compared to the standard gas mixture currently used at CMS and ATLAS experiment ( $C_2H_2F_4/i-C_4H_{10}/SF_6$  95.2/4.5/0.3). Novec gases have proven to be promising alternatives to  $SF_6$ . The second part of this work is related to long term tests and validation of low GWP gas mixtures for RPC detectors under irradiation condition at the CERN Gamma Irradiation Facility (GIF++), where a 12.2 TBq  $^{137}Cs$  source provides an irradiation background similar to the one foreseen for the High Luminosity LHC (HL-LHC) phase. The RPC detectors under irradiation were kept at the working point in order to investigate the performance stability over time. The gas mixture which underwent the validation test was a five components mixture where part of the  $C_2H_2F_4$  has been replaced by R-1234ze and Helium ( $C_2H_2F_4/HFO/He/iC_4H_{10}/SF_6$  37.45/37.45/20/4.5/0.6). Currents measured at the gas mixture's working point were approximately larger by a factor two with respect to the standard gas mixture, but they showed good stability over a six-month operation period. Long term performance studies were started and are being carried on.





---

# Contents

<b>1 High Energy Physics at the Large Hadron Collider</b>	<b>1</b>
1.1 CERN and the LHC . . . . .	1
1.2 Physics and the LHC . . . . .	3
1.2.1 Standard Model physics . . . . .	3
1.2.2 The Higgs boson at the LHC . . . . .	4
1.2.3 Physics beyond the standard model . . . . .	4
1.2.4 Other Physics at the LHC . . . . .	5
1.3 Muon Detector Systems at the LHC Experiments . . . . .	5
1.3.1 Gas Systems for Muon Detectors . . . . .	6
1.4 Detector upgrades for HL-LHC . . . . .	7
1.4.1 Motivation for Muon Detector Systems upgrade . . . . .	8
1.4.2 Examples of Muon Systems Optimization . . . . .	9
1.5 Greenhouse gases at the LHC . . . . .	10
1.5.1 Greenhouse effect . . . . .	10
1.5.2 Greenhouse gases and Global Warming Potential . . . . .	11
1.6 RPCs and the GHGs . . . . .	11
<b>2 The RPC detector</b>	<b>13</b>
2.1 Historical developments . . . . .	13
2.1.1 General description of an RPC . . . . .	13
2.2 Detection principles . . . . .	14
2.2.1 Charge multiplication . . . . .	14
2.2.2 Raether limit . . . . .	15
2.2.3 Statistical fluctuation of the avalanche charge . . . . .	15
2.2.4 Multiple clusters formation . . . . .	16
2.2.5 Total developed charge . . . . .	17
2.2.6 Signal formation on the readout strips . . . . .	17
2.2.7 Avalanche and streamer modes . . . . .	17
2.3 Foremost parameters . . . . .	18
2.3.1 Charge distribution . . . . .	18
2.3.2 Efficiency . . . . .	19
2.3.3 Time resolution . . . . .	19
2.3.4 Gas mixture . . . . .	19
2.3.5 Bulk resistivity . . . . .	21
2.4 Pressure and temperature effects . . . . .	21
2.5 Electrical scheme . . . . .	21
2.6 Model for RPC detectors operating at high rate . . . . .	22
<b>3 Gas related studies on RPC detectors</b>	<b>23</b>
3.1 Experiment goals and experimental setup . . . . .	23
3.1.1 Gas supplying system . . . . .	23
3.1.2 RPC gap, trigger and readout systems . . . . .	24
3.2 Single strip Analysis procedure . . . . .	24
3.3 Signal processing . . . . .	25
3.3.1 Charge development . . . . .	25
3.4 Analyzed data structure . . . . .	26

3.5 Multi strip analysis . . . . .	26
3.6 Height spectrum . . . . .	27
3.7 Charge spectrum . . . . .	27
3.7.1 Charge-based avalanche/streamer discrimination . . . . .	28
3.7.2 Describing the charge distribution . . . . .	29
3.8 Cluster size . . . . .	30
3.9 Time resolution . . . . .	30
3.10 Efficiency . . . . .	31
3.11 Streamer probability . . . . .	31
3.12 Fit of the efficiency curve . . . . .	32
3.13 Full run results . . . . .	33
<b>4 RPC performance with eco friendly gas mixtures</b>	<b>35</b>
4.1 Novec4710 . . . . .	35
4.1.1 Efficiency and streamer probability . . . . .	35
4.1.2 Collected charge . . . . .	36
4.1.3 Cluster size and time resolution . . . . .	37
4.1.4 Summary . . . . .	38
4.2 Novec5110 . . . . .	39
4.2.1 Efficiency and streamer probability . . . . .	39
4.2.2 Charge distribution . . . . .	40
4.2.3 Cluster size and time resolution . . . . .	41
4.2.4 Summary . . . . .	42
4.3 EcoHe mixtures . . . . .	43
4.3.1 Efficiency and streamer probability . . . . .	43
4.3.2 Collected charge . . . . .	44
4.3.3 Cluster size and time resolution . . . . .	44
4.3.4 Summary . . . . .	45
<b>5 The Gamma Irradiation Facility (GIF++)</b>	<b>46</b>
5.1 Historical background . . . . .	46
5.2 Gamma irradiation field . . . . .	47
5.3 Experiment goals and experimental setup . . . . .	47
5.4 Effective attenuation . . . . .	49
5.5 RPC detectors in gamma irradiation condition . . . . .	50
5.5.1 Definitions . . . . .	51
5.5.2 Detector resistance measure . . . . .	51
5.5.3 The $R \cdot I$ drop . . . . .	52
5.5.4 EcoHe20 mixture . . . . .	53
5.6 Performance stability . . . . .	55
5.7 Source ON - detector ON - ABS 2.2 . . . . .	55
5.7.1 Shadowing from other setups . . . . .	56
5.7.2 Environmental effects . . . . .	57
5.7.3 Current stability - RPC2 . . . . .	58
5.7.4 Current stability - RPC0 . . . . .	58
5.8 Performance stability - source OFF . . . . .	59
5.8.1 Ohmic current . . . . .	60
5.8.2 Physics current . . . . .	60





# HIGH ENERGY PHYSICS AT THE LARGE HADRON COLLIDER

## 1.1 CERN and the LHC

The Large Hadron Collider (LHC) is a two-ring superconducting hadron accelerator and collider at the European Organization for Nuclear Research (*Conseil Européen pour la Recherche Nucléaire*, CERN). Made of 27km of superconducting magnets, laying 100 meters underground, it allows the confinement and acceleration of two proton beams, running in opposite directions. It has been designed to provide enough statistics to fulfil the requirements of the CERN physics program, oriented to studies on the Standard Model as well as to the search of new physics. The LHC can nominally provide a center of mass energy of 14 TeV for proton-proton collisions, created by 2808 bunches containing  $1.15 \cdot 10^{11}$  particles each, with a bunch spacing of 25 ns. The design luminosity of the collider is of  $1 \cdot 10^{34} \text{cm}^{-2} \text{s}^{-2}$ . Primary protons are obtained from Helium, and they are accelerated in a first linear collider (LINAC) and then injected in the chain of circular accelerators that allows the achievement of their maximum energy (13 TeV). Protons pass through the Proton Synchrotron (PS, 25GeV), the Super Proton Synchrotron (SPS, 450GeV) and finally are injected in the LHC (Figure (1.1)).

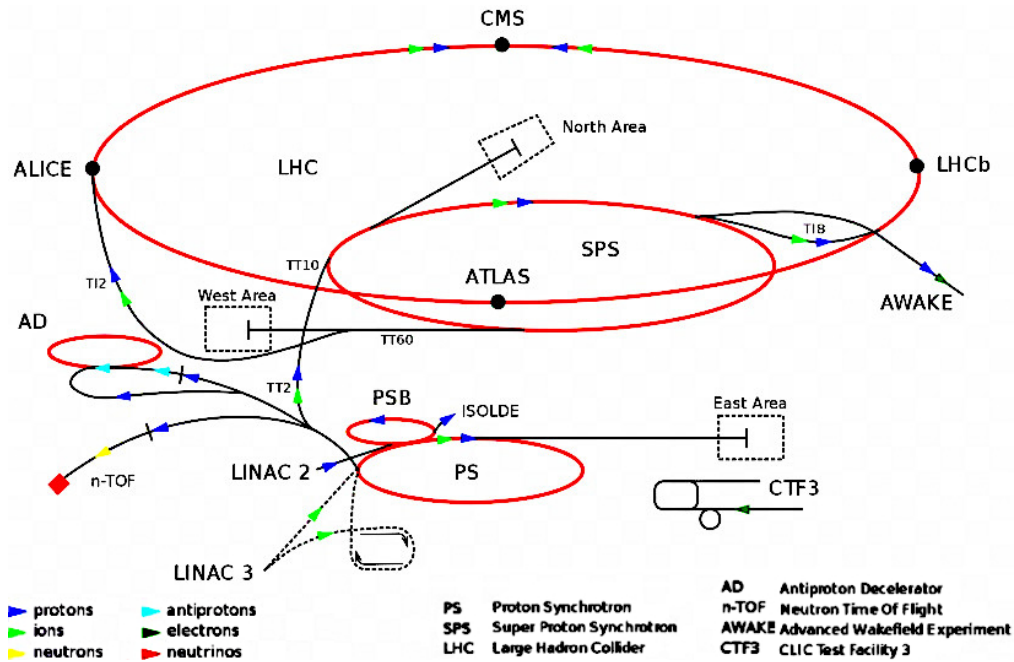


Figure 1.1: LHC Accelerator Complex layout [1].

The particle beams are guided by 1232 superconducting magnets that can produce a maximum magnetic field of about 8.3 T. The protons are accelerated with radio frequency cavities, designed with particular size and shape so that the electromagnetic waves inside them become resonant and invert their direction of propagation with a frequency of 400 MHz. As a result, the oscillation field keeps the beam separated into discrete bunches.

Four experiments were designed and built to completely exploit the physics program for proton collisions. They are located at the four LHC's interaction points, in which the actual collisions happen. Two general purpose experiments, ATLAS (A Toroidal LHC ApparatuS) and CMS (Compact Muon Solenoid), were designed to explore all the possible aspects of the LHC physics, from heavy-ions collisions and forward physics, to Higgs boson physics and direct search of new particles. Specially dedicated to heavy-ions physics is the ALICE experiment (A Large Ion Collider Experiment), while the LHCb aims to maximize the LHC potential in beauty and charm physics. Though the final purpose is specific for each experiment, the requirements on the detectors of which they are composed of are quite the same: capability of identifying charged particles and measuring particles momentum with high resolution, high granularity in order to reduce the possibility of overlapping events, fast and radiation-tolerant electronics for proper data acquisition.

LHC experiments can be described by dividing their structure into three different areas (CMS detector structure reported in Figure (1.2) as an example):

- **inner detectors** are located close to the collision points, and allow tracking and momentum measurement of charged particles, as well as vertices reconstruction;
- **hadronic and electromagnetic calorimeters** measure the energy of hadrons, photons and electrons by measuring their energy loss inside the detectors;
- **muon systems** are dedicated to detecting muons, which escape electromagnetic calorimeter. Placed at the outermost layers of the experiments, the muon system allows to unambiguously detect the signature of many relevant events.

Although the four experiments have significantly different goals, they all rely on gaseous detectors for muon detection and tracking.

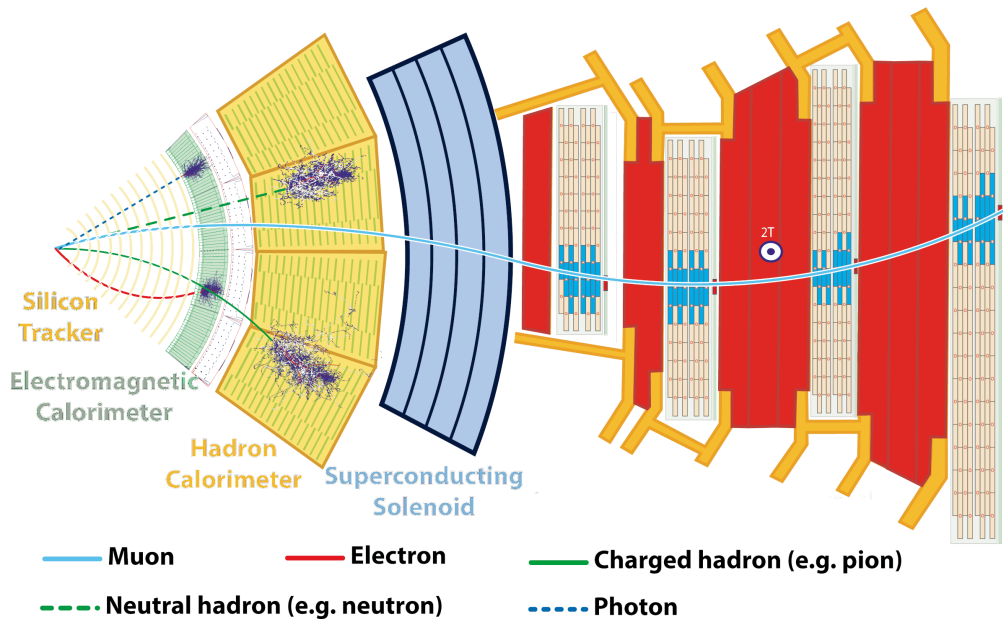


Figure 1.2: Transverse section of the CMS detector [2].

## 1.2 Physics and the LHC

### 1.2.1 Standard Model physics

The Standard Model (SM) physics finds its roots in the early sixties, when the Quark Model was put beside the already known leptonic side of the elementary particles picture. In its complete formulation, the SM combines special relativity and quantum mechanics, through a gauge theory based on symmetry groups. Fundamental constituents of matter are spin-1/2 particles, the so called fermions. Fermions are again divided into quarks and leptons, each composed of three different families (Figure (1.3)). For each fermion, a correspondent anti-particle exists, with opposite quantum numbers.

		Lepton classification					Quark classification							
		$l$	$Q$	$L_e$	$L_\mu$	$L_\tau$	$q$	$Q$	$D$	$U$	$S$	$C$	$B$	$T$
First generation	$e$	$-1$	$1$	$0$	$0$	$0$	$d$	$-1/3$	$-1$	$0$	$0$	$0$	$0$	$0$
	$\nu_e$	$0$	$1$	$0$	$0$	$0$	$u$	$2/3$	$0$	$1$	$0$	$0$	$0$	$0$
Second generation	$\mu$	$-1$	$0$	$1$	$0$	$0$	$s$	$-1/3$	$0$	$0$	$-1$	$0$	$0$	$0$
	$\nu_\mu$	$0$	$0$	$1$	$0$	$0$	$c$	$2/3$	$0$	$0$	$0$	$1$	$0$	$0$
Third generation	$\tau$	$-1$	$0$	$0$	$0$	$1$	$b$	$-1/3$	$0$	$0$	$0$	$0$	$-1$	$0$
	$\nu_\tau$	$0$	$0$	$0$	$0$	$1$	$t$	$2/3$	$0$	$0$	$0$	$0$	$0$	$1$

Figure 1.3: Standard Model classification of fermions in their three generations [3].

Fermions interact among them through the exchange of spin-1 particles, the gauge bosons, which are elementary particles themselves. Their presence arises from the invariance of the SM theory under gauge symmetries. Each of the fundamental interactions is described with a different gauge group and different mediators:

- **Electromagnetic Interaction** is described by the **Quantum Electro-Dynamics (QED)** and it is mediated by the photon, a massless boson. It is associated with a  $U(1)$  symmetry, since there is a single gauge boson and only one quantum number, the electromagnetic charge  $Q$ ;
- **Weak Interaction** is mediated by the massive  $W^\pm$  and  $Z^0$  bosons, and it is described with the symmetry groups  $SU(2)$ . It involves all elementary particles and it is the only interaction during which quarks' flavour change is allowed;
- **Strong Interaction**, described by the **Quantum Chromo-Dynamics (QCD)**, is associated with the symmetry group  $SU(3)$ , which describes the colour symmetry. Only quarks take part in QCD interactions, since leptons are colorless.

Weak and Electromagnetic interactions were unified in 1963 with the ElectroWeak theory, accomplished under a  $SU(2) \times U(1)$  group. Nonetheless, all mediators foreseen by the first ElectroWeak model were massless. Being this far from the already proved physics at the time, a new mechanism was proposed in 1964 to introduce the mass of the exchange bosons. The mechanism, known as the Higgs mechanism, was developed by F. Englert and P. Higgs, and it was worth the Physics Nobel Prize in 2013. The mechanism foresees an extra fundamental particle, the Higgs boson, whose interaction with ordinary particles generates their own masses. The fact that  $W^\pm$  and  $Z^0$  bosons are massive particles, while the photon is massless, invariably requires the Higgs mechanism to break the ElectroWeak symmetry, with the direct consequence of the existence of a new spin-0 boson. The mass of such boson is however an open parameter of the theory.

### 1.2.2 The Higgs boson at the LHC

In the first three-years physics run of the LHC (2010-2013) results were highly remarkable. The LHC has been operated at up to 8 TeV of center of mass energy, delivering about  $25 \text{ fb}^{-1}$  with a peak luminosity of  $7.7 \cdot 10^{33} \text{ cm}^{-2} \text{ s}^{-1}$  (in ATLAS and CMS). Within several physics results, the major achievement was undoubtedly the observation of a new particle, with a mass of 126 GeV and Higgs-like properties. The discovery came from both ATLAS and CMS experiments, which identified the new particle as the Standard Model Higgs boson.

The channels with the strongest Higgs sensitivity at the LHC are the vector boson fusion and gluon-fusion, while the most significant decay processes are the di-photon, the ZZ to four leptons and the leptonic WW channels. For both experiments, the most relevant results were obtained in the ZZ and di-photon channels, which allowed the measurement of the Higgs boson mass with a very high precision (0.43% and 0.34% for ATLAS and CMS respectively). The discovery was determined by the 5-standard-deviation significance of the deviation from the background-only hypothesis in the cited channels. As it can be seen by looking at the invariant mass distribution of di-photon events from CMS events analysis (Figure (1.4), left), an excess can clearly be seen at the mass value of 126 GeV. Similarly, the signal excess can be seen in the invariant mass distribution of four lepton events from the double Z decay, measured by the ATLAS experiment (Figure (1.4), right).

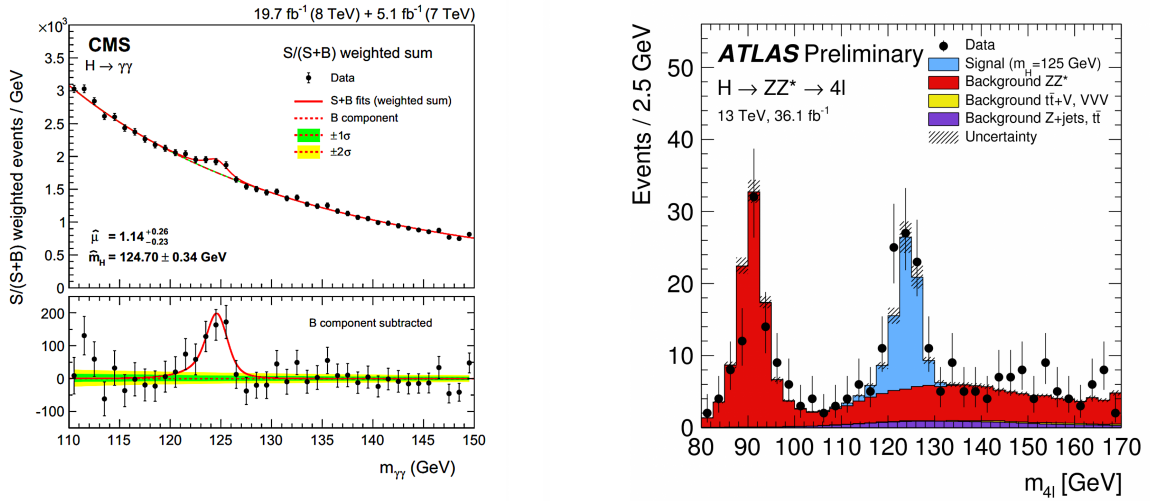


Figure 1.4: Invariant mass distribution of a di-photon event (left) and of a four lepton event (right), detected from CMS and ATLAS experiments respectively.

Being this discovery of fundamental importance for the Standard Model, part of the future LHC program will be focused on measurements of the properties of the Higgs boson. This implies studies to test the Standard Model pattern of its coupling to elementary particles, as well as searches for additional Higgs bosons. As a matter of facts, the capability of the LHC to reach a center of mass energy of 14 TeV, delivering an integrated luminosity of  $3000 \text{ fb}^{-1}$  by 2030, will lead to the possibility of pushing further the studies on the Higgs boson itself, as well as a variety of other matters in which the new particle is involved. Besides, off-shell and high transverse momentum Higgs production will allow access to new physics near the TeV scale that may otherwise be hidden. Finally, the Higgs self-coupling process will possibly be investigated, leading to the crucial test on whether its potential is the one associated with the actual vacuum, as its field properties seem to suggest.

### 1.2.3 Physics beyond the standard model

Notwithstanding the Standard Model having been successfully tested in the last decades, it presents numerous lacks on fundamental questions in particle physics. As an example, forces unification, hierarchy problem of the Fermi



scale as well as dark matter and antimatter issues are still unresolved. This leads to the thinking that the Standard Model may only be a low energy effective theory. Several theories have been proposed, such as the extension of the SM in the **Super Symmetry** (SUSY) theory, which foresees a symmetry between fermions and bosons. It potentially offers elegant solutions to many of the SM shortcomings, but as of today, there are not evidences of SUSY particles. Beyond Standard Model theories are an open scenario, for which future LHC period at higher luminosity (HL-LHC) will be essential.

#### 1.2.4 Other Physics at the LHC

In parallel to Higgs and new physics searches, flavour and heavy ions physics is of fundamental importance in the LHC physics program. Flavor physics studies are lead by the dedicated LHCb experiment, which accomplished notable results during the first run. The very rare decay  $B_s^0 \rightarrow \mu^+ \mu^-$  was observed, with a branching ratio extremely consistent with the one calculated with the SM theory. Moreover, the first experimental evidence of direct CP violation was observed in  $B_s^0$  decays. LHCb will then be the leading experiment for a wide range of important observables concerning rare decays and CP violation in charm and beauty hadrons.

Furthermore, very successful PbPb and pPb runs brought unprecedented results in heavy-ion physics, such as the detailed studies of jet quenching in PbPb collisions and di-jet production in pPb collisions. Involved experiments are ATLAS, ALICE and CMS, that will have in the future a significant role in the studies of heavy-flavour particles, quarkonium states and many others.

### 1.3 Muon Detector Systems at the LHC Experiments

As mentioned before, each LHC experiment is equipped with a Muon Detector System. Muon detection is fundamental for a complete identification and characterization of collisions, since muons represent a very clean probe for many events of interest. In addition, they can provide trigger and veto for event selection. With a mass of 105.6 GeV, muons can quite easily penetrate matter and therefore they escape electromagnetic calorimeters. Muon systems are then made of dedicated detectors, capable of identifying and tracking these particles. A brief summary of the Muon System of each LHC experiment is here reported, followed by the description of how their infrastructure is sustained.

#### LHCb

LHCb is a single-arm spectrometer with a forward angular coverage from 10 mrad to 300 mrad in the bending plane, to best exploit the statistics of the  $b$  and  $\bar{b}$  production, which predominantly happens in the same forward or backward region. The muon detection system is fundamental in the LHCb since muons are present in the final states of many CP-sensitive decays. They provide a tag of the initial state flavor of the accompanying neutral B mesons for semi-leptonic decays. The muon system is here mainly composed of **Multi Wire Proportional Chambers** (MWPC), except for the high rate region, where **Gas Electron Multipliers** (GEM) are used. It is divided into five rectangular stations, along the beam axis, with a total of 1380 chambers covering an area of 435 m<sup>2</sup>. GEMs are located in the inner region, where the expected particle rate would not be sustained by MWPCs due to ageing safety limits. Lastly, the outmost layer hosts the Outer Tracker, a gaseous detector that covers approximately a 30 m<sup>2</sup> area with twelve double layers of straw tubes.

#### CMS

The CMS experiment structure is based on a super-conducting solenoid, that produces a 3.8 T magnetic field: the tracker, the electromagnetic and hadronic calorimeters are located within the field volume. The iron yoke is equipped with a muon spectrometer for identification, triggering and momentum measurement. The system is divided into five separate wheels in the barrel, with four concentric layers of detectors. Both the positive and negative

endcaps are instead instrumented with four independent disks. Three different gaseous detector technologies are employed. In the barrel region, **Drift Tubes (DT)** are used to detect muons up to pseudo-rapidity  $|\eta| < 1.2$ . **Cathode Strip Chambers (CSC)** located in the endcap region ( $0.9 < |\eta| < 2.4$ ) allow the handling of higher rates and non-uniform magnetic field. Lastly, **Resistive Plate Chambers (RPC)** are employed in both barrel and endcap region ( $|\eta| < 1.6$ ).

### ATLAS

The physics program of the ATLAS experiment requires high performance over the large range in transverse momentum. Its muon system includes three large super-conducting air-core toroids, precision tracking chambers for accurate momentum resolution, and an effective trigger system. The latter is realized with two different detector technologies: **RPCs** are used in the barrel, with two layers of chambers installed in the middle station and a third layer on the outer chamber station. The endcap trigger system is instead composed of **Thin Gap Chambers (TGC)**, multi-wire chambers operated in saturated mode. Three multi layers are located in the middle tracking station, while some others are part of the inner station. Precise  $p_T$  measurements are instead made possible by **Monitored Drift Tubes (MDT)**. They can in fact sustain high rates without ageing with little sensitivity to space charge. Their surface can reach  $10 \text{ m}^2$ , requesting an extremely accurate mechanical construction to best exploit their tracking accuracy. Moreover, the use of **CSCs** in the inner station of the end-cap allows to have optimal performances regardless the high background rate in this region.

### ALICE

Being ALICE experiment fully dedicated to heavy ion physics, its muon spectrometer needs to measure very low  $p_T$  in a large rapidity range ( $-4 < |\eta| < -2.5$ ). Its tracking system is made of five stations with two detector planes each, consisting of cathode pad chambers. These detectors are multi-wire proportional chambers with a segmented cathode plane. Different pad densities are present, depending on the station position with regard to the pseudo-rapidity. The system is also capable of high efficient triggering, with four planes of 18 **RPCs**, operating in streamer mode. They are located at approximately 20 m from the Interaction Point, and deliver online information to the central trigger processor.

#### 1.3.1 Gas Systems for Muon Detectors

Regardless the location and scope of each gas detector inside LHC experiments, the most critical of the infrastructures is their gas distribution system. Indeed, the gas mixture is a fundamental parameter for detector operation and safety for both short and long term periods. A total of 30 dedicated gas systems deliver the proper gas mixture to corresponding detectors. Their extension can reach several hundreds of meters and they are subject to severe requirements on design and components quality to guarantee good and safe long-term detector operation. High reliability is needed in terms of both stability and quality of the gas mixture, since it is the primary element influencing detector performance.

The LHC gas system has been implemented following a modular design, in a way that it can be adapted to each gaseous detector requirements, but still remaining based on a common structure. The function-oriented design allows an effective construction, as well as an easier maintenance and intervention in case of any failure. Each module is also associated with a **Programmable Logic Controller (PLC)**, an industrial PC with basic functionalities for managing and monitoring the unit.

Building blocks are located over three different levels: the surface room (SG), the underground service room (US) and the experimental cavern (UX). All the units that need an immediate access are located in the SG, while the US provides the first predistribution of gas into several channels. The effective detailed distribution to each detector is instead done in the UX. The main building blocks are common to all the systems.

- **Gas supply monitoring system:** each gas is provided by two independent, supply sources, one in use and one in stand-by, that can compensate when there is a failure in the main one.
- **Mixer module:** primary gases are used to prepare the suitable gas mixture for each detector. Mixer modules have up to four input lines, equipped with **Mass Flow Controllers (MFCs)** managed via software. Gas mixtures are prepared with high precision, better than 1% on the concentration of each component.
- **Gas Distribution:** several steps are needed to distribute the gas mixture to each detector, choosing gas flow and pressure. Pre-distribution modules (located in US) are related to different detector sectors of the experiments, and they still allow some parameter tuning during LHC runs. The gas is then sent in the UX, where the final distribution modules are located. Each pre-line is split into several smaller lines, to distribute the gas with the required granularity.
- **Pump module:** Once the gas has flown inside detectors, it is sent back to the pre-distribution rack. Its outlet leads to the pump module, that compressing the gas to an higher pressure sends it to the circulation module at the surface.

In addition to these fundamental components, other blocks are generally present in the gas systems, more related to the gas management and quality monitoring.

- **Gas analysis modules** allow continuous monitoring of some critical mixture components, as well as the presence of impurities ( $O_2$  and  $H_2O$ ).  $O_2$ ,  $H_2O$  and Infra-Red analysers are normally present, but **Gas Chromatograph (GCs)** can also be used. In particular, CMS and LHCb are equipped with GC modules to allow more specific studies, i.e. monitor the presence of more complex impurities.
- **Gas recuperation module:** expensive or greenhouse gases (GHG) can be recuperated during the emptying of detector volumes, mainly to contain operational costs. The returning mixture is cooled down, until the liquefaction point of the gas, that can then be stored and reused. Typical recuperated gases are Xe,  $C_4F_{10}$ ,  $CF_4$  and  $nC_5H_{12}$ .

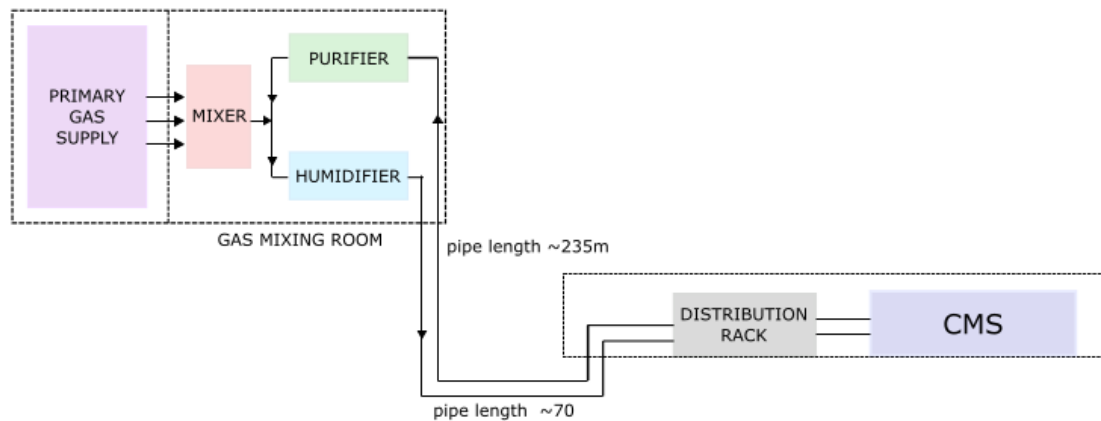


Figure 1.5: CMS gas infrastructure layout, simplified from [6].

#### 1.4 Detector upgrades for HL-LHC

With the LHC Upgrade during the LS2 and the future High-Luminosity phase, intense consolidation and upgrade for all experiments are invariably needed. It is in fact fundamental to reach the highest possible performance to

make the most out of the extremely improved running conditions of the LHC. While integration of new features and replacement of several machine components will be the basis of the future collider performance, experiments are as well in need of a complete renewal and reinforcement.

The increasing rates and pile-up effects will make more and more challenging the experiments operation. A staged upgrade program during the long shutdowns has been established. It has started during the LS1 (2013/2014) and it will continue in two other LS periods: the LS2 (2018/2019) and the future LS3 (2023/2025). The plan for ongoing and future upgrades is reported in Figure (1.6).

Major upgrades of ALICE and LHCb are taking place during the LS2, with the improvements of some sub-systems and the re-design of read-out electronics. Detector constraints set in fact limits, which need to be overcome to face the increased luminosity, already during Run 3. Moreover, the HL-LHC phase will require a significant upgrade with regard to the detector performance degradation caused by the extremely high integrated radiation dose. In this view, a substantial improvement for both CMS and ATLAS will be of primary importance. These operations are foreseen for the LS3, during which many systems will be replaced due to their radiation damage or inability to proper read-out at very high data rates. At the same time, it will be fundamental to maintain an appropriate performance for the high pile-up environment physics, which requires then innovative components to be integrated in the already existing systems.

Being this work mainly focused on gaseous detectors, main upgrades of the Muon Detector Systems will be illustrated in the following paragraphs.

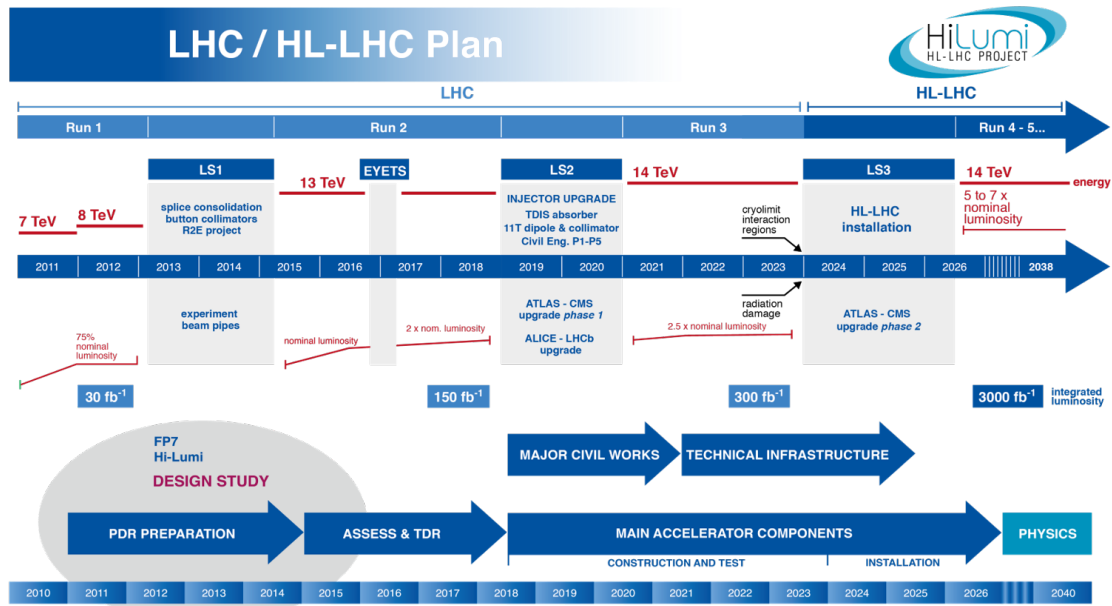


Figure 1.6: 2010-2025 plans for LHC operation and upgrades [7].

#### 1.4.1 Motivation for Muon Detector Systems upgrade

As previously illustrated, gaseous detectors are widely used in the LHC experiments for tracking, trigger and particle identification. In particular, the Muon Systems are fundamental for muon identification and momentum measurement. In the general picture of experiments upgrades, this is the system that will probably experience the least issues due to increased radiation dose. Nevertheless, a continuous performance monitoring is fundamental to keep under control their response under high particle flux. Weaknesses and failures have to be spotted in advance, in order to minimize the issues that will invariably be faced during future operations. Performance degradation due to ageing and high luminosity, read-out electronics limitations and generation of fake hits are the major aspects which need to be addressed for the future operation of gaseous detectors.

The extremely elevated luminosity that will be delivered by the LHC sets the main goals of muon systems upgrades, that include improved timing resolution, greater trigger sharpness and higher efficiency in the background rejection. These elements will mainly affect the systems in ATLAS and CMS. In particular, their forward region ( $|\eta| \geq 1.0$ ) already experiences particle rates around  $10 \text{ kHz/cm}^2$ , which causes a very high pile-up of events that can compromise the accuracy of  $p_T$  measurements. It has been demonstrated that nowadays in the ATLAS experiment about 90% of the muon triggers in the end-caps are fake or background dominated by low energy particles (mainly protons), which can be confused with high  $p_T$  muons (analysis of 2012 data, Figure (1.7)).

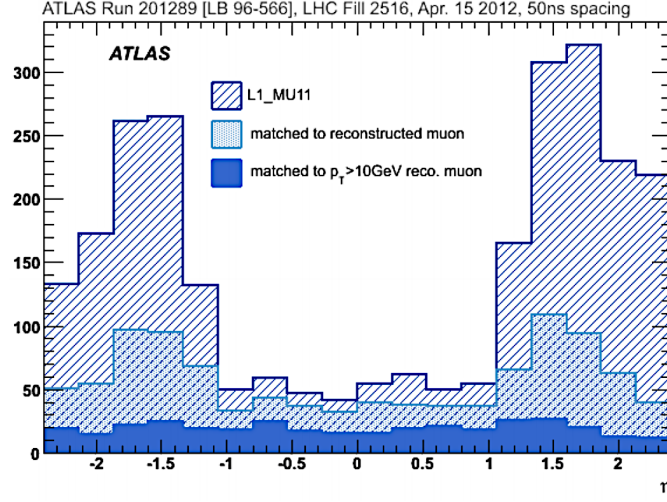


Figure 1.7:  $\eta$  distribution of the Level-1 muon signal compared to subsets with matched muon candidate and with offline reconstructed muon with  $p_T > 10 \text{ GeV}$  in the ATLAS experiment. [8].

### 1.4.2 Examples of Muon Systems Optimization

#### GEMs in LHCb Experiment

The LHCb Muon System hosts GEM detectors in the region where high particle rates are present, with a total of 20 chambers, each made of two triple-GEM detectors. The gas mixture used is Ar/CO<sub>2</sub>/CF<sub>4</sub> (45%/15%/40%), with a gas flow around 100 l/h. The presence of CF<sub>4</sub> makes the exhaust a greenhouse gas mixture. For this reason, already in 2016 the gas system was upgraded from open mode to recirculated. For the first time, GEM detectors were operated in a closed loop system after intense RD to validate the detector performance in such configuration. With this improvement, the reduction of greenhouse gases reached 90% with respect to previous operation.

#### MicroMegas in ATLAS Experiment

The forward section of ATLAS muon spectrometer (Small Wheel, SM) will exceed its design rate capabilities, since rates up to  $15 \text{ kHz/cm}^2$  are expected after the LS2. The system upgrade foresees the installation of MicroMegas, that will cover the full New Small Wheel (NSW). Intense R&D studies allowed to reach an efficient configuration for these detectors, for which the presence of sparks is generally a key issue. Resistive strips laying on the ordinary read-out strips make MicroMegas spark resistant, while maintaining their ability to measure minimum-ionizing particles with an excellent precision in high-rate environments. A total of eight planes of MicroMegas will be installed during LS2, for a total detector area of  $1200 \text{ m}^2$ . In addition, to make the NSW a fully redundant system, it will be equipped with eight planes of Thin Gap Chambers (TGC).

### GEMs and iRPCs in CMS Experiment

CMS experiment will be in need of increasing redundancy in tracking and reconstruction capabilities in the forward regions, since by now it only relies on the CSCs. Here the high background rates ( $\sim 100 \text{ kHz cm}^{-2}$ ) in the High Luminosity phase) can heavily compromise the momentum resolution, leading to a significantly higher trigger rate. Proposals to minimize this effect have found their convergence on the installation of two new stations in the end-cap region, with Gas Electron Multipliers chosen installed detectors. In particular, triple-GEM chambers are be installed in a double-layer configuration. As shown in the preliminary simulation of Figure (1.8) this will reduce the trigger rate in this region thanks to improved momentum resolution. Moreover, an extension of the Muon System acceptance is foreseen (to  $|\eta| < 3$ ), with a new GEM-based station that will be installed in the space left by the new compact endcap calorimeter. Also improved **Resistive Plate Chambers** (iRPC) are proposed for some endcap stations, in order to extend the present RPC system. The new configuration could offer excellent time resolution and at the same time it would allow a significant reduction in the neutron background and pile-up effects.

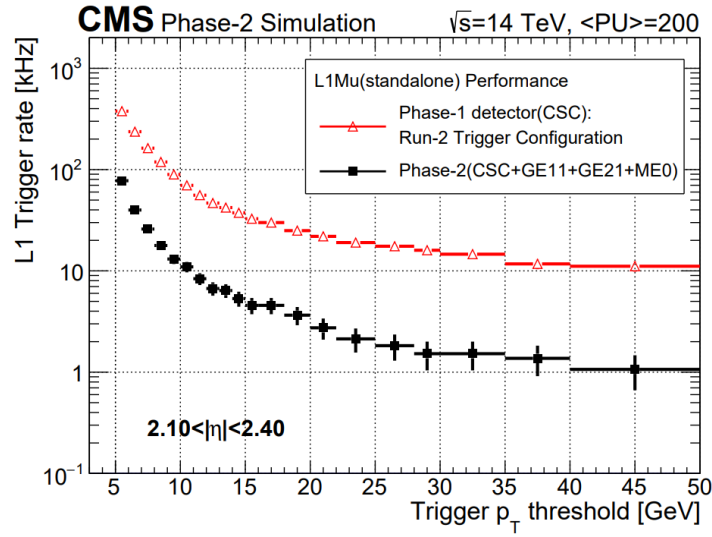


Figure 1.8: L1 prompt muon trigger rates, with and without GEM chambers, as a function of muon trigger  $p_T$  threshold in the region  $2.1 < \eta < 2.4$  [9].

## 1.5 Greenhouse gases at the LHC

### 1.5.1 Greenhouse effect

The greenhouse effect is the process of heat capture by the Earth atmosphere, with consequent surface temperature increase. Despite being commonly associated to human activities only, the greenhouse effect is a natural process critical for the support of life on the Earth's surface. The key role of the greenhouse effect can be depicted by using a simple model. An estimate of the Earth's temperature surface can be done by balancing the energy that the Earth receives from the Sun and the energy emitted by Earth itself via irradiation. In the approximation that the Earth is a black body (emissivity=1), the equilibrium equation is then

$$(1 - A)S \cdot \pi R^2 = 4\pi R^2 \cdot \sigma T^4 \quad (1)$$

being  $S$  the average power emitted by the Sun that arrives on a  $1 \text{ m}^2$  surface on Earth (*solar constant* =  $1.37 \text{ kWm}^{-2}$ ),  $R$  the Earth's radius,  $\sigma = 5.67 \cdot 10^{-8} \text{ Wm}^{-2}\text{K}^{-4}$  the Stephan-Boltzmann constant,  $T$  the Earth's surface temperature and  $A$  (*albedo*,  $\sim 0.3$ ) a constant which takes into account that part of the Solar radiation is not absorbed but rather

reflected by the Earth's surface. Equation (1) returns an Earth's temperature value of  $T = 255 \text{ K} = -18^\circ \text{C}$ . The balance equation can be corrected by including the atmosphere contribute. Despite being almost transparent to the Sun's radiation, peaked in the visible part of the electromagnetic spectrum, Earth's atmosphere can absorb part of the infrared emission of the Earth surface. The result is that the atmosphere prevents some of the energy emitted by Earth from getting lost, and that the atmosphere becomes itself an irradiating body, sending part of the energy back to the Earth's surface. The corrected power balance equation is then:

$$(1 - A)S \cdot \pi R^2 + f \cdot 4\pi R^2 \cdot \sigma T_a^4 = 4\pi R^2 \cdot \sigma T^4 \quad (2)$$

being  $\sigma_a$  the atmosphere emissivity,  $0 \leq f \leq 1$  is a constant that takes into account that the atmospheric absorption of the IR radiation is partial. By approximating  $f = 1$ , equation (2) returns  $T = 30^\circ \text{C}$ , a value  $\sim 15^\circ \text{C}$  higher than the real one, which corresponds to  $f \sim 0.68$  [10].

### 1.5.2 Greenhouse gases and Global Warming Potential

A **GreenHouse gas** (GHG) is thereby a gas which absorbs radiation in the thermal infrared range. The main GHGs in Earth's atmosphere are water vapour,  $\text{CO}_2$  and methane. Human activities, mainly the burning of fossil fuels and clearing of forests, have strengthened the greenhouse effect by increasing the GHG concentration in the atmosphere, causing a phenomenon known as global warming.

A measure of how much heat a gas traps in the atmosphere in a fixed time span is given by the **Global Warming Potential**, defined as the quantity of energy that  $1 \cdot 10^3 \text{ kg}$  of gas would absorb over a period of time, relative to the quantity of energy that would be absorbed by the same amount of  $\text{CO}_2$ . The GWP of a gas strongly depends both on his radiation absorption and in its atmospheric lifetime.

Among gases used for the gaseous detectors of the various LHC experiments, perfluorocarbons (PFCs), hydro-fluorocarbons (HFCs), hydro-chlorofluorocarbons (HCFCs) are high-GWP gases, with global warming potential in the order of thousands or tens of thousands.

### 1.6 RPCs and the GHGs

The RPC systems at LHC are operated with a  $\text{C}_2\text{H}_2\text{F}_4/\text{iC}_4\text{H}_{10}/\text{SF}_6$  gas mixture (GWP of 1430, 3.3 and 23900 respectively). The mixture composition changes slightly between different experiments but is usually close to  $\text{C}_2\text{H}_2\text{F}_4/\text{iC}_4\text{H}_{10}/\text{SF}_6$  95.2/4.5/0.3, corresponding to a total GWP of 1433. The total volume of the chambers approaches a value of  $15 \text{ m}^3$ , covering a surface of  $\sim 4000 \text{ m}^2$ . Due to the large size of the systems, the cost of the mixture and the use of greenhouse gases, the RPCs are operated in recirculating gas systems, with a recirculation fraction up to 90%. The recirculation fraction has been validated for a safe operation of the detectors and purifier cartridges are required on the return lines to clean the gas from accumulated impurities that can compromise the RPC performance. [11] It is however not possible to operate the detectors to higher recirculation fractions because of the presence of leaks at the detector level. For this reason fresh gas mixture must be continuously injected into the system, leading to GHG emissions that are found to be the highest amongst all the other gaseous particle detectors systems at LHC. The main gas contributing to GHG emissions is the  $\text{C}_2\text{H}_2\text{F}_4$ . Its production is subject to a European regulation started in 2015 [12] which aims to reduce the quantity of F-gases that can be sold to one fifth from 2014 to 2030. It is therefore advisable to search for new environmentally friendly gases with a lower GWP that can be used as an alternative to  $\text{C}_2\text{H}_2\text{F}_4$ , both to reduce high GWP gas emission and contain the operational costs. Several gases with similar properties of the  $\text{C}_2\text{H}_2\text{F}_4$  are already available on the market and used for specific industrial application as replacements for the  $\text{C}_2\text{H}_2\text{F}_4$ . Gases in the family of the HydroFluoroOlefin (HFO) have already been identified by the refrigeration industry as a low GWP ( $< 6$  over 100 years) alternatives and are used nowadays in refrigerating systems. Since the relevant properties for particle detectors operation are not available for such new gases, a simulation of the detector with the desired gas mixture can be hardly achieved. Thus, the search

for new  $C_2H_2F_4$  alternatives requires an experimental setup where RPC performance can be tested with these new eco-friendly gases.

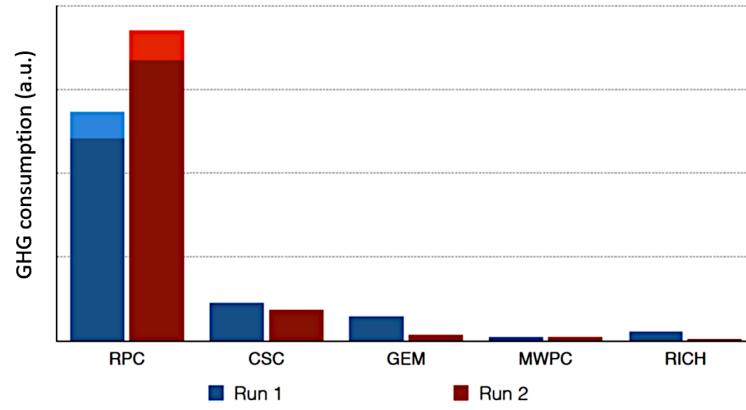


Figure 1.9: GHG emissions for LHC gaseous detectors [13].



# THE RPC DETECTOR

---

RPC detectors are planar-geometry gaseous particle detectors. As all the other particle detectors, they are based on the physical processes of gas ionization and charge multiplication. RPCs consist of two parallel plates, a positively-charged anode and a negatively-charged cathode, both made of a very high resistivity plastic material and separated by a gas volume, in which the ionization and multiplication processes take place.

## 2.1 Historical developments

The first gaseous detector with a planar geometry was designed in the late '40s by J. W. Keuffel. The prototype detector, called **Parallel Plate Chamber (PPC)**, had copper electrodes with a 25 m<sup>2</sup> surface at high voltage (1 - 3kV), a 2.5 mm wide gas gap filled with an Argon-Xylene (C<sub>6</sub>H<sub>12</sub>(CH<sub>3</sub>)<sub>2</sub>) based gas mixture at about 500 mbar. Signal in PPCs is produced by a spark generated by the charge multiplication process. Being the electrodes conductive, an external switch-off circuit is needed in order to stop the spark. The need of this switch-off system represents a problem, as it introduces a dead time up to 1s after the particle is detected, thus limiting the maximum detection rate.

In the '70s a very important change was introduced in the development of parallel plate detectors: the metal electrodes were substituted by resistive ones. Resistive electrodes bring to self-extinguishing multiplication processes and to a spatially confined modification of the electrode voltage, leaving the rest of the surface ready to detect other impinging particles. The first detector with resistive electrodes, known as **Planar Spark Chamber (PSC)** was built in 1978 by N. Pestov: the electrodes were made of glass, the gas gap width was between 0.1 and 1mm and was filled with a gas mixture based on Argon, Neon and an organic(?) gas for the UV photon absorption. The PSC achieved a time resolution of about 25 ps in detectors with a gap 0.1 mm wide.

At the beginning of '80s the development of new technologies made available for the first time phenolic resin materials, good candidates for replacing the breakable glass of the PSCs, allowing the detector to cover a larger area. The new gas detector made with this material was developed by R. Santonico and it was named **Resistive Plate Chamber (RPC)**. As will be explained in the following sections, the RPC has many advantages with respect to the other planar gas detectors and for this reason it is widely used in three of the four experiments at the CERN Large Hadron Collider.

### 2.1.1 General description of an RPC

A scheme of a RPC detector is shown in Figure (2.1). The resistive plates are separated by a grid of non conductive material made cylinders, which are referred to as *spacers*. Spacers are 2 mm high, have a diameter of 10 mm and a density of 100 /m<sup>2</sup>, and they improve the rigidity of the detector and ensure a uniform thickness of the gap. The gap can be filled using different gas mixtures at atmospheric pressure. The importance of the gas mixture, which plays a key role in the detector performance, will be discussed in the next section.

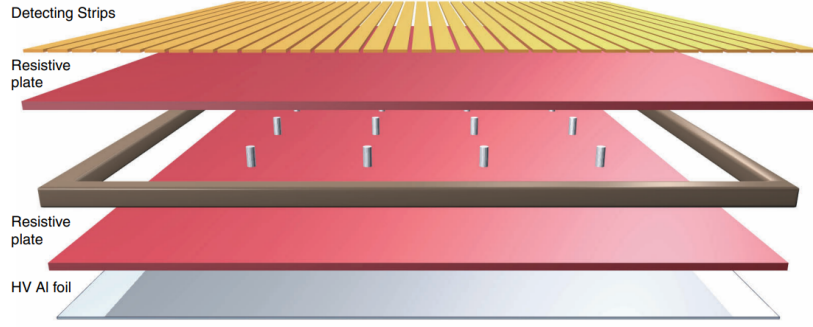


Figure 2.1: Scheme of a RPC detector.

## 2.2 Detection principles

### 2.2.1 Charge multiplication

The basic phenomena behind the a particle detection is an ionization event inside the gap, with an electron-ion pair production. If a voltage difference between the electrodes exists, an electric field is created inside the gap

$$E = \frac{\Delta V}{d} \quad (3)$$

being  $d$  the gap width. If the electric field inside the gap is sufficiently strong, the *primary electron* can gain enough energy to further ionize other gas molecules; *secondary* electrons, accelerated by the electric field, produce a third generation of ion-electron pairs, and so on. The result is a multiplication process, in which an electron *avalanche* is created.

The avalanche formation can be described by assuming the probability of an electron producing an electron-ion pair to be independent from the previous multiplication stage. Let  $\lambda$  be the electron's mean free path, i.e. the average distance an electron travels between two different pair productions. After travelling a distance equal to  $x = n\lambda$  inside the gap, a single electron has produced  $2^n$  secondary electrons. For a generic travelled distance, the number of produced electrons is

$$N(x) = 2^{\frac{x}{\lambda}} = (e^{\log 2})^{x/\lambda} = e^{\frac{\log 2}{\lambda}x} = e^{\alpha x} \quad (4)$$

where

$$\alpha = \frac{\log 2}{\lambda} \quad (5)$$

is known as the Townsend coefficient. The multiplication, and so the Townsend coefficient, are strictly dependent on the gas conditions and on the strength of the electric field. The relation is expressed by Korff's Formula [14]:

$$\frac{\alpha}{p} = A \cdot e^{-\frac{Bp}{E}} \quad (6)$$

being A and B constants dependent on the gas mixture. If the electric field is too weak, electrons don't gain enough energy to ionize neutral gas molecules. The gas pressure gives information on the gas density, and different gas density: the higher the gas density, the shorter the electron the mean free path, the less the average energy be gained by an electron between two different impacts with neutrals.

During the drift process, electrons can however be captured by electronegative atoms. Together with the multiplication coefficient, the attachment probability  $\beta$  is defined. If  $N(x)$  is the number of electrons at distance  $x$  from the anode, the variation on the number of electrons after a travel distance  $dx$  due to the capture process is given by

$$\frac{dN(x)}{dx} = -\beta n(x) \quad (7)$$

The total variation, considering both multiplication and capture processes, is then given by

$$\frac{dN(x)}{dx} = (\alpha - \beta) \cdot N(x) = \alpha^* \cdot N(x) \quad (8)$$

so that

$$N(x) = e^{\alpha^* \cdot x} \quad (9)$$

being  $\alpha^*$  the effective Townsend coefficient.

### 2.2.2 Raether limit

As the charge multiplication process goes on, the number of the electrons inside the avalanche (which is usually called *Multiplication* and referred to as  $M$ ) increases. Theoretically,  $M$  should have no limit, and could be increased at will by increasing the effective Townsend coefficient or the travelling length  $x$ . As soon as the avalanche grows, though, space charge effects appear, with a local variation on the electric field. When the space charge reaches a certain limit, the avalanche process develops into a spark breakdown. The physical limit at which the breakdown takes place is given by Raether condition [15]:

$$\alpha^* \cdot x \sim 20 \quad (10)$$

or equivalently  $M \sim 10^8$ , which corresponds to a total avalanche charge of  $\sim 16$  pC. In order to avoid spark formation inside the gap, high electronegativity gases can be added to the mixture in order to lower the value of the effective Townsend constant.

### 2.2.3 Statistical fluctuation of the avalanche charge

Charge multiplication is a stochastic process. Thus, the total number of electrons inside an avalanche which developed over a fixed travelling path  $\bar{x}$  will not be constant, but rather have a certain probability distribution. To derive the statistical fluctuation of the avalanche, we proceed as shown in [16]. Let  $dx$  be a distance so small that a single duplication or capture process happens while the whole front distribution moves from  $x$  to  $x + dx$ . The probability of having exactly  $N$  electrons at position  $x + dx$  is:

$$\begin{aligned} P(N, x + dx) = & P(N - 1, x) \cdot [\alpha(N - 1)dx] \cdot [1 - \beta(N - 1)dx] + \\ & P(N, x) \cdot [1 - N\alpha dx] \cdot [1 - \beta N dx] + \\ & P(N, x) \cdot [\alpha N dx] \cdot [\beta N dx] + \\ & P(N + 1, x) \cdot [1 - \alpha(N + 1)dx] \cdot [\beta(N + 1)dx] \end{aligned} \quad (11)$$

The first line gives the probability that there are  $N - 1$  electrons at position  $x$ , exactly one of them duplicates and no electron is captured. The second line gives the probability that there are  $N$  electrons at  $x$ , no electron duplicates and no electron is captured. The third line gives the probability that from  $N$  electrons, one multiplies and one gets captured and finally the fourth line gives the probability that from  $N + 1$  electrons one gets captured and no electron is multiplied. The expressions for the four described possibilities are not trivial, so the derivation of the first line will be reported as a guideline to derive all four. Having exactly  $N-1$  electrons, one multiplication and zero capture processes means that

$$\begin{aligned} 1 &= \left. \frac{d(N - 1)}{dx} \right|_{\text{multiplication}} = \alpha(N - 1)dx \\ 0 &= \left. \frac{d(N - 1)}{dx} \right|_{\text{capture}} = -\beta(N - 1)dx \quad 0 = -\beta(N - 1)dx \quad 1 = 1 - \beta(N - 1)dx \end{aligned}$$

Coefficients multiplying probabilities on the right hand side of equation 11 are all equal to 1. If we neglect second-order term in  $dx$ , writing the coefficient in such a way allows us to divide all the members of the equation by  $dx$ , obtaining the differential equation

$$\frac{dP(N, x)}{dx} = -P(N, x) \cdot [(\alpha + \beta)N] + P(N - 1, x) \cdot [\alpha(N - 1)] + P(N + 1, x) \cdot [\beta(N + 1)] \quad (12)$$

which has general solution

$$P(N, x) = \begin{cases} k^{\frac{\bar{N}(x)-1}{\bar{N}(x)-k}}, & N = 0 \\ \bar{N}(x) \left( \frac{1-k}{\bar{N}(x)-k} \right)^2 \left( \frac{\bar{N}(x)-1}{\bar{N}(x)-k} \right)^{N-1}, & N > 0 \end{cases} \quad (13)$$

where

$$k = \frac{\beta}{\alpha} \quad (14)$$

The avalanche charge distribution mean value and variance are, respectively:

$$\bar{N}(x) = e^{(\alpha-\beta)x} \quad (15)$$

$$\sigma^2(x) = \left( \frac{1+k}{1-k} \right) \cdot \bar{N}(x) \cdot [\bar{N}(x) - 1] \quad (16)$$

### 2.2.4 Multiple clusters formation

A single ionizing particle can in principle produce more than one primary electron-ion pair. It is then useful to define the number of clusters  $n_{cl}$  as the number of primary pairs generated directly by the impinging particle, plus the additional pairs that are generated by the primary electron in case it has a kinetic energy high enough to further ionize atoms or molecules of the mixture. The number of clusters  $n_{cl}$  following the passage of an ionizing particle, of course, is not fixed, but its actual value changes from event to event according to a certain probability distribution:  $n_{cl}$  is a stochastic variable, which depends linearly on the gas thickness  $g$  crossed by the particle.

Values for the average value of the number of clusters per unit length, which here will be indicated with  $\lambda_{cl}$  have been measured experimentally for many gases and can be found in the literature; in case of gas mixtures, the value for  $\lambda_{cl}$  is the weighted average of the ones corresponding to the gas mixture components, with weights equal to the gas fractions.  $\lambda_{cl}$  depends, in general, on the energy of the impinging particle. Here, for the sake of simplicity, we will suppose that the energy lost by the particle crossing the gas gap is negligible with respect to its kinetic energy; this assumption is generally true in most cosmic ray experiments, or the muon systems of the LHC experiments. In this case, we can safely assume that the kinetic and total energy of the impinging particle, and consequently the primary ion/electron pair density  $\lambda_{cl}$  is constant throughout the particle path in the gas gap. In case the particle is crossing the RPC gas gap not perpendicularly, we will also define

$$\lambda_{\text{eff}} = \frac{\lambda_{cl}}{\cos \phi} \quad (17)$$

where  $\phi$  is the azimuthal angle of the track of the incident particle.

Given these assumptions, the probability  $P_{cl}$  that  $k$  clusters are generated in the gas gap (whose width is indicated with  $g$ ) by an ionizing particle can be computed by simple binomial statistics; the following result is obtained from a Poisson distribution:

$$P_{cl}(n_{cl} = k) = \frac{(g\lambda_{\text{eff}})^k}{k!} e^{-g\lambda_{\text{eff}}} \quad (18)$$

Moreover, the probability  $P(n_{cl} = 0)$  that not one single cluster is generated in the gas gap by the passage of an ionizing particle is easily computed from the above mentioned formula by putting  $n_{cl} = 0$ , and is given by

$$P_{cl}(n_{cl} = 0) = e^{-g\lambda_{\text{eff}}} \quad (19)$$

Equation 19 is important since it expresses the intrinsic inefficiency of a gaseous detector; its value imposes limits on the thickness of the gap width which needs to be used in order to have a reasonable efficiency. Just as an example, by using  $\lambda_{cl} = 5.5$  cluster/mm (corresponding to gas mixture  $C_2H_2H_4/iC_4H_{10}/SF_6$  95.0/4.7/0.3, a mixture very similar to the one now in use), a gas gap with 0.2mm width would result in an intrinsic inefficiency around 11%.

### 2.2.5 Total developed charge

The total charge developed after an ionizing particle passed through the RPC gas can be modeled from an exponential growth related to the effective Townsend coefficient of the gas and it is expressed by the formula:

$$q(t) = \sum_{j=1}^{n_{cl}} q_e n_0^j M_j e^{\alpha^* v_d t} = q_e e^{\alpha^* v_d t} \sum_{j=1}^{n_{cl}} n_0^j M_j \quad 0 < t \leq \frac{g - x_0^{n_{cl}}}{v_d} \quad (20)$$

where  $q_e$  is the charge of the electron,  $n_0^j$  is the number of electrons in the  $j$ -th cluster,  $\alpha^*$  is the effective Townsend coefficient,  $v_d$  is the drift velocity of the electrons and  $M_j$  are some random numbers extracted from a Polya distribution, describing the stochastic effects that takes place in the avalanche development [17].

### 2.2.6 Signal formation on the readout strips

The signal of the RPC is usually read on Copper or Aluminum strips placed close to the electrodes. Using the Shockley-Ramo theorem which states that the induced charge on the strip depends on the instantaneous change in the line flux of the electromagnetic field it is possible to describe the induced current with the expression:

$$I_{ind} = q \mathbf{v}_d \cdot \mathbf{E}_w \quad (21)$$

where  $\mathbf{v}_d$  is the electrons' drift velocity and  $\mathbf{E}_w$  is the weighting field, which in the case of the RPC can be assumed uniform across the gap and can be expressed in terms of the gas gap and the thickness of the electrodes by the formula:

$$E_w = \frac{\varepsilon_r}{\varepsilon_r g + 2d} \quad (22)$$

where  $\varepsilon_r$  is the dielectric permittivity of the electrodes and  $d$  is the electrode thickness. The induced current over time caused by the avalanche process takes then the following expression:

$$I_{ind}(t) = \mathbf{v}_d \cdot \mathbf{E}_w q_e e^{\alpha^* v_d t} \sum_{j=1}^{n_{cl}} n_0^j M_j \quad (23)$$

and integrating the expression over time one get the total induced charge:

$$q_{ind}(t) = \frac{\varepsilon_r}{\varepsilon_r g + 2d} \frac{q_e}{\alpha^* g} \sum_{j=1}^{n_{cl}} n_0^j M_j \left[ e^{\alpha^* (g - x_0^j)} - 1 \right] \quad (24)$$

### 2.2.7 Avalanche and streamer modes

RPC detectors can be operated in two different modes defined by the number of electrons created during the ionization processes.

In the **avalanche mode**, the amplification of the signal inside the gap is small and proportional under the Townsend mechanism.

In the **streamer mode**, a number of nonlinear effects are added to the linear mechanism. The electric field generated by the space charge ( $E_S$ ) is comparable with the external electric field ( $E_E$ ). When  $E_S = E_E$  the avalanche formation should theoretically arrest, but not in this case: new photoionization processes, due to recombination and excitation phenomena, ionize the gas molecules around the avalanche region developing secondary avalanches

along the avalanche axis. These avalanches are all close and they move forward the electrode until the formation of one charge filament, the streamer. Thus the streamer is not a direct evolution of the first avalanche but rather a late discharge stage that develops via gas photoionization processes after the first avalanche is extinguished. In a RPC at low voltage range the grow of the charge is exponential, that is typical of the proportional mode. At higher voltage multiple pulsed signals start to appear: the avalanche to streamer transition occurs. The new pulses are late and the signals are much larger than before. As an example, in the wave form shown in Figure (2.2) an avalanche signal is followed by a streamer afterpulse.

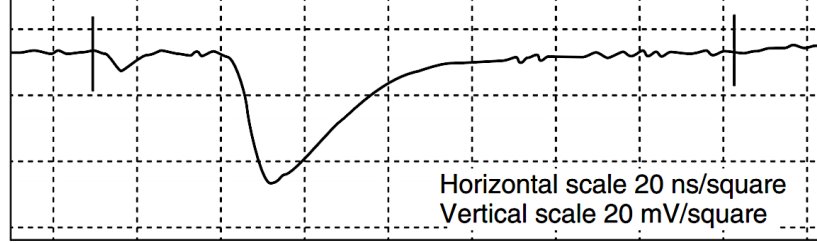


Figure 2.2: Avalanche precursor followed by a streamer pulse [21].

## 2.3 Foremost parameters

### 2.3.1 Charge distribution

The charge distribution that an ionizing particle crossing the gas gap on an RPC is expected to produce on an external readout electrode can be computed and simulated using Monte Carlo techniques due to the presence of many stochastic variables in equation (24). The simulation for two RPC gaps with 2 mm and 9 mm, with fixed cluster density  $\lambda_{cl} = 5.5$  clusters/mm, shows that the charge distributions strongly differ from each other. In the former case the distribution tends to diverge when  $q_{ind} \rightarrow 0$  while in the latter the induced charge tends to vanish for  $q_{ind} \rightarrow 0$ .

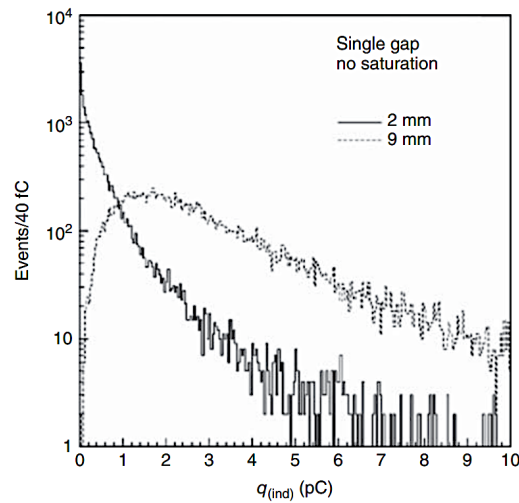


Figure 2.3: Simulated spectra of the induced charge, for a 2-mm single-gap RPC, compared to the same spectra but for a 9-mm single-gap RPC [17].

### 2.3.2 Efficiency

The efficiency of the detector depends on the electronic noise of the readout and in general on the noise of the system. From the equation (24) it is possible to compute the distance from the cathode required for a cluster to be originated in such a way that a charge is above a certain electronic threshold  $q_{thr}$ :

$$x_0^1 = g - \frac{1}{\alpha^*} \log \left( \frac{q_{thr}}{A_1} + 1 \right) \quad (25)$$

where  $A_1$  is defined as

$$A_1 = \frac{q_{ew} M_1 n_0^1}{\alpha^* g} \quad (26)$$

The probability  $P$  of observing one cluster in the position  $x_0^j$  is following a Poisson distribution. Thus, the efficiency is just  $1 - P(0)$  and for a set of clusters can be described as:

$$\varepsilon_c = 1 - e^{-(1-\beta/\alpha)g\lambda_{cl}} \left[ 1 + \Delta V_w \frac{\alpha - \beta}{q_e} q_{thr} \right]^{\lambda_{cl}/\alpha} \quad (27)$$

where  $\alpha$  is the first Townsend coefficient and  $\beta$  is the electronegativity attachment. The efficiency of the detector depends on the gas gap and on the choice of the gas mixture (through  $\alpha$  and  $\beta$ ).

### 2.3.3 Time resolution

The time resolution can be computed using the previous equations as well. It is possible to compute the time  $t$  at which the induced current  $q_{ind}(t)$  crosses a threshold  $I_{thr}$ . Let us consider the signal of a primary electron somewhere in the RPC gap. The induced current can be described as:

$$I_{ind}(t) = I_s e^{\alpha^* v_d t} \quad (28)$$

where  $I_s$  is the signal current amplitude, different from event to event, exponentially distributed around some average amplitude. The time  $t$  at which the signal crosses  $I_{thr}$  is then

$$t = \frac{1}{\alpha^* v_d} \log \frac{I_{thr}}{I_s} \quad (29)$$

whose fluctuation can be obtained by making the proper calculations on  $I_s$ .

### 2.3.4 Gas mixture

The choice of the gas mixture is of fundamental importance for the RPC and at the same time a difficult task. There are several requirements for a gas mixture to be considered as optimal. In general, a gas mixture should be good combination of the following characteristics:

- high density of primary ion-electron clusters so that a high detection efficiency is ensured;
- high electronegativity to reduce the spatial distribution of the charge;
- possibly not toxic or dangerous for human health
- relevant quenching properties to reduce the photon feedback phenomena
- the chemical processes taking place inside the gap should not produced elements than can damage the electrode surface
- the gas mixture should be eco-friendly with the lowest GWP possible, , in order to reduce the greenhouse effect as it has been prescribed by the European Community and the regulations of the countries following the Kyoto protocol.

A crucial parameter to understand the performance of a RPC detector is the cluster density. As stated in equation (27), the inefficiency is related to  $e^{-\lambda_{cl}d}$ , so that in principle  $\lambda_{cl}$  should be as large as possible to maximize the signal and to achieve high detection efficiency. A higher value of  $\lambda_{cl}$  implies a lower streamer probability (Figure (??)), making the mixture suitable for RPC operation in avalanche mode.

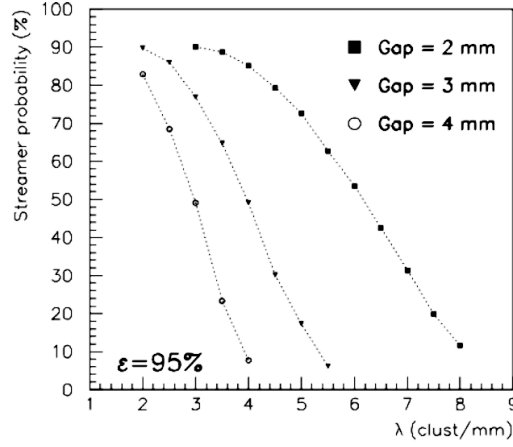


Figure 2.4: Streamer probability as a function of  $\lambda_{cl}$  [18].

With a high concentration of  $C_2H_2F_4$ , in addition to a high value of  $\lambda_{cl}$ , the RPCs have excellent timing properties due to higher electron drift velocity compared to that of other gases. Even in small percentage with respect to  $C_2H_2F_4$ , polyatomic molecules acting as a quencher, like  $iC_4H_{10}$ , are necessary in order to absorb photons in a wide energy range. In fact such molecules have a large number of non-radiative rotational and vibrational excited states and therefore they avoid the production of secondary avalanche by the UV photons emitted in the avalanche multiplication process. In order to decrease the streamer formation, a small percentage of a gas with a high electronegativity attachment is added to the mixture. This modifies the drift properties of the electrons, being captured by the electronegative gas. In particular, it has been demonstrated that adding a small quantity of  $SF_6$  to the mixture with  $C_2H_2F_4/iC_4H_{10}$  helps to suppress the streamer, as it can be seen in figure.. There is a clear peak of streamers when no  $SF_6$  is present with a mean value of 80 pC. The progressive addition of the  $SF_6$  to the baseline mixture suppress the formation of the streamers. The effectiveness of the  $SF_6$  as a streamer suppressor is related to its low electron affinity properties ( $1.05 \pm 0.1$  eV)

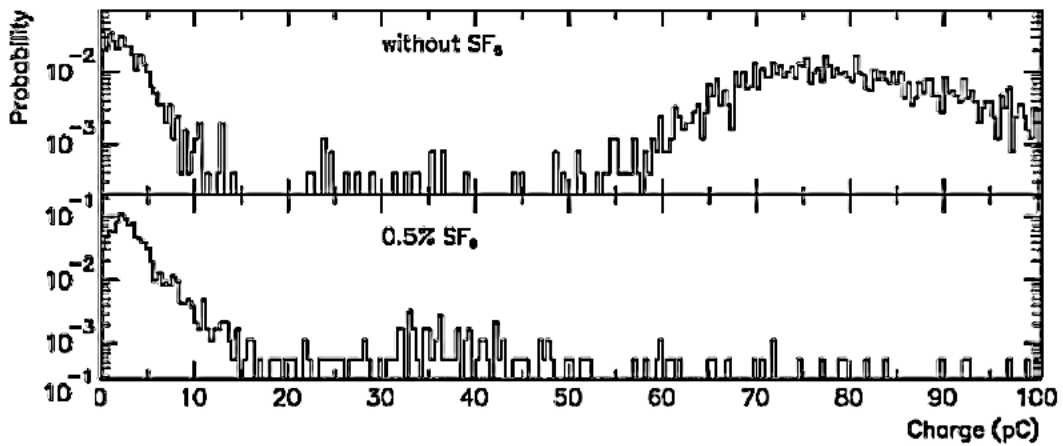


Figure 2.5: Experimental charge distribution for two different percentages of  $SF_6$  added to the mixture [19].



### 2.3.5 Bulk resistivity

The RPC resistive electrodes are usually made of bakelite (phenolic resin) plates covered with a thin layer of melamine. The bakelite plates are made of several compressed layers of ordinary paper imbued with resin, then heated and finally cut to the proper size. The percentage change of phenolic and melamine resin carries a different bulk resistivity, so it's the final user that decides the bulk resistivity of the RPC, a very important parameter because the rate capability is strongly dependent on it. As it will better explained in the next section, at very high particle rate a drop of voltage  $V_d$  occurs across the plates because of the high current flow between them. Such voltage drop is proportional to the electrodes resistance  $R$ , and therefore to the resistivity. A lower resistivity implies a lower voltage drop for a fixed particle rate.

The quality of the bakelite is very important and it is crucial to monitor the environmental condition in which the RPC is located. As a matter of fact the resistivity is strongly dependent on temperature and humidity conditions. For example, work done by many groups has shown that the resistivity is correlated with the environmental temperature by the following empirical relation

$$\rho_{20} = \rho_T \cdot 0.99e^{0.128(T-20)} \quad (30)$$

where  $\rho_T$  is the measured resistivity at temperature  $T$  expressed in Celsius.

### 2.4 Pressure and temperature effects

The temperature and pressure affect the RPC operation in a relevant way. In first instance the temperature affects the resistivity of the bakelite. Bakelite resistivity usually decreases to an order of magnitude with a temperature increase of 20°C. Moreover, the temperature and the pressure have a direct relationship with the gas density. Generally speaking, drift velocity and multiplication parameters depend on the ratio  $E/\rho_{\text{gas}}$  and therefore any change in the temperature  $T$  or in the pressure  $p$  is affecting these parameters as well. It is then useful to introduce the concept of effective applied voltage when comparing data from the same RPC

$$HV_{\text{eff}} = HV_0 \cdot \frac{p_0}{p} \cdot \frac{T}{T_0} \quad (31)$$

where  $p$  and  $T$  are the measured values for pressure and temperature,  $p_0$  and  $T_0$  reference values. In the measurements described in chapter 4, the reference values used for CMS experiment will be used ( $p_0 = 960$  mbar,  $T_0 = 20^\circ\text{C}$ ).

### 2.5 Electrical scheme

The equivalent circuit of an RPC detector is shown in Figure (2.6). The gas is represented as a parallel between the spacers resistance and a diode representing the gas: the diode symbol is due to the fact that, in the ideal limit, the gas is totally non conductive for low applied voltage and has zero-resistance if voltages sufficiently high are applied.

When a current  $I$  flows through the RPC, the voltage drop inside the gap is given by

$$V_{\text{gap}} = V_A - V_B = V - \frac{R}{2} \cdot I - \frac{R}{2} \cdot I = V - R \cdot I \quad (32)$$

with  $R$  total electrodes' resistance.

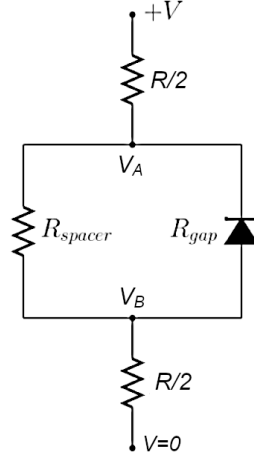


Figure 2.6: Equivalent circuit of an RPC detector.

### 2.6 Model for RPC detectors operating at high rate

The  $I V_{\text{gap}}$  curve can be modeled by a linear function with a sharp threshold  $V_T$

$$I(V_{\text{gap}}) = a \cdot \theta(V_{\text{gap}} - V_T) \cdot (V_{\text{gap}} - V_T) \quad (33)$$

where  $\theta$  is the unit step function. The experimental curve is well described by the sharp threshold model, with the exception of (V-I) points close to the voltage threshold value. The curve is therefore modelled with the sharp threshold function folded with a gaussian distribution of  $V_T$ :

$$I(V_{\text{gap}}) = a \cdot \left[ \frac{\sigma_T}{\sqrt{2\pi}} \exp\left(-0.5 \cdot \left(\frac{V_{\text{gap}} - V_T}{\sigma_T}\right)^2\right) + 0.5 \cdot (V_{\text{gap}} - V_T) \cdot \left(1 + \text{erf}\left(\frac{V_{\text{gap}} - V_T}{\sqrt{2}\sigma_T}\right)\right) \right] \quad (34)$$

where  $\bar{V}_T$  is the average  $V_T$  value,  $\sigma_T$  it RMS spread and  $a$  is a normalization factor which depends on both the electrodes resistance and on the impinging particle flux. For high particle flux,  $a$  can be expressed in form [20]:

$$a = \frac{1}{R} \cdot \frac{X}{1 + X} \quad (35)$$

where  $R$  is the total electrodes' resistance and  $X$  depends on the particle flux in a way such that

$$X \rightarrow +\infty, \quad \text{high flux condition} \qquad X \rightarrow 0, \quad \text{low flux condition}$$

This implies

$$a \rightarrow \frac{1}{R} \quad (36)$$

if the particle flux is high enough. In such a case, charge is continuously created inside the gap: the current flows freely in the gas gap, which acts as a short circuit between the electrode.

# GAS RELATED STUDIES ON RPC DETECTORS

---

This chapter describes the studies realized with RPC detectors operated in a laboratory setup. Data acquired with the standard gas mixtures used in LHC experiments ( $C_2H_2F_4/iC_4H_{10}/SF_6$  95.2/4.5/0.3) will be taken as an example caseto introduce the parameters which define the detectors performance and to provide some examples of the data analysis procedure.

## 3.1 Experiment goals and experimental setup

The main goal of laboratory tests is to evaluate the RPC performance as a muon-detecting system. For laboratory tests, cosmic muons are used as the to-be-detected particle. The experimental setup consists of a gas supplying system connected to one or more detectors and of an electronic readout system to acquire data from the RPCs. All the used RPCs readout consists of seven 2.1cm large copper strips, and a set of two scintillators is used as a triggering system to select only the muons which cross the readout area. A schematic view of the setup is reported in Figure (3.1).

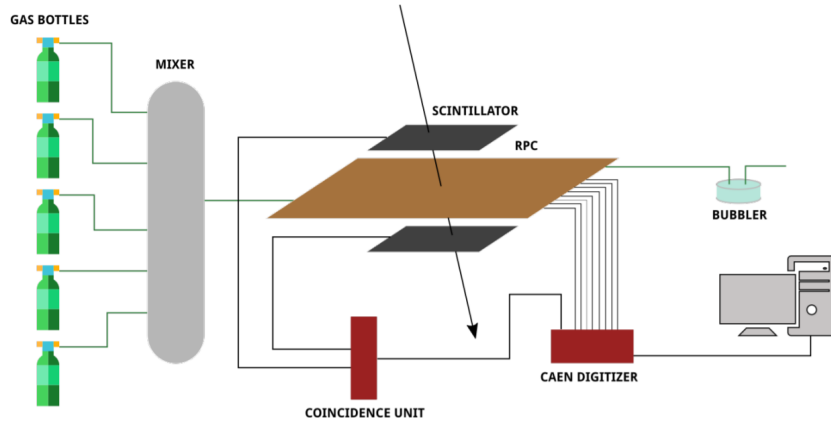


Figure 3.1: Experimental setup.

### 3.1.1 Gas supplying system

The gas supplying system consists of a series of gas bottles connected to different gas lines. The gas flow in each line is controlled by a Mass Flow Controller (MFC), a device capable of regulating the output flow, thereby allowing to create the desired gas mixture. MFCs are remotely connected to a PC and controlled via dedicated software. Each MFC output is then connected to a 2L volume (*mixing volume*), where the different gases mix up before going to the input of the detector. A return line, terminating into a bubbler, allows to visually check that the gas is flushing thorough the detector and to make sure that the detector is operating at the correct pressure (few mbars).

### 3.1.2 RPC gap, trigger and readout systems

Two standard 2mm gap wide, 70.5cm  $\times$  100.5cm RPCs were used. The signal readout is made of seven 2.1cm wide and 0.2cm distant copper strips for each RPC. Each strip is terminated using a  $56\Omega$  resistance on one side, and a lemo cable is soldered on the opposite side. Lemo cables are then connected to a CAEN VME digitizer which allows the signal readout. During the experiments, both v1720 and v1730 models were used.

The digitizer allows to record a voltage signal in ADC units, sampled over time. Every recorded event is defined by a fixed-sample-length window, in which samples are acquired at a defined sampling frequency. Every digitizer has a maximum voltage range that can be measured and a specific resolution. Technical parameters of used digitizer are reported in Table (3.1).

model	window size	sampling frequency [Hz]	voltage range [V]	resolution [bit]	resolution [mV]
v1730	520	5.0e8	2	14	0.122

Table 3.1: CAEN digitizers specifics.

A set of two 20cm  $\times$  60cm scintillators (SC01, SC02) was used as a trigger system. Scintillator SC01 was placed over the RPCs, while SC02 was placed below. Scintillators were aligned and positioned so that the readout area is totally contained between them. Each scintillator has an output lemo cable connected to a discriminator and afterwards to a coincidence module: when a particle passes through both SC01 and SC02, a NIM signal is sent to channel CH0 of the used digitizer. The digitizer records data in continuous mode; when a trigger signal arrives on channel CH0, data corresponding to the previous time window and collected via other channels, connected to the RPC strips, are saved.

### 3.2 Single strip Analysis procedure

As discussed in chapter two, an ionizing particle passing through the RPC gap may start an avalanche ionization process and produce a local charge. Such local charge induces a second charge on a readout strip; the induced charge can be seen as a voltage drop on the signal measured on the strip. The height and duration of the voltage drop, together with the number of strips which experience such voltage drop, give us information about the local charge inside the gap. Reflections or overshoots due to non perfect impedance matching and strip crosstalk can be seen during the recording of a signal. For this reason it is important to analyse the shape of the signal in order to discriminate particle signals from eventual electronic noise. The discrimination procedure will be discussed in detail in the following sections. An example of an avalanche signal given by a passing particle is shown in figure (3.2).

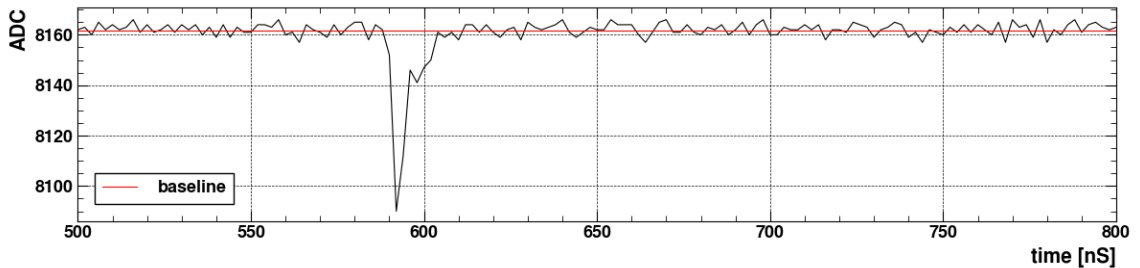


Figure 3.2: ADC drop on strip signal.

### 3.3 Signal processing

For each recorded signal, a series of analysis steps take place. The analysis steps list is:

1. **baseline calculation and subtraction;** CAEN digitizer settings are set so that data recording starts at least 200ns before the trigger signal given by the scintillators. Given this and the 2ns time step of the v1730 digitizer used for this example data collection, a 100 samples long window is used to compute the signal baseline;
2. **noise filtering:** all signal ADC values falling in  $(-\text{noise\_threshold}, \text{noise\_threshold})$  interval are set to 0.  $\text{noise\_threshold}$  value can be defined in several ways (manual definition, baseline data RMS value,...); for this example analysis,  $\text{noise\_threshold}$  was manually set to 9ADC;
3. **pulse-noise discrimination:** a pulse is considered so in it satisfies two different conditions:

$$\min(\text{signal}) < \text{height\_threshold}$$

$$\left| \frac{\min(\text{signal})}{\max(\text{signal})} \right| > \text{reflection\_threshold}$$

Both  $\text{height\_threshold}$  and  $\text{reflection\_threshold}$  are user defined parameters. The first one ensures that a peak in the signal is actually present, the second one is used as a discriminant to discard signals for which positive peaks with comparable height are present in the signals, i.e. some kind of signal reflection took place;

4. **cumulative charge calculation;**
5. **cumulative charge smoothing and pulse duration evaluation.**

#### 3.3.1 Charge development

For every sample point, the total charge accumulated *up to that point* is computed. Please note that "accumulated" doesn't mean that this charge actually accumulates somewhere, as the strips are grounded and charge flows to the ground as soon as it forms on the strip. Given the resistance  $R$  and the voltage  $V$  of a strip, the flowing current can be calculated using the first Ohm law:  $I = V/R$ . The total charge can then be computed by integrating the current over time. Stopping the integration at a sample point  $\bar{N}$  returns the total charge formed *up until sample point  $\bar{N}$*  itself. In formulas

$$Q_{tot} = \sum_{n=1}^{\text{window\_size}} \frac{\text{signal\_amplitude}(n) [\text{V}]}{R} \cdot \frac{1}{\text{sampling\_frequency}} \quad (37)$$

$$Q(\bar{N}) = \sum_{n=1}^{\bar{N}} \frac{\text{signal\_amplitude}(n) [\text{V}]}{R} \cdot \frac{1}{\text{sampling\_frequency}} \quad (38)$$

After cumulative charge has been computed, a smoothing operation takes place. For the shown example, a seven-points-window moving average smoothing process has been used. The number of pulses in the signal has been defined as the number of separated intervals for which the derivative of the smoothed charge is non-zero. For each interval, the pulse width in sample points is defined as the amplitude of the interval itself, minus a correction given by the size of the window used for the smoothing process. The total time over threshold, defined as the sum of the width of all pulses in the signal, is then computed. An example plot of single-pulse signal and of its cumulative charge is shown in Figure (3.3). It is worth noting that with this approach, a pulse is considered *finished* only if there are at least a few consecutive points under  $\text{noise\_threshold}$  level after the signal minimum; the number of consecutive points is set by the smoothing window size. The purpose of charge smoothing is to compute the pulse duration avoiding problems related to multiple crossings of the set  $\text{noise\_threshold}$ . It is worth noting that, while performing the smoothing operation on the signal itself would have modified the area under the signal, i.e. the collected charge, the same operation performed on the charge itself doesn't alter the final result.

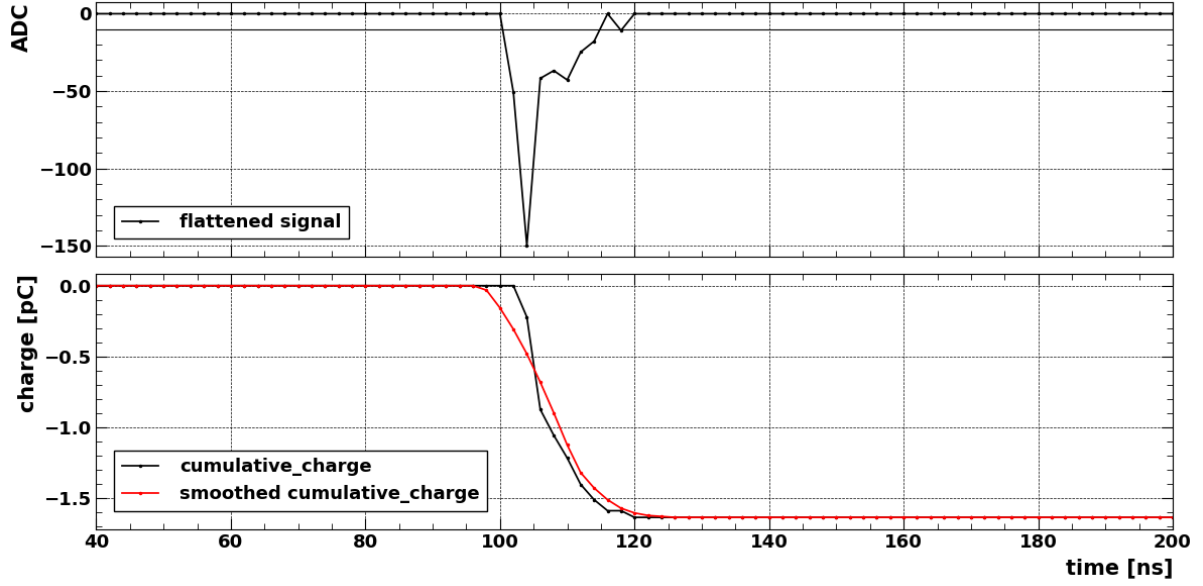


Figure 3.3: Flattened signal (above); computed cumulative charge (below).

### 3.4 Analyzed data structure

Analyzed data information is stored in tabular form using a pandas DataFrame [22]. Each row is associated to a unique tuple corresponding to a single strip signal; rows with the same event number correspond to the same scintillator trigger. The tabular form allows easy access to particular events or group of events which meet certain conditions. The analysis results for the event corresponding to the signal shown in Figure (3.3) are shown in Figure (3.4). Other event features, computed via the multi-strip analysis described below, are added to analysis results in a later step.

	HV	event	strip	minimum	fired	reflection	cumulative_charge	n_pulses	widths	widths_sum
5484	6	5484	1	0.000	False	False	0.000000	1	[0]	0
5484	6	5484	2	-10.800	False	False	0.000000	1	[0]	0
5484	6	5484	3	-149.776	True	False	-1.634835	1	[10]	10
5484	6	5484	4	-19.020	True	False	-0.157031	1	[4]	4
5484	6	5484	5	0.000	False	False	0.000000	1	[0]	0
5484	6	5484	6	0.000	False	False	0.000000	1	[0]	0
5484	6	5484	7	-10.348	False	False	0.000000	1	[0]	0

Figure 3.4: Analysis results for a single event.

### 3.5 Multi strip analysis

Starting from single strip analysis results in tabular form, other features common to a single event are defined:

- **total event height:** sum of the minima of all fired strips in such event;
- **total event charge:** sum of the charge collected by all fired strips in such event;

- **cluster size:** maximum value of contiguous fired strips for an event;
- **central-strip-computed cluster size:** number of contiguous fired strips in all events for which the charge collected on the central strip (strip no. 3, in this particular case) has the maximum value. While working with a reduced sample of events, this method allows us to neglect *border losses*, i.e. events for which the triggering muon crosses the gap near the outer strips (strips no. 1 and no. 7) and part of the charge is induced on strips which are not collected to the readout system, resulting in an incorrect measure of both total event charge and cluster size.

### 3.6 Height spectrum

For every signal, the pulse height is defined as the opposite of the minimum value of the flattened signal, multiplied by an `adc_to_mV` coefficient set by the used digitizer. For every event, the event height is defined as the maximum of all the strip heights. The height of a signal gives information about the development of avalanche and streamer phenomena inside the gap. Height spectra for all strip and event height at a fixed applied voltage are shown in Figure (3.5). The HV value has been chosen as the closest to the RPC-mixture working point, in order to have good statistics on detected signals. Left histogram corresponds to all the data collected, with no filter applied. A significant part of the histogram falls below the `fired threshold`: this part of the spectrum corresponds to strips far from the ionization process inside the chamber, and vanishes if we only consider the maximum recorded height value among the strips (right histogram).

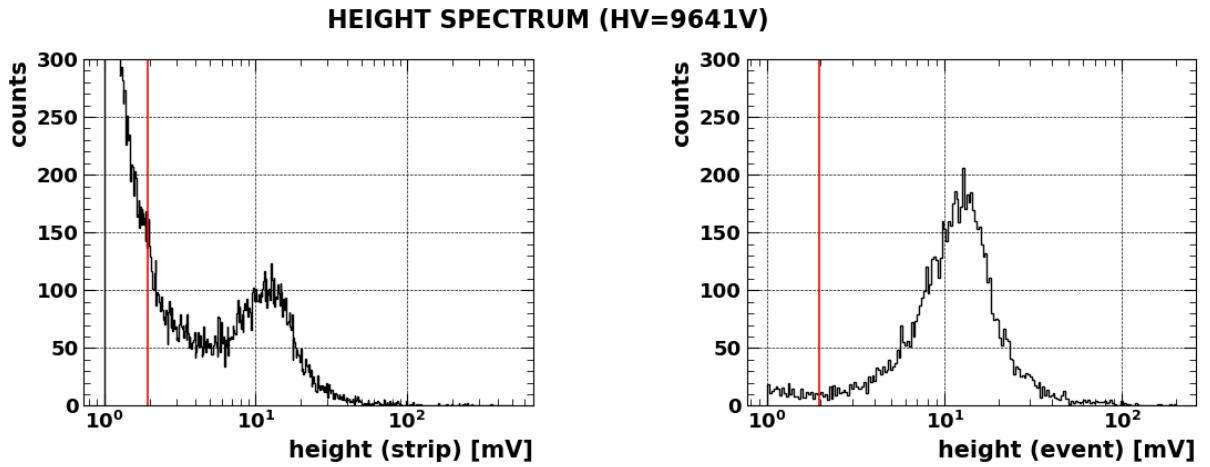


Figure 3.5: Height spectrum for a RPC operated with standard gas mixture at HV=9641V. All strip signals shown (left), maximum registered value for an event (right). The vertical red line corresponds to the `fired strip` threshold.

### 3.7 Charge spectrum

The pulse charge is a common parameter used to study detector signals, since it gives information on both the pulse height and duration. The same distinction between strip charge and event charge is made, in order to consider all the charge collected by the strips after a single scintillator trigger. The same vanishing process occurring in the height spectrum, with the exact same explanation, also happens to the charge spectrum.

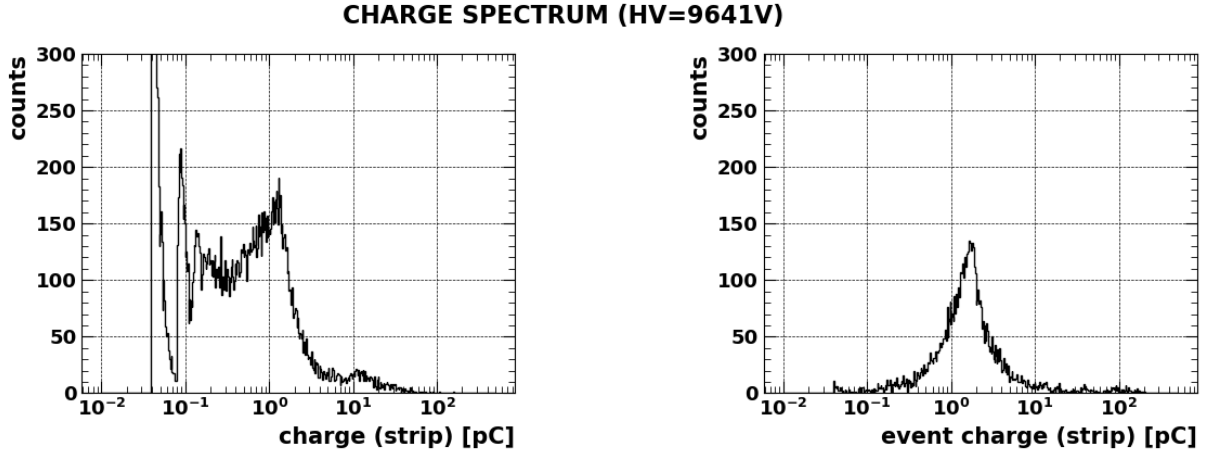


Figure 3.6: Charge spectrum for a RPC operated with standard gas mixture at HV=9641V. All strip signals shown (left), sum of the strips signals charge (right).

The collected charge spectrum changes when different HV values are applied. Spectra collected at different voltages are different both in peak position and spectrum shape, as can be seen in Figure (3.7). Two main things happen while increasing the applied HV:

- the charge spectrum shifts toward higher charge values, indicating that the ionization process produces a bigger average charge;
- the total count number increases, i.e. more primary particles are detected.

It is also worthwhile to mention that for HV=10042V a second peak can be seen; such HV value is the first one for which the number of streamer events becomes significant.

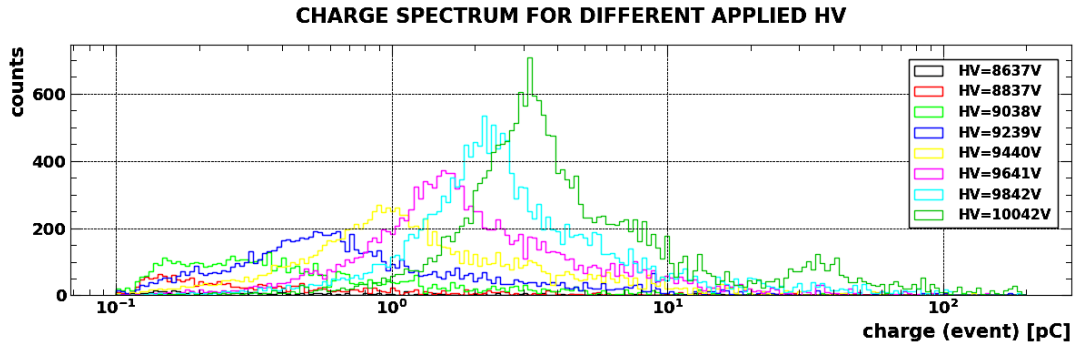


Figure 3.7: Charge spectra for a RPC operated with standard gas mixture; only events occurring near the central strip selected.

### 3.7.1 Charge-based avalanche/streamer discrimination

The event charge spectrum was fitted with a Gaus + Polya function: (referenza da mettere in chap2:

$$\text{fit\_function} = [0] \cdot \exp\left(-\frac{(x - [1])^2}{[2]^2}\right) + \max\left[0, [3] \cdot (x - [4]) \cdot [5] \cdot \exp\left(-\frac{(x - [4]) \cdot [5]}{[2]^2}\right)\right] \quad (39)$$

Data collected at HV=10442V, which shows a charge distribution with a significant number of streamers, is used for the example. Only events centered on strip 4 were considered, in order to avoid all kinds of border-effects, such as



charge loss or charge reflection due to induction on external strips. For each charge value, the error on the number of counts has been estimated by

$$\sigma_{counts} = \max\left(1, \sqrt{counts}\right)$$

where the  $\max(1, \dots)$  operation is necessary in order not to have zero-error points, which are troublesome for fit purposes. Fit results for the two different populations in the event charge spectrum are shown in Figure (3.8). The streamer distribution function is null for charge values below 10pC; the avalanche distribution function, on the other hand, goes to zero for increasing charge. In order to set the avalanche-streamer threshold value, two probability functions were constructed starting from the fit functions of the two populations. For a set value of event charge  $\bar{q}$ , the probabilities for the event to be an avalanche event or a streamer event are respectively

$$P(\text{avalanche}) = \frac{\text{fit\_function}(\text{avalanche}, \bar{q})}{\text{total\_fit\_function}(\bar{q})} \quad (40)$$

$$P(\text{streamer}) = \frac{\text{fit\_function}(\text{streamer}, \bar{q})}{\text{total\_fit\_function}(\bar{q})} \quad (41)$$

A plot of the probability functions is shown in Figure (3.8). The probability of an event being an avalanche goes to 1 for event charge values below 10pC, and the probability of it being a streamer does the same for charge values above 30pC. The two probability functions both have nonzero value in the (15-25)pC region. The avalanche-streamer threshold is set as the charge value for which  $P(\text{avalanche}) = P(\text{streamer})$ , and it is equal to  $q_t = 19.1\text{pC}$ , in accordance with Raether's limit.

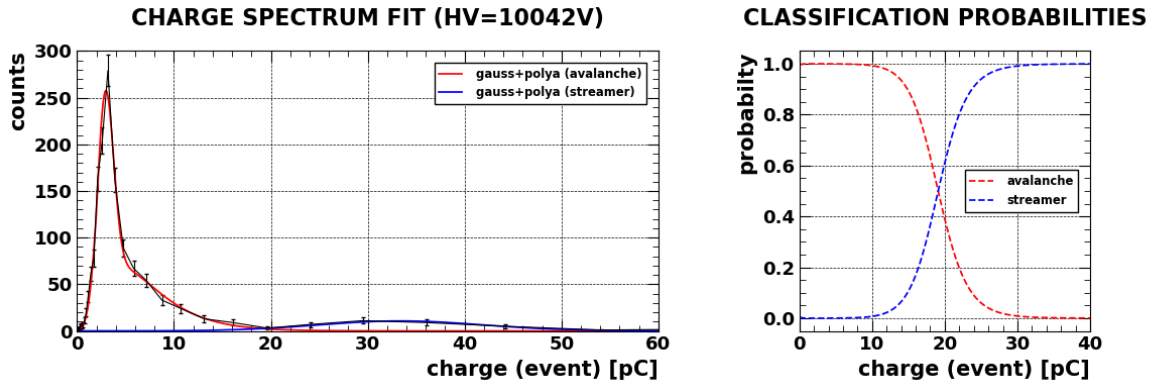


Figure 3.8: Charge spectrum for a RPC operated with standard gas mixture at HV=10420V. Data fit with two-peak function (left), event charge based classification probabilities (right).

### 3.7.2 Describing the charge distribution

The charge distribution, as can be seen by Figure (3.8), is not symmetrical. Two different parameters can be extracted from the distribution in order to compare different mixtures:

- the average charge  $\bar{q}$  gives no information on the distribution itself, but is strictly correlated to the current flowing through the RPC, thus playing a key role on the voltage drop in high irradiation condition, as will be seen in chapter 4;
- the *most frequent charge*  $q_{mf}$ , defined as the charge value corresponding to the peak of the distribution, gives an overview of the distribution evolution with increasing applied voltages, by highlighting the peak shift.

Together with the most frequent charge, an error on the peak position is defined, by fitting the low charge part of the charge spectrum with a gaussian function and defining the gaussian standard deviation as the error.

### 3.8 Cluster size

For each event, the cluster size is defined as the maximum number of contiguous fired strips. The same definition, applied only to those events for which most of the charge was collected on strip 4, reduces the statistical pool but only considers events which happen in a part of the detector where the induced charge was totally induced on strips connected to the readout system. A difference between the two approaches can be seen in figure (3.9): apart from the total number of counts, the main difference is that the relative counts between 1-size and 2-size events are inverted. This can be explained by considering the fact that events close to the border may induce charge on an external strip not connected to the readout system: if, for example, an avalanche process fires strips 1 (connected to the readout system) and 0 (not connected to the readout system), the true value for the event cluster size is 2, but the computed cluster size is 1.

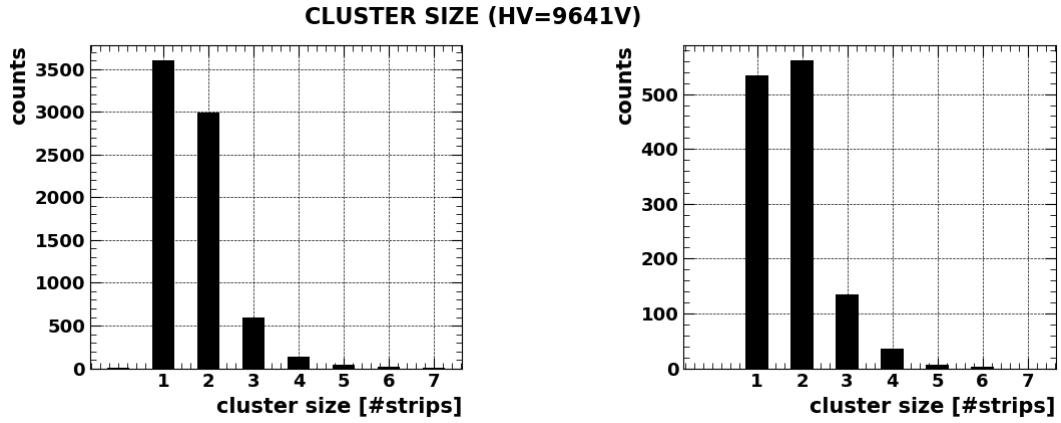


Figure 3.9: Cluster size distribution using all selected events (left); cluster size distribution computed using only events occurring near the central strip (right).

### 3.9 Time resolution

As mentioned before, when an ionizing particle passes through both scintillators a trigger signal is produced, and the corresponding time window recorded by the digitizer is saved on file. Let  $t_{tr}$  be the trigger position inside the time window. If we consider the ideal case in which *the trigger position is constant* and the ionizing particle starts the ionization process *always in the same position while crossing the gap, with instantaneous charge multiplication process*. Both  $t_{tr}$  and the time of the event record on a fired strip ( $t_s$ , defined as the time corresponding to the signal's minimum) are then uniquely defined and equal for all crossing particles. In reality, the trigger position can change of a few ns from event to event because of latency times of the used electronics. Moreover, the primary ionization doesn't happen at a unique fixed position, and the charge multiplication process requires a certain amount of time, different from avalanche to avalanche being the multiplication a stochastic process; the charge developing time is then not constant, but follows a certain distribution function with a mean value and a certain spread. The difference between the time of the minimum and the time of the trigger is then not constant for all signals, but distributed around a certain mean value with a certain spread. The spread is related to the difference in the charge development time from event to event, and it is referred to as *time resolution*.

A problem which needs to be taken into account is the difference between avalanche events and avalanche precursors followed by a streamer formation. In such a case, the time of the minimum corresponds to the streamer time, and the difference between the time of the minimum and the time of trigger increases, creating a tail in the time distribution  $t_s - t_{tr}$  distribution. The tail is very low on counts and does not create a problem for fit purposes when it comes to standard mix, but can become significant if the streamer probability increases, which will be the case for

some of the mixtures tested and described in chapter 4. In such a case, the time resolution is defined as the spread of the  $t_s - t_{tr}$  distribution corresponding to avalanche events only, with avalanche-streamer discrimination based on the total event charge.

The trigger time distribution for a single RPC operated with standard mixture at 9641V is shown in Figure (3.10-left). The trigger time isn't fixed, but it has a quasi-uniform distribution between timesamples 335 and 341. The time spectrum fit to extract the time resolution is also shown in Figure (3.10-right). The time distribution can be fitted using a gaussian function, with a  $\sigma$  value of  $1.59 \pm 0.03$  timesamples ( $3.18 \pm 0.06$ ns).

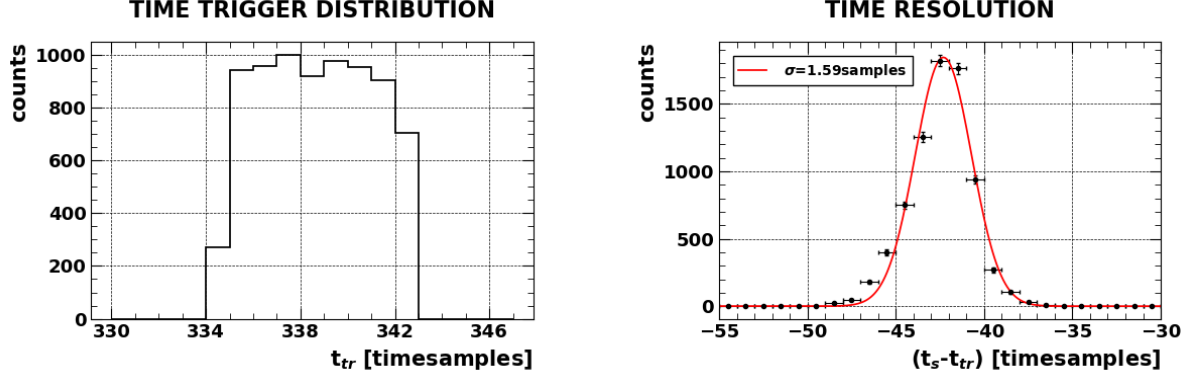


Figure 3.10: Distribution for trigger time (left); fit of the time(minimum) - time(trigger) spectrum for a RPC operated with standard gas mixture at HV=9641V.

### 3.10 Efficiency

The definition of efficiency is strictly correlated to the definition of *detected* event. For the current analysis, a crossing muon is considered detected if the corresponding event has least one strip that satisfies the conditions `fired==True` and `reflection==False`. Efficiency is defined as the number of detected muons, divided by the total number of muons which crossed the detector in the readout zone.

$$\varepsilon = \frac{\#(\text{detected events})}{\#(\text{scintillator triggers})} \quad (42)$$

The error on the efficiency is given by the error of a binomial distribution:

$$\varepsilon_{err} = \sqrt{\frac{\varepsilon \cdot (1 - \varepsilon)}{\#(\text{scintillator triggers})}} \quad (43)$$

### 3.11 Streamer probability

Among all detected events, a distinction is made between avalanche and streamer events using the event charge threshold introduced before. The streamer probability is defined as the number of events classified as streamers, divided by the number of the total detected events.

$$SP = \frac{\#(\text{streamer events})}{\#(\text{detected events})} \quad (44)$$

$$SP_{err} = \sqrt{\frac{SP \cdot (1 - SP)}{\#(\text{detected events})}} \quad (45)$$

Both efficiency and streamer probability increase with increasing value of the applied voltage. The higher the voltage, the higher the electric field inside the gap, the larger the probability that the charge produced after the primary ionizations is enough for the readout system to record signals that pass the *detected* test. The detector efficiency goes to almost 1 (*every crossing muon is detected*) for high HV values. The streamer probability is less than 1% for all applied voltage values below 9641V, but increases rapidly after that value.

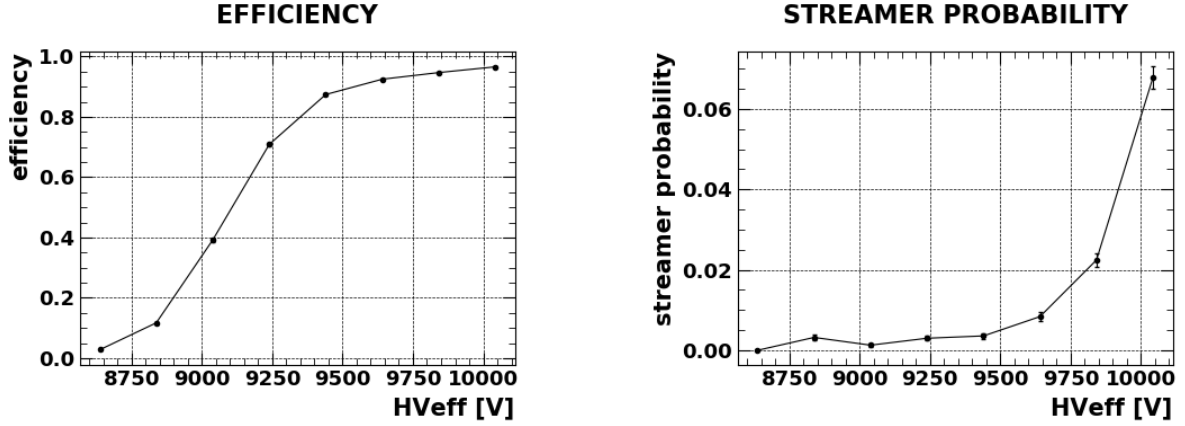


Figure 3.11: Efficiency and streamer probability for a RPC operated with standard gas mixture.

### 3.12 Fit of the efficiency curve

The efficiency curve of an RPC has been found to follow a sigmoidal shape [23]:

$$\varepsilon(\text{HV}_{\text{eff}}) = \frac{\varepsilon_{\text{max}}}{e^{\gamma(\text{HV}_{\text{eff}} - \text{HV}_{50})}} \quad (46)$$

where  $\varepsilon_{\text{max}}$  is the asymptotic efficiency for  $\text{HV}_{\text{eff}} \rightarrow +\infty$ ,  $\text{HV}_{50}$  is the voltage value corresponding to efficiency equal to half of the maximum efficiency and  $\gamma$  is a coefficient proportional to the inflection point of the sigmoid. Formula (46) is particularly useful to fit experimental efficiency points since the three fit parameters contain important information about the efficiency curve: the plateau value  $\varepsilon_{\text{max}}$ , the position of the center of the efficiency curve itself and its slope, estimated by means of  $\gamma$ . Two other parameters that can be computed from the fit results are the mixture *knee* and *working point*, defined respectively as the voltage values corresponding to 95% of the maximum efficiency and the knee voltage plus 150V.

The use of sigmoid functions provides a uniform way to compare performance of different chambers and different gas mixtures to build relative statistics. Different mixtures are usually compared by means of their knee and working point HV values, and by means of their foremost parameters (average charge, ...) evaluated at the mixture working point. Different mixtures have different performances at different applied HVs; evaluating the foremost parameters at knee voltage value removes the HV dependency and allows to compare how different mixtures perform *at the same detection efficiency condition*.

The streamer probability curve can also be fitted; if one were to increase the applied HV voltage over and over, streamer probability would get higher and higher and then saturate to  $\varepsilon_{\text{max}}$  value (*all the detected events are streamer events*). HV scans are usually interrupted once efficiencies near  $\varepsilon_{\text{max}}$  are reached, both because the important mixture parameters don't require higher voltages and not to damage the RPC gap. The streamer probability curve is then usually almost flat, with an exponential like rise for voltage values above the knee voltage; for higher voltages, given the saturation effect, the streamer curve would also have a sigmoidal shape, but for voltage values usually applied the curve can be fitted using an exponential function. The fit operation allows to construct a continuous (voltage, streamer probability) curve that can be useful to extract streamer probabilities at working point in order to

compare different mixtures. In particular, the derivative of the curve at knee and working point voltage allows to get an estimate of the streamer probability stability.

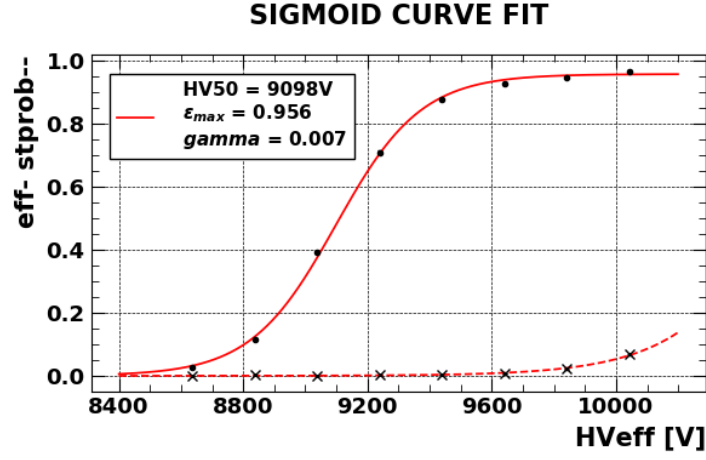


Figure 3.12: Sigmoid fit of an efficiency curve and exponential fit of a streamer curve for a RPC operated with standard gas mixture.

### 3.13 Full run results

The parameters listed above are computed for all the applied voltage values. Run results are summarized in Figure (3.13) and in Table (3.2).

knee [V]	eff [%]	stprob [%]	stprob'	$\bar{q}$ [pC]	csize [#strips]	time_res [ns]
9502	90.8	0.5	2.3e-5	2.87	2.17	3.24

Table 3.2: Foremost parameters for a RPC operated with standard gas mixture at knee voltage value.

wp [V]	eff [%]	stprob [%]	stprob'	$\bar{q}$ [pC]	csize [#strips]	time_res [ns]
9652	94.0	1.0	4.8e-5	3.93	2.36	3.18

Table 3.3: Foremost parameters for a RPC operated with standard gas mixture at working point value.

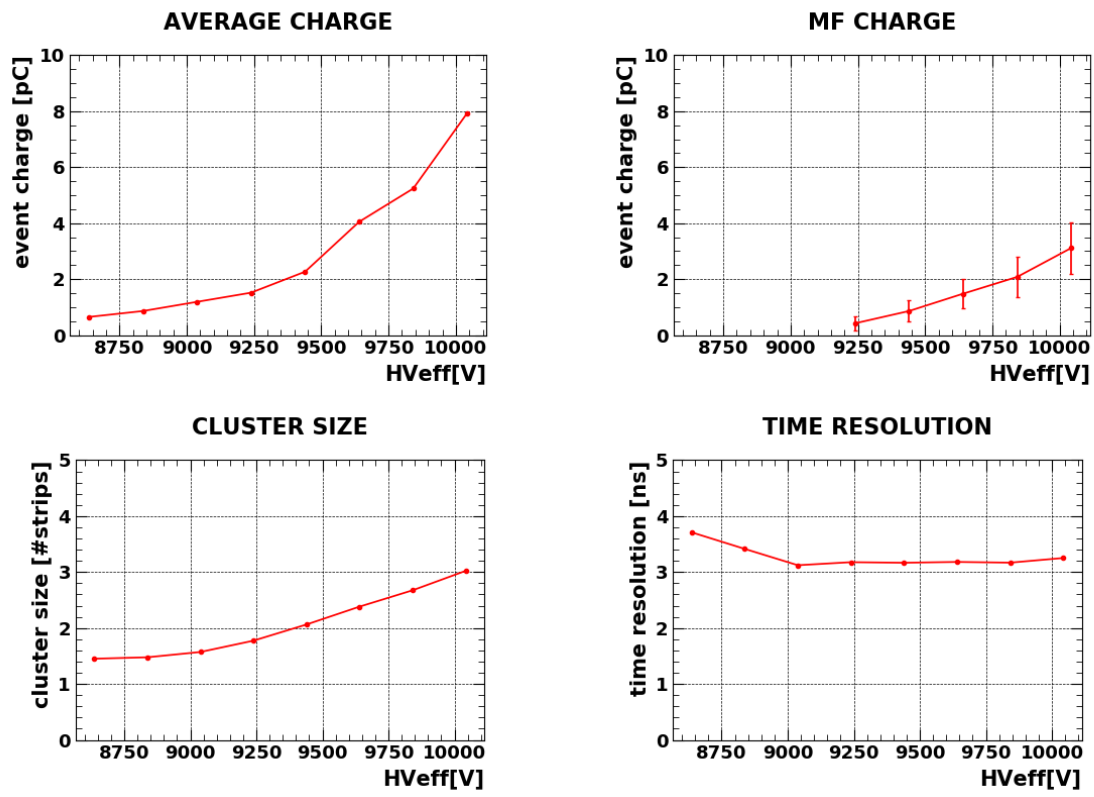


Figure 3.13: Foremost parameters for a RPC operated with standard gas mixture at different applied voltages.

# RPC PERFORMANCE WITH ECO FRIENDLY GAS MIXTURES

---

This chapter illustrates RPC performance with new eco-friendly gas mixture. The data is analysed in the same way as described in chapter 3. Every tested gas mixture performance is then compared to the standard one.

The standard gas mixture components which have a major impact on the total mixture GWP are  $C_2H_2F_4$  and  $SF_6$ , with global warming potential of 1430 and 23900 respectively. Low GWP gas mixtures are obtained by substituting, partially or totally, one of those two components. Regarding the  $C_2H_2F_4$  reduction, the tested mixtures were created by a partially replacing it with low GWP inert gases (He,  $CO_2$ ), with another gas used in the refrigerant industry (known as R-1234ze), or by a combination of them. 3M<sup>TM</sup> Novec gases, already used in power plants as electrical insulators, were tested as alternatives to  $SF_6$  because of their low GWP and high electronegativity.

## 4.1 Novec4710

3M<sup>TM</sup> Novec<sup>TM</sup> 4710 [24] is a sustainable alternative to Sulfur Hexafluoride ( $SF_6$ ) for electrical equipment insulation. It offers excellent dielectric properties, a wide range of operating temperatures and has a GWP of 2100 which, despite being very high, is less than one tenth of the  $SF_6$ 's one. Different Novec4710 concentrations (N4710 from now onwards) were tested.

$C_2H_2F_4$ [%]	$iC_4H_{10}$ [%]	N4710 [%]	GWP mix	mix label
95.40	4.50	0.10	1365	N4710_010
95.35	4.50	0.15	1366	N4710_015
95.28	4.50	0.22	1366	N4710_022
95.20	4.50	0.30	1367	N4710_030
94.90	4.50	0.50	1369	N4710_050
94.70	4.50	0.70	1370	N4710_070

Table 4.1: Novec4710 tested mixtures.

### 4.1.1 Efficiency and streamer probability

Efficiency and streamer probability curves of the different mixtures are shown in Figure (4.8), with darker green lines for higher N4710 concentration; standard mixture is shown for comparison purposes. Streamer probabilities are represented versus the shift with respect to the working point, so that the value crossing the  $x=0$  line corresponds to the streamer probability at working point for each mixture. All N4710 mixtures except for the one with 0.10% on N4710 concentration have a higher working point than the standard mixture. Streamer probabilities are comparable

to the standard mixture's one, with three mixtures (N4710\_010, N4710\_022, N4710\_030) showing a streamer probability equal or less than the streamer probability of the standard mixture at working point. As for N4710\_010, we can however notice that for  $(H_{\text{Veff}} - W_P) = 0$  the streamer curve grows more rapidly than the standard mixture with increasing HV, thus indicating a faster change in streamer rate in case of applied voltage fluctuations.

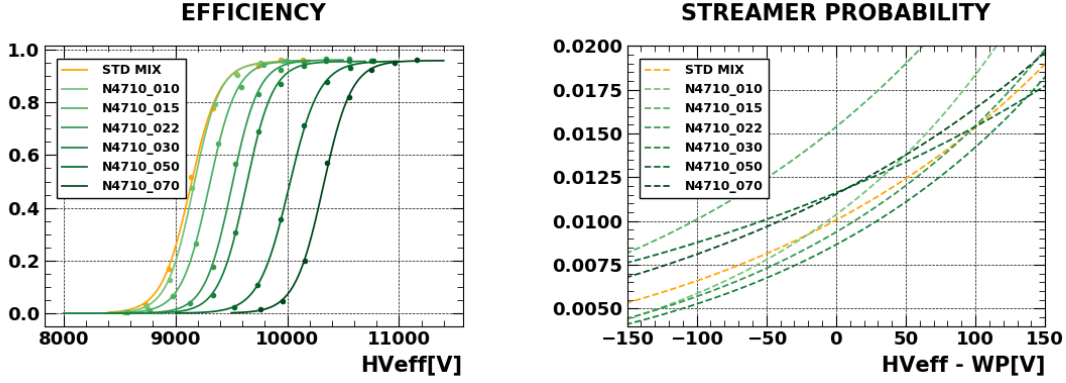


Figure 4.1: Efficiency and streamer probability curves for standard mixture and Novec4710 mixtures.

#### 4.1.2 Collected charge

The average collected charge is shown in Figure (4.2); once again, the collected charge for each mixture is represented as a function of the shift with respect to the mixture's working. No clear differences can be seen between the average collected charge per event case. The same holds for the position of the peak of the charge spectrum, which shifts toward higher charge values with the same speed as the voltage difference between the electrodes is increased.

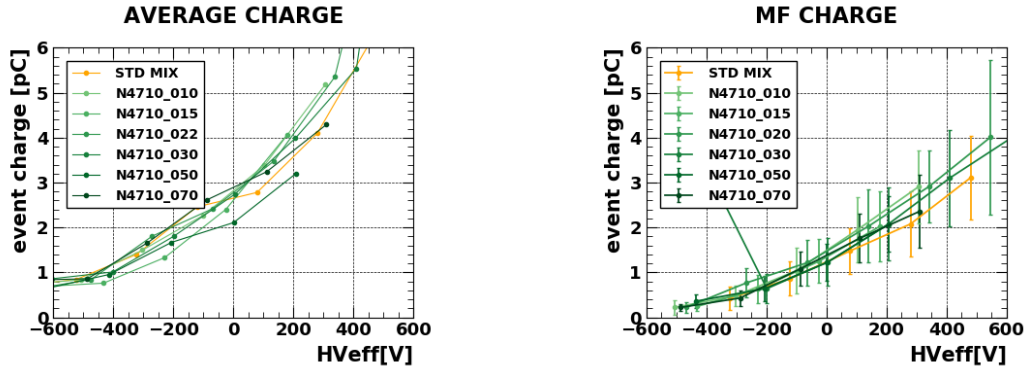


Figure 4.2: Average event charge (left) and peak position of the avalanche distribution (right) for different Novec4710 mixtures.

The fact that the average event charge at working point is the same for all mixtures may seem in contrast with the different streamer probabilities at working point. For all N4710 mixtures, the evolution of the charge spectrum is very similar to the evolution of the standard one; in particular, the streamer probability at working point is  $\sim 1\%$ ; the average charge is thus dominated by the low-charge part of the spectrum, while the streamer probability is evaluated by counting the number of events in the tail of the charge distribution. The average collected charge is therefore poorly correlated with the streamer probability of the mixture. A better understanding of the average charge-streamer probability correlation can be given by the box and whiskers plot shown in Figure (4.3). The box and whiskers plot allows to show information on both the median charge value and on the charge distribution itself,



with box borders corresponding to the 25<sup>th</sup> and 75<sup>th</sup> percentile of the distribution, "+" markers corresponding to the distribution *outliers* and markers density proportional to the outliers counts. Charge distributions at different HV values for standard mixture and for N4710\_030 mixture are shown, with an horizontal line corresponding to the avalanche-streamer threshold and a vertical line corresponding to the mixture working point. We can see that, despite having the same average value, the charge distribution for N4710\_010 is more compact and has no outliers above the threshold line, while the standard mixture distribution has some outliers above the threshold line event for an applied voltage slightly lower than its working point. It is important to stress that no outliers does not mean that no values at all above the threshold are present; "+" markers don't provide a quantitative measure of the counts, but just provide a relative measure, that allows to see that standard mixture at working point has more values over threshold than N4710\_030 mixture.

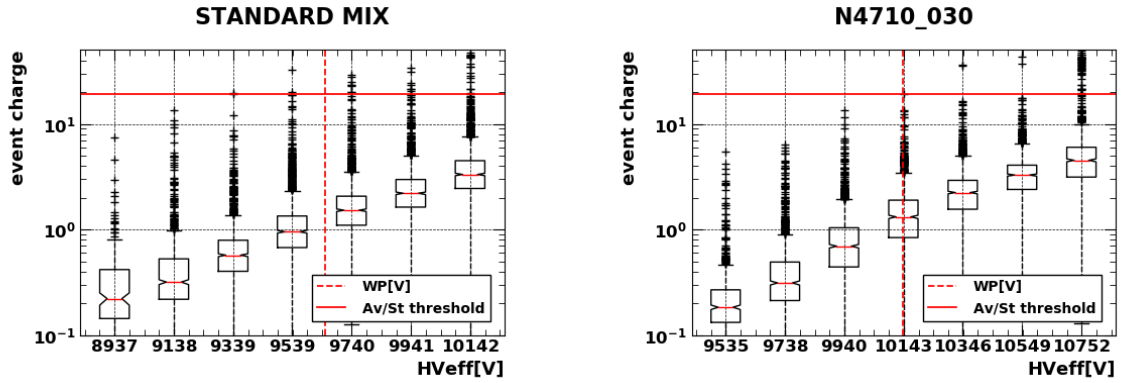


Figure 4.3: Average event charge for standard mixture and Novec4710\_030 mixture; horizontal line corresponding to the avalanche-streamer threshold; vertical line corresponding to the mixture working point.

#### 4.1.3 Cluster size and time resolution

Cluster size and time resolution do not show significant differences with respect to the standard mixture. Errors, of the order of 0.1strips for cluster size and of 0.1ns for time resolution, are not shown in Figure (4.4) for a better understanding of the plot. Cluster size does not show a clear relation with the Novec4710 concentration, as can better be seen in Figure (ref a csize vs percent in summary). Time resolution is higher for Novec4710 mixtures than for the standard one, and increases (i.e. the detection time distribution gets broader) for voltage values above the working point.

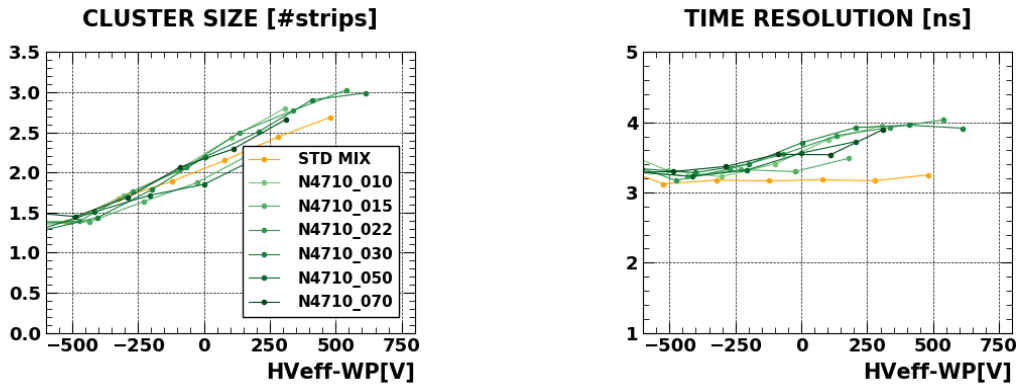


Figure 4.4: Cluster size (left) and time resolution (right) for Novec4710 mixtures.

#### 4.1.4 Summary

A summary of the foremost parameters at working point for each Novec4710 tested concentration can be found in Figures (4.5), (4.6), (4.7), and in Table (4.2). Results can be resumed this way:

- the working point shifts linearly with the N4710 concentration, with an average increase of about 2000V per percentage point;
- streamer probability does not show a precise trend with respect to the N4710 concentration, but it is always very low (less than 1.5%);
- the relative streamer probability variation, computed as the ration between the streamer probability curve derivative at working point of a mixture divided by the streamer probability curve derivative at working point of the standard mixture, shows that the streamer rate changes more slowly for all N4710 mixtures with concentration 0.2% or higher;
- cluster size and time resolution are very similar for all the tested mixtures, with values falling within each others' errors.

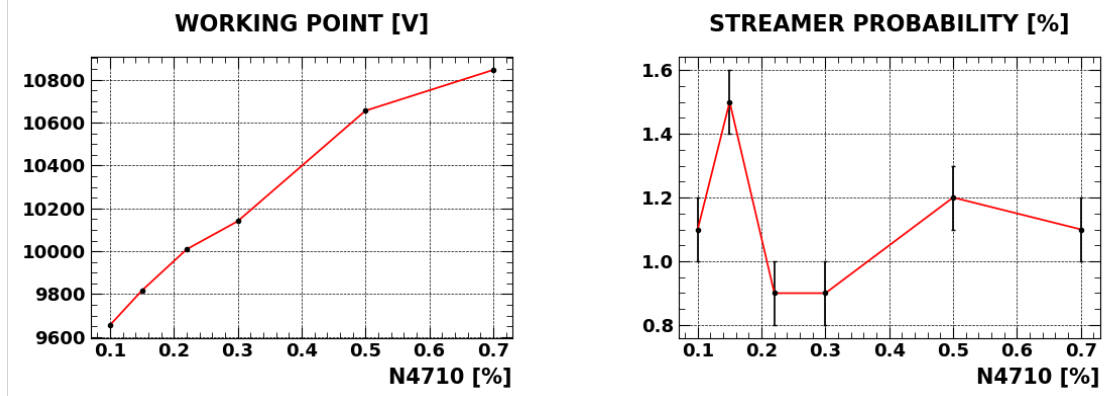


Figure 4.5: Working point (left) and streamer probability (right) for a single RPC operated with different concentration of Novec4710.

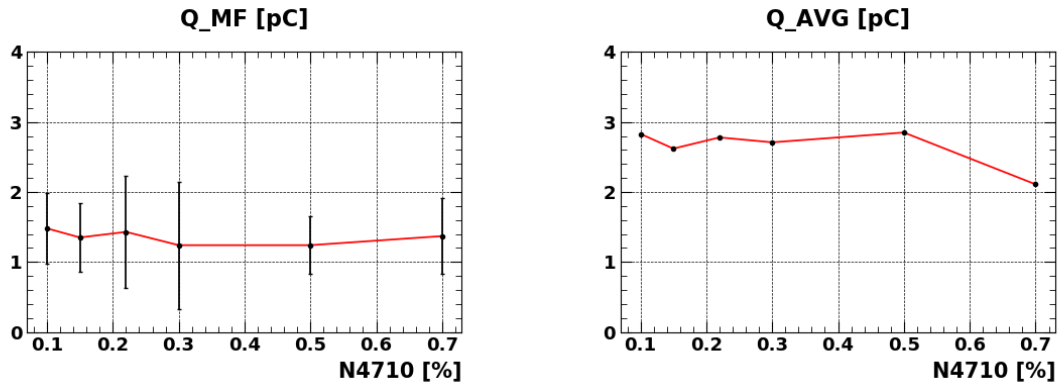


Figure 4.6: Streamer probability change rate with respect to standard mixture (left) and average event charge (right) for a single RPC operated with different concentration of Novec4710.

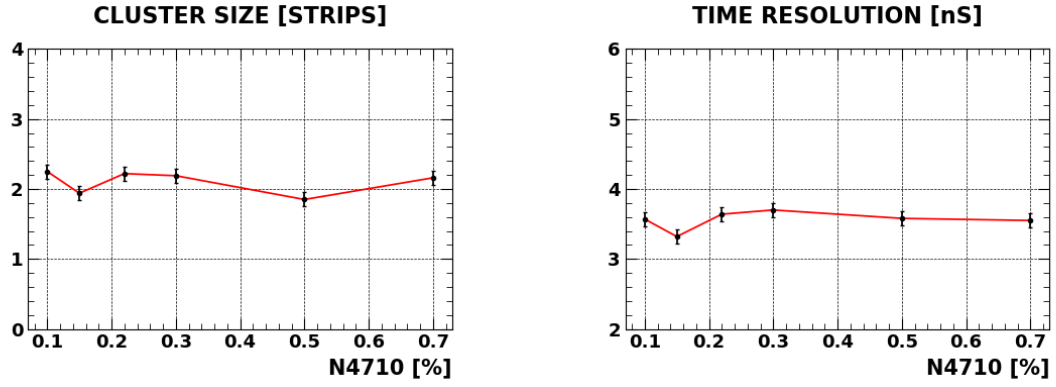


Figure 4.7: Cluster size (left) and time resolution (right) for a RPC operated with different concentration of Novec4710.

MIX	wp [V]	stprob [%]	stprob'[%/V]	$\bar{q}$ [pC]	$q_{mf}$ [pC]	csize [#strips]	time_res [ns]
STD	9652	1.0	4.8e-3	2.66	1.26	2.07	3.18
N4710_010	9664	1.1	6.2e-3	2.41	1.48	2.25	3.57
N4710_015	9807	1.5	6.2e-3	2.62	1.35	1.94	3.32
N4710_022	9997	0.9	4.4e-3	2.78	1.43	2.22	3.64
N4710_030	10140	0.9	4.3e-3	2.71	1.24	2.19	3.70
N4710_050	10562	1.2	3.3e-3	2.85	1.24	1.85	3.58
N4710_070	10837	1.1	4.0e-3	2.11	1.37	2.16	3.55

Table 4.2: Foremost parameters at working point for a RPC operated with different concentration of Novec4710.

## 4.2 Novec5110

With a GWP of less than 1 and strong dielectric properties, 3M<sup>TM</sup> Novec<sup>TM</sup> 5110 [25] gas is a sustainable SF<sub>6</sub> alternative for insulation applications leading to dramatic environmental impact reductions. The main downside of Novec5110 is its high boiling point (26.8°C against the -50.8°C of the SF<sub>6</sub>), which means that the Novec5110 is found in liquid form at room temperature and requires to be heated to be injected into the mixture. As for the Novec4710 gas, mixtures with different percentages of Novec5110 were tested.

C <sub>2</sub> H <sub>2</sub> F <sub>4</sub> [%]	iC <sub>4</sub> H <sub>10</sub> [%]	N <sub>5110</sub> [%]	GWP mix	mix label
95.2	4.50	0.30	1362	N45110_030
94.5	4.50	1.00	1352	N5110_100
93.5	4.50	2.00	1339	N5110_200

Table 4.3: Novec5110 tested mixtures.

### 4.2.1 Efficiency and streamer probability

Efficiency and streamer probability curves are shown in Figure (), the darker the blue line the higher the N5110 concentration. Unlike Novec4710 testes mixtures, streamer probabilities are not comparable to the standard mixture one. The best results are obtained with the highest reached N5110 concentration, with a streamer probability at working point of 2.1 times higher than the standard mixture one, and with a streamer rate growth 2.5 higher than the standard mixture one.

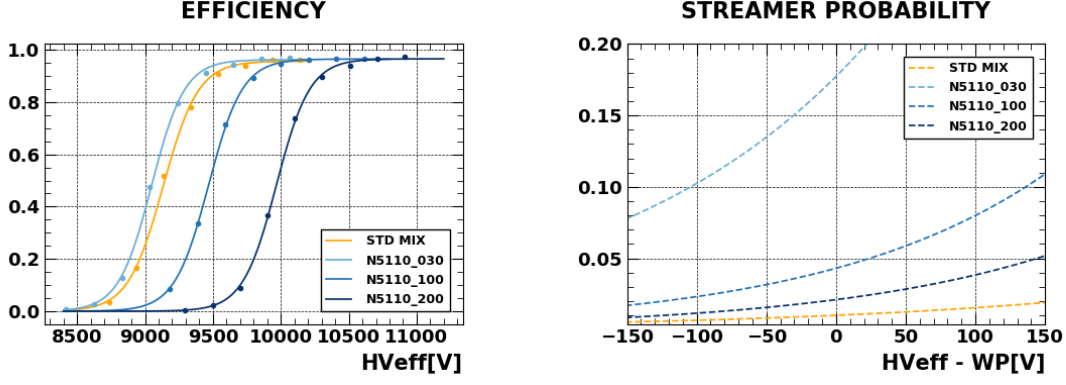


Figure 4.8: Efficiency and streamer probability curves for standard mixture and Novec5110 mixtures.

#### 4.2.2 Charge distribution

The number of streamer signals is not negligible for both the N5110\_030 and N5110\_100. The charge spectrum for N5110\_100 mixture is reported as an example in Figure (), where the counts for high-charge part of the spectrum have been multiplied by a factor 10 to enhance the plot interpretability. The streamer distribution become more and more relevant with increasing applied voltage, with streamer probability reaching 45.2% and 71.3% value for  $HV_{eff} = 10409V$  and  $10613V$  respectively.

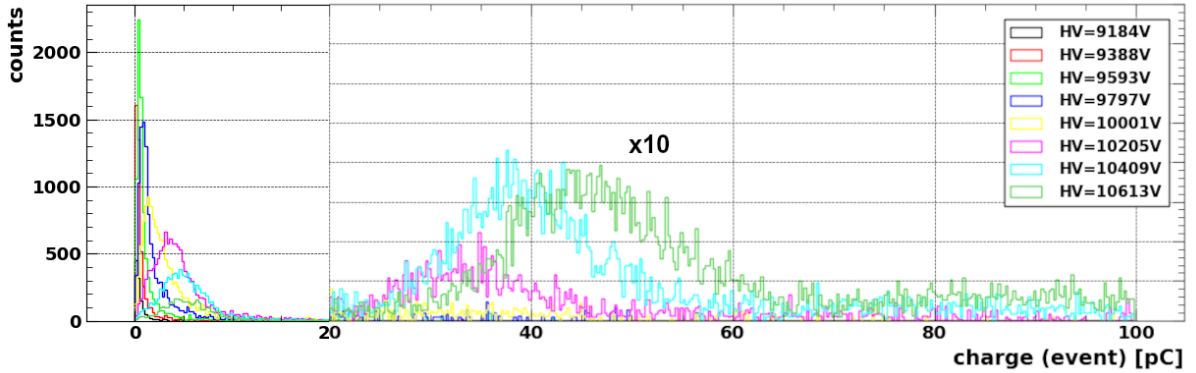


Figure 4.9: Charge spectrum for a single RPC operated with N5110\_100 mixture at different operating voltage. Counts in the  $q > 20pC$  region have been multiplied by a factor 10.

The shift of the position of the peak of the charge distribution is regular for the highest tested Novec5110 concentration, with  $q_{mf} \approx q_{mf,STD}$  for the same  $\Delta V$  from the mixture working point. The peak shift is irregular for N5110\_100 and N5110\_030: this is because the avalanche to streamer transition occurs in a larger number of events, limiting the statistics of the avalanche distribution only.

Streamer distributions can be clearly distinguished for both N5110\_030 and N5110\_100 at sufficiently high voltage values, as it can be seen in Figure () reported above. At the same  $\Delta V$  from the working point, the streamer distribution for N5110\_030 corresponds to a charge value  $\sim 1.8$  higher than N5110\_100's one.

The average induced charge is roughly the same than the standard one for low applied voltages: all Novec5110 curves are superposed to the standard one for voltages lower than (mixture working point - 400V), and the superposition continues up to the working point for N5110\_100 and N5110\_200 curves. After the working point is reached, all Novec5110 mixtures' charge increases faster than the standard mix charge. Moreover, even if the average collected charge at working point is roughly the same, Novec5110 has a higher streamer probability: once again it needs to be reminded that the average collected charge does not give a complete information on the streamer rate, which depends on the tail of the charge distribution.

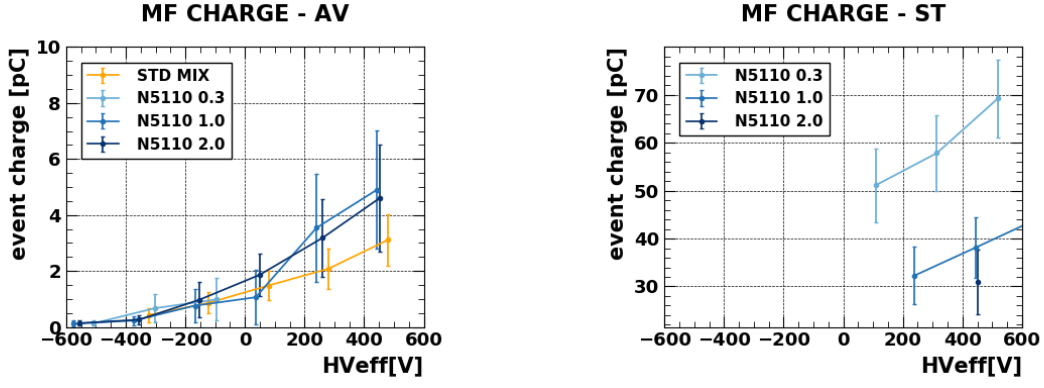


Figure 4.10: Most frequent charge value for a single RPC operated with N5110\_100 mixture at different operating voltage; avalanche distribution only (left), streamer distribution only (right).

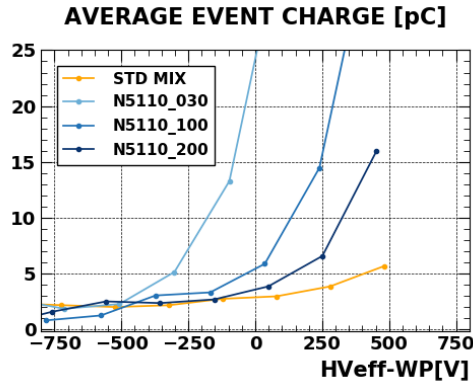


Figure 4.11: Average event charge for different Novec5110 concentrations.

#### 4.2.3 Cluster size and time resolution

The average cluster size for N5100\_030 and N5100\_200 mixtures is slightly higher than the standard mixture one, while N5100\_100 mixture has a cluster size equal to the standard mixture one, and even lower for very high applied voltage.

The time resolution is  $\sim 1.2$ – $1.3$  times higher than the standard mixture's one, with maximum value corresponding to the highest Novec5110 concentration.

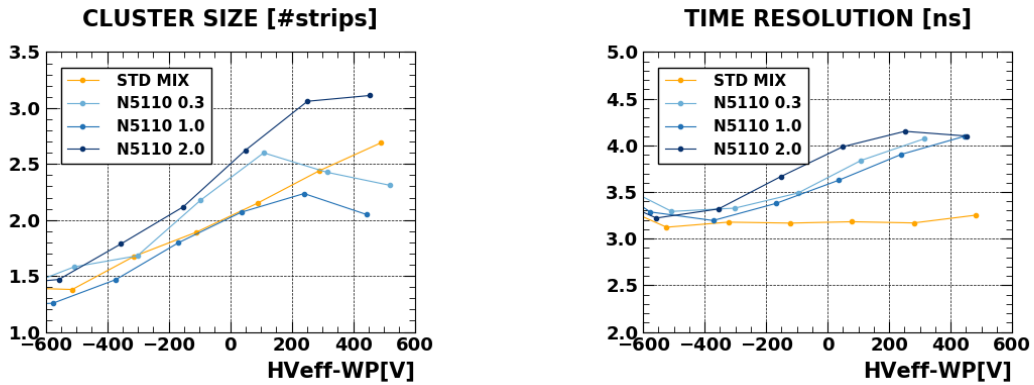


Figure 4.12: Cluster size (left) and time resolution (right) for Novec4710 mixtures.

#### 4.2.4 Summary

A summary of the foremost parameters at working point for each Novec5110 tested concentration can be found in Figures (4.13), (4.14), (4.15), and in Table (4.4). Results can be resumed this way:

- the working point shifts linearly with the N5110 concentration, with an average increase on about 500V per percentage point;
- the streamer probability decreases with the N5110 concentration, going from 17.7% for a concentration of Novec5110 of 0.3% to 2.1% for a Novec5110 concentration of 2.0%
- the time resolution shows a slight increase with the N5110 concentration, and it is on average about 15% higher than the one of the standard mixture.

Being the GWP of Novec5110 less than 1, high concentrations of this do not represent a problem for the environmental issue. The increase in the mixture's working point, though, sets a limit on the concentration, since the RPC detector has to work at operational conditions similar to the one already in use with standard gas mixture.

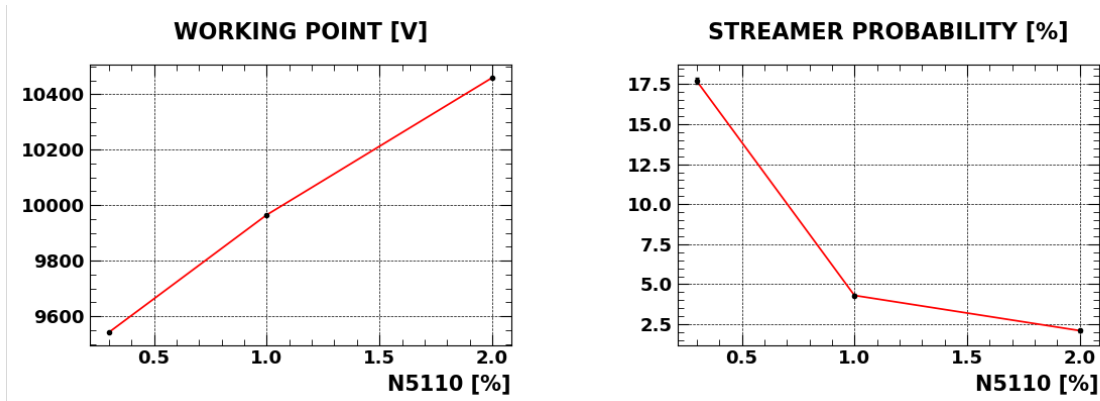


Figure 4.13: Working point (left) and streamer probability (right) for a single RPC operated with different concentration of Novec5110.

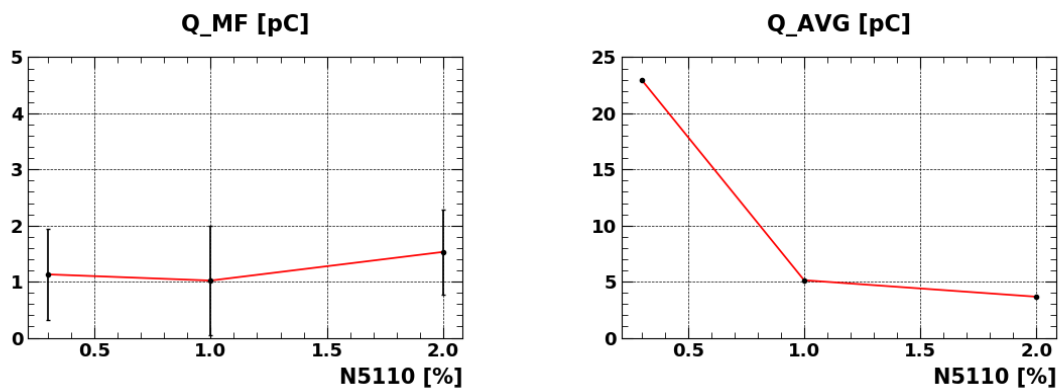


Figure 4.14: Streamer probability change rate with respect to standard mixture (left) and average event charge (right) for a single RPC operated with different concentration of Novec5110.

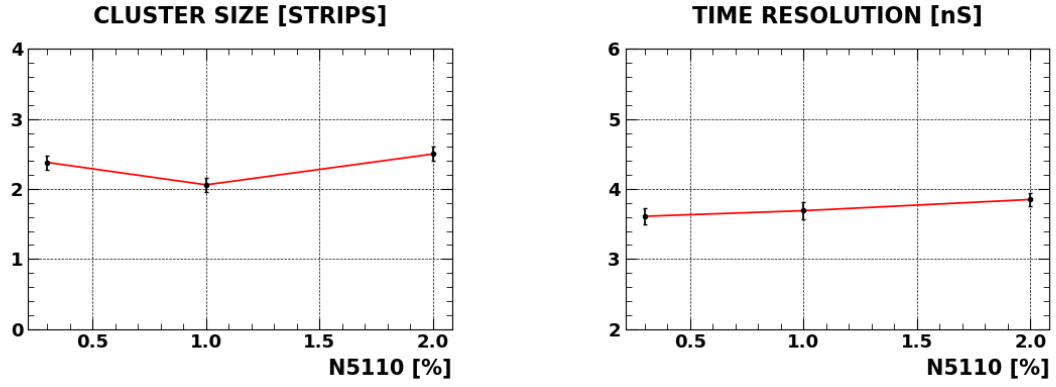


Figure 4.15: Cluster size (left) and time resolution (right) for a single RPC operated with different concentration of Novec5110.

MIX	wp [V]	stprob [%]	stprob'[%/V]	$\bar{q}$ [pC]	$q_{mf}$ [pC]	csize [#strips]	time_res [ns]
STD	9652	1.0	4.8e-3	2.66	1.26	2.07	3.18
N5110_030	9542	17.7	9.7e-2	23.2	1.13	2.38	3.61
N5110_100	9965	4.3	2.6e-2	5.13	1.02	2.06	3.69
N5110_200	10459	2.1	1.2e-2	3.66	1.53	2.50	3.85

Table 4.4: Foremost parameters at working point for a RPCr operated with different concentration of Novec5110.

### 4.3 EcoHe mixtures

Different low GWP mixtures were created with partial substitution of the R-1234a with a combination of Helium and R-1234ze. Given the decrease in the highly electronegative R-134a concentration, an increase of the  $\text{SF}_6$  concentration was necessary in order to obtain reasonable streamer probabilities. Data analysis on the two tested mixtures which were considered as suitable candidates for the standard mixture replacement is reported.

$\text{C}_2\text{H}_2\text{F}_4$ [%]	$\text{C}_3\text{H}_2\text{F}_4$ [%]	He [%]	$\text{iC}_4\text{H}_{10}$	$\text{SF}_6$	GWP mix	mix label
37.45	37.45	20	4.5	0.6	682	EcoHe20
32.45	32.45	30	4.5	0.6	610	EcoHe30

Table 4.5: EcoHe tested mixtures.

#### 4.3.1 Efficiency and streamer probability

Efficiency and streamer probability curves are shown in Figure (4.16). The best results are obtained with EcoHe20 mixture, with a streamer probability at working point of 4.4%. EcoHe30 mixture shows a higher streamer probability (6.2%) and a faster streamer probability increase.

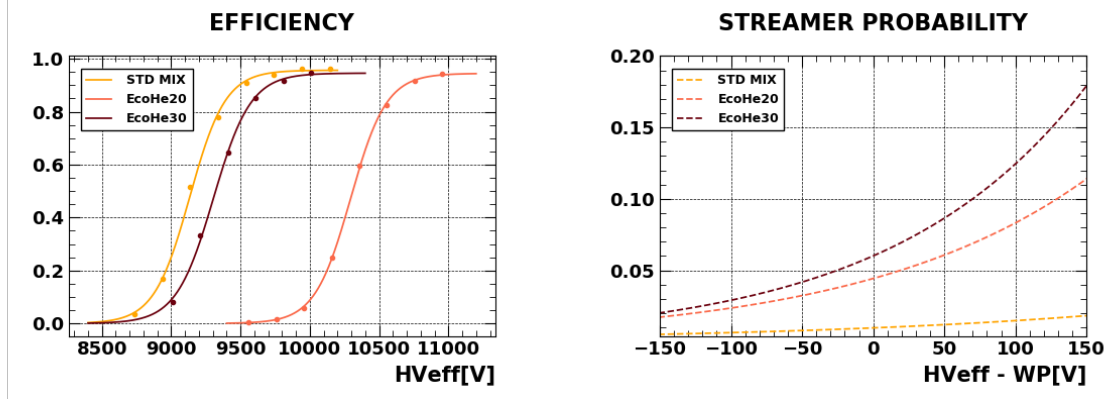


Figure 4.16: Efficiency and streamer probability curves for standard mixture and EcoHe mixtures.

#### 4.3.2 Collected charge

The induced charge is again very similar to the standard mixture's one for voltages lower than the mixture working point - 400V. When approaching the knee voltage, the charge distribution for both EcoHe mixtures is shifted toward higher charge values (Figure (4.17), right). Even if the peak of the distribution is located in the same position, the tail of the distribution, negligible for the standard mixture case, is significant for both EcoHe20 and EcoHe30 mixtures: the result is a higher average charge. For the  $V = (\text{working point} - 400V)$  case, for example, the peak position is roughly the same (superposed curves in Figure (4.17), right), but the average charge for both EcoHe mixtures is  $\sim 2$  times higher than the standard mixture's one (Figure (4.17), left)

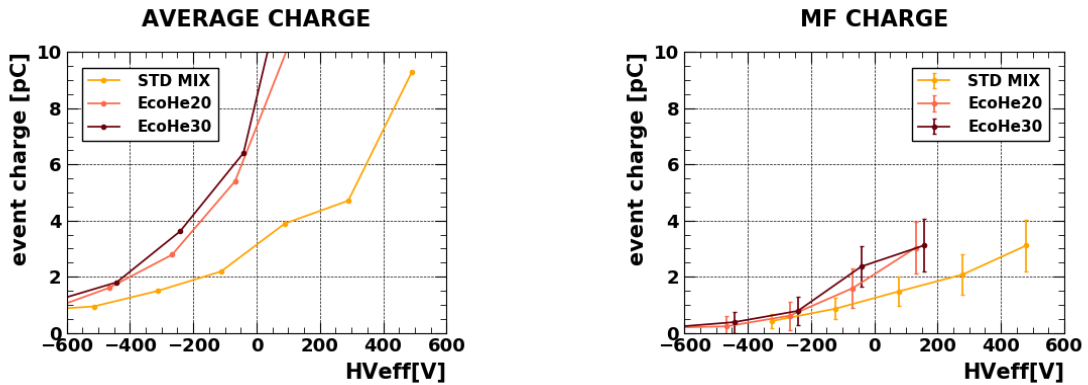


Figure 4.17: Average charge and most frequent charge for standard and EcoHe mixtures.

#### 4.3.3 Cluster size and time resolution

A cluster size comparison between EcoHe and standard mixtures is shown in Figure (4.18); as in the previous plots of the same type, errors are not shown for a better understanding of the plot, and are of the order of  $\sim 0.1$  strips for the cluster size. Cluster size for the EcoHe mixtures is higher, but is comparable to the standard mixture's one. Time resolution, on the other hand, shows a clear increase, with working point values  $\sim 1.6$  higher than the standard time resolution.



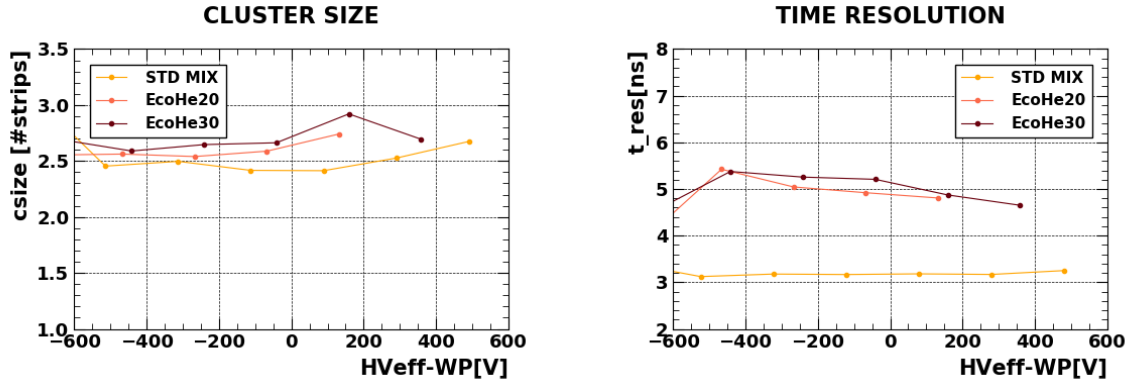


Figure 4.18: Cluster size and time resolution for standard and EcoHe gas mixtures.

#### 4.3.4 Summary

A summary of the foremost parameters at working point for the two EcoHe tested gas mixtures can be found in Table (4.6). Results can be resumed as follows:

- The GWP of the mixtures is about one half of the one of the standard gas mixture (from 1433 to 682 and 610 for EcoHe20 and EcoHe30, respectively), thanks to the replacement of R-134a with HFO and Helim;
- the streamer probability is quite high for EcoHe30 mixture (6.2%), but has an acceptable value for the EcoHe20 mixture (4.4%);
- avalanche distributions peaks are shifted toward higher charge values with respect to the peak of the standard mixture, with an increase in the peak charge value around 65% and 100% with respect to the standard mixture for EcoHe20 and EcoHe30 respectively. The average charge increase is even higher, because of the increase of the number of streamer events in the tail of the charge distribution.

MIX	wp [V]	stprob [%]	stprob'[%/V]	$\bar{q}$ [pC]	$q_{mf}$ [pC]	csize [#strips]	time_res [ns]
STD	9652	1.0	4.8e-3	2.66	1.26	2.07	3.18
EcoHe20	10823	4.4	2.8e-2	7.12	2.08	2.46	4.82
EcoHe30	9850	6.2	4.4e-2	8.42	2.54	2.61	5.13

Table 4.6: Foremost parameters at working point for a RPC operated with different concentration of Novec5110.

# THE GAMMA IRRADIATION FACILITY (GIF++)

## 5.1 Historical background

The original CERN Gamma Irradiation Facility (GIF) in CERN building 190 had been intensively used to simultaneously expose detectors to the photons from a  $^{137}\text{Cesium}$  source and high energy particles from the X5 beam line in SPS West Area. From 2004 onwards, only the  $^{137}\text{Cesium}$  (0.5 TBq) source was available for irradiation. In September 2014 the decommissioning of the facility started and the old Cs source was removed in early December 2014.

The high-luminosity LHC (HL-LHC) upgrade is setting a new challenge for particle detector technologies. The increase in luminosity will produce a higher particle background with respect to present conditions. Performance and stability of detectors at LHC and future upgrade systems will remain the subject of extensive studies. To meet these challenges, a joint project between the Engineering department (EN) and the Physics department (EP) was started to build a new Gamma Irradiation Facility. Located at the H4 beam line in EHN1, the GIF++ is a unique place where high energy charged particle beams (mainly muon beam with momentum up to 100GeV/c) are combined with a 13.5TBq  $^{137}\text{Cesium}$  source. The higher source activity produces a background gamma field more intense by a factor 30 with respect to the one at original GIF, allowing to accumulate doses equivalent to HL-LHC experimental conditions in a reasonable time. The GIF++ area is mainly composed by the actual irradiation area, a preparation zone and a two-floor area that hosts the gas systems and the electronic devices. The bunker is delimited by 1.6m thick concrete blocks that create a shielded area accessible from two sides.

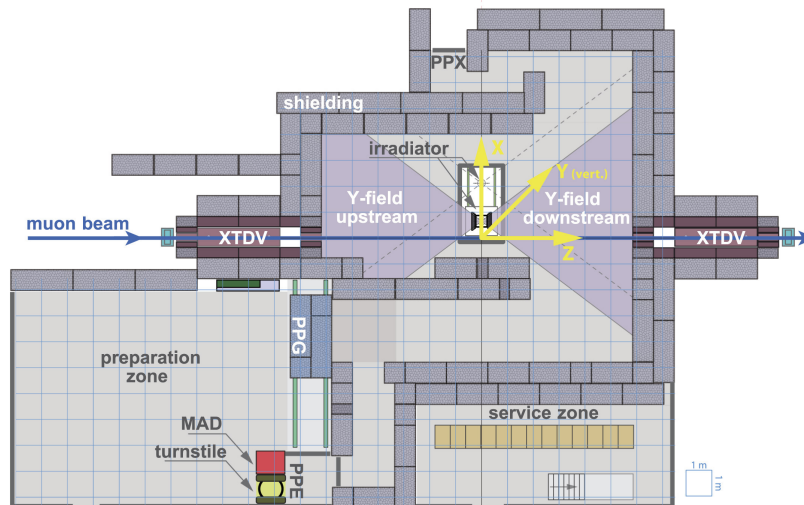


Figure 5.1: GIF++ irradiation bunker, preparation and service area.

### 5.2 Gamma irradiation field

(main source from <https://ieeexplore.ieee.org/document/7581874>) Two independent irradiation zones are present, the *upstream* and *downstream* zone, referring to their position with respect to the gamma source. The gamma source is the  $^{137}\text{Cs}$  isotope, whose spectrum is composed by primary 662keV photons and scattered photons with lower energy. This isotope was chosen for its long half-life (30.17 years) which can give a more uniform photon rate over time. The activity of the source at the beginning of the operations (March 2016) was 13.5TBq; last measured activity value (September 2020) is 12.2TBq.

The  $^{137}\text{Cs}$  source is embedded between two Tungsten blocks and can be moved vertically inside a support tube, with source OFF condition (no irradiation inside the bunker are) corresponding to the bottom of support tube itself (*garage position*). At the top of the tube (*irradiation window*), the wide opening angle of both upstream and downstream openings ( $\pm 37^\circ$ ) allows to irradiate a large fraction of the two irradiation zones. Both openings are equipped with an Aluminium angular correction lens that converts the gamma flux from a point source flux to a uniform flux on vertical surfaces at fixed distance from the source. This operation is mainly benefits large area detectors, which would otherwise be subjected to a non-uniform photon flux. For each irradiation zone, the gamma flux can be modulated independently using a system of two independent 3x3 arrays of absorption filters (ABS, from now onwards) made of paint coated Lead mounted on remotely movable supports. The ABS can be arranged to fine tune the irradiation flux from a to a total attenuation of 46415. It is however worthwhile to mention that the nominal attenuation factor corresponds to the attenuation of 662keV photons only, and that the effective attenuation of lower energy photon can differ from the nominal value.

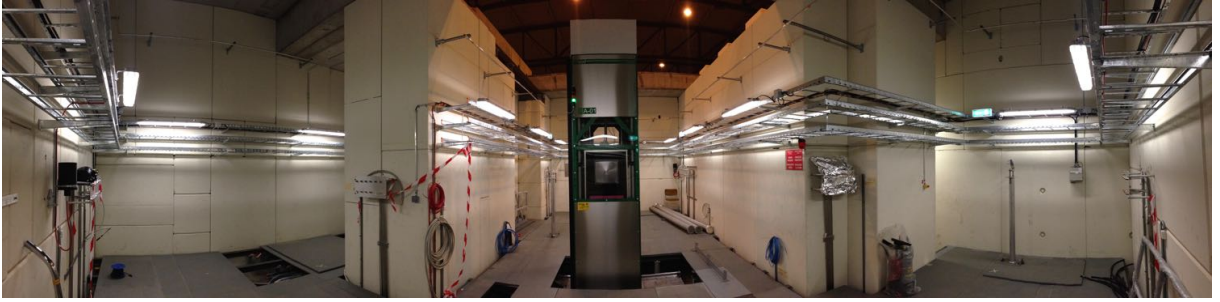


Figure 5.2: GIF++ bunker from the downstream point of view.

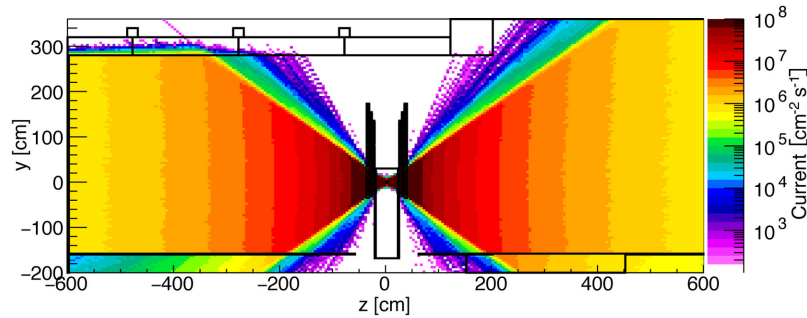


Figure 5.3: Photon current at different distances from the source; attenuation factor 1 (add source).

### 5.3 Experiment goals and experimental setup

The used experimental setup at GIF++ consists of two main parts, one situated inside the bunker and the second one located in the gas service area.

The gas system works the same way as the one described for laboratory measurements, with a few additional parts. Gas flow is regulated using mass flow controllers, that allow to create the desired mixture. The gas mixture humidity is controlled and modified via a dedicated part of the gas system: the gas line is split into two; one part goes to a tank where the mixture is forced to flow through water before being reuniting with the other line, where the non changed original mixture flows. The flow on the two lines, which are referred to as *wet* and *dry* lines respectively, is regulated again using two MFCs, one for each line, allowing to regulate the mixture humidity by controlling the relative amount of dry and wet in the final mixture.

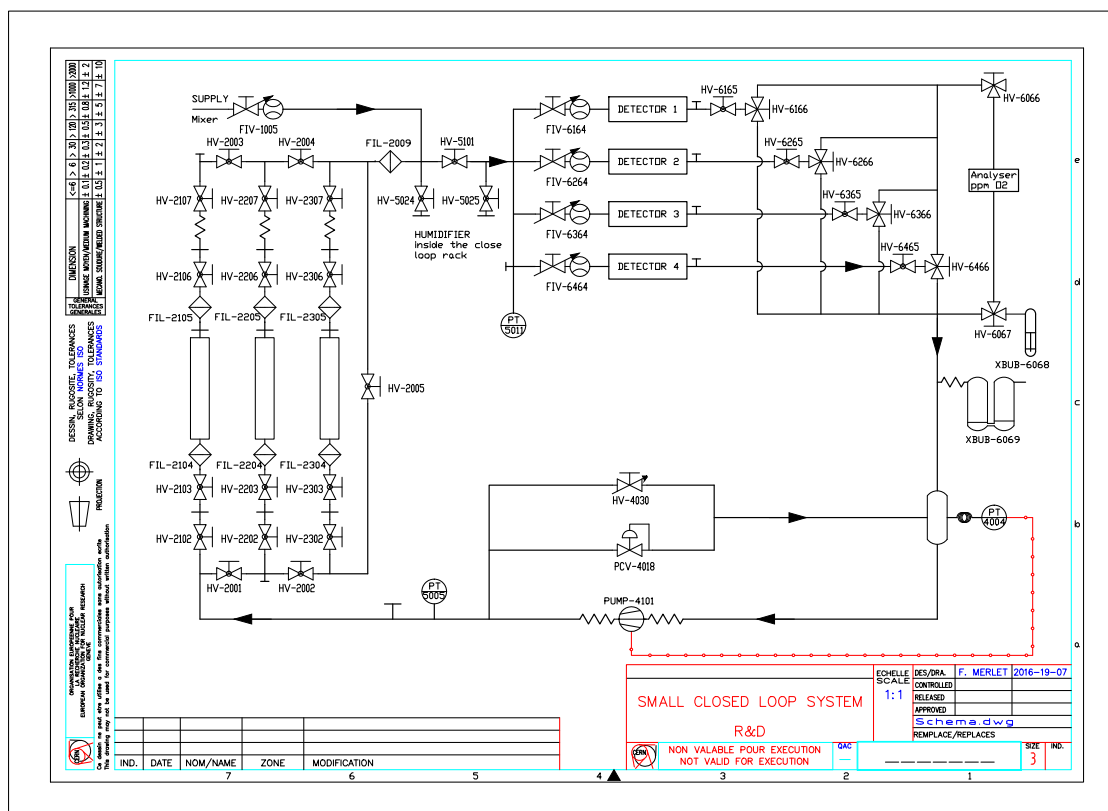


Figure 5.4: Scheme of the gas system at the GIF++.

Inside the bunker, the RPCs are installed on a metal structure which will be referred to as *trolley*, which can host up to three RPCs at the same time. The trolley can easily be moved inside the bunker, but it was kept fixed in a position such that the distance between the source and the installed RPCs was around 6m. The part where RPCs are installed can rotate around an horizontal axis of rotation, so that the RPCs can assume every position between the vertical one (perpendicular to the photon flux) and the horizontal one (parallel to the ground).

The final goal of the experiment is to understand the detectors' performance under high irradiation gamma flux and to check if they remain stable after a total integrated remains stable while a total integrated charge equal to the one expected for HL-LHC is accumulated. RPCs are therefore kept ON at working point value and currents are constantly monitored as well as the performance stability over time. The applied voltage value is corrected in real time using pressure and temperature values inside the bunker in order to keep the effective voltage fixed.

Figure 5.5: Metal structure for RPC installation inside the bunker *trolley*.

#### 5.4 Effective attenuation

In order to have a precise measure of the effective attenuation for different absorption filters, a measurement of the collected dose inside the bunker versus the set ABS was done. An estimate of the gamma flux intensity was done by measuring the dose collected at different ABS filters by a MIRION-RDS31<sup>TM</sup> dosimeter [26], installed on the RPC position inside the bunker. During the acquisition, the downstream ABS was set to 1, and it was not possible to change it. For each nominal ABS, the effective attenuation is defined as ratio between the collected dose with no filter applied (ABS=1) and the collected dose at that specific nominal ABS value.

$$\text{effective attenuation(ABS)} = \frac{\text{effective attenuation(ABS=1)}}{\text{effective attenuation(ABS)}} \quad (47)$$

The effective attenuation is lower than the ABS filter value, and it seems to saturate with increasing ABS. The maximum measured effective attenuation was 262 for a nominal filter of 46000. The background radiation is due to both low energy, non shielded photons and to backscattering process of photons emitted downstream.

nominal ABS	dose [ $\mu\text{Sv/h}$ ]	dose error [ $\mu\text{Sv/h}$ ]	effective attenuation	effective attenuation error
1.0	8778	283	1	
2.2	4143	153	2.12	0.15
6.9	1557	68	5.63	0.43
10	1056	69	8.31	0.82
46	285.9	15.5	30.7	2.7
100	155.3	10.2	56.5	5.5
220	95.19	8.98	92.2	11.7
2200	39.32	3.09	223	25
46000	33.53	1.89	262	24

Table 5.1: Measured dose and effective attenuation at different absorption filters; ABS filter downstream set to 1.



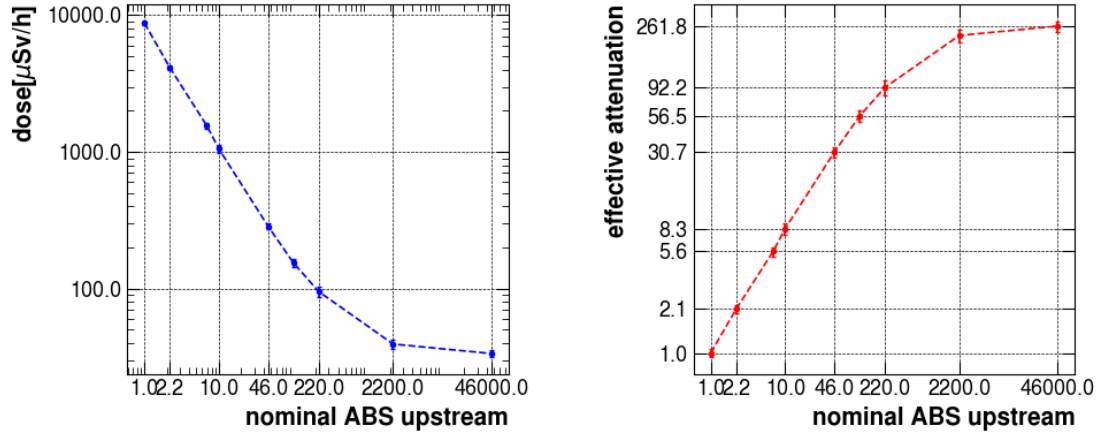


Figure 5.6: Measured dose (left) and effective attenuation (right) versus absorption filter; ABS filter downstream set to 1.

In order to construct a parameter which gave an estimate of the photon flux, the relative intensity  $\mathcal{I}_{rel}$  was defined as the inverse of the effective attenuation, so that the no filter case corresponds to  $\mathcal{I}_{rel} = 1$  and that the relative intensity decreases while increasing the nominal ABS.

$$\mathcal{I}_{rel}(ABS) = \frac{1}{\text{effective attenuation}(ABS)} \quad (48)$$

with  $ABS = +\infty$ ,  $\mathcal{I}_{rel} = 0$  corresponding to the source OFF case.

### 5.5 RPC detectors in gamma irradiation condition

As described in chapter 2, RPC detectors under high gamma irradiation flux behave in a different way than in low flux ionizing particle. Charge formation inside the gap, and so the current flowing through the RPCs, are not due to the impinging particle starting a multiplication process, but rather to the acceleration of a single electron emitted in the photon-bakelite interaction [27]. The current flowing through the RPC can be modeled by a linear function with a sharp threshold  $V_t$ , with zero-current for applied voltage lower than  $V_t$  and a linear current-voltage relation for applied voltage higher than  $V_t$ . The second linear part corresponds to a saturation part, in which any increase in the applied HV leads to a proportional increase in the flowing current in order to have a fixed voltage difference between the electrode plates. The transition from one region to the other is not sharp in reality, but can be modeled by the formula introduced in section (referenza)

$$I(V_{eff}) = \frac{1}{R_{eff}} \cdot \left[ \frac{\sigma_t}{\sqrt{2\pi}} \exp\left(-0.5 \cdot \left(\frac{V_{eff} - V_t}{\sigma_t}\right)^2\right) + 0.5 \cdot (V_{eff} - V_t) \cdot \left(1 + \operatorname{erf}\left(\frac{V_{eff} - V_t}{\sqrt{2}\sigma_t}\right)\right) \right] \quad (49)$$

with effective resistance at a given irradiation flux

$$R_{eff} = \frac{1 + X}{X} R \quad (50)$$

being  $R$  the true value of the total bakelite resistance (sum of the resistance of the two electrodes) and  $X$  a parameter proportional to the flux intensity. Using the dose measurements done for evaluating the effective attenuation,  $X$  was taken in the form of

$$X = D_0 \cdot D^\beta \quad (51)$$

being  $D$  the measured dose at a fixed ABS filter.

### 5.5.1 Definitions

Before discussing the RPCs stability over time, a clarification on the terminology is needed. Three different terms will be widely used to refer to the RPC voltage in the next paragraphs, and it is worth to precisely remind their definition.

- **HVset** is the set voltage value applied to the RPC (value set on the HV module);
- **HVeff** is the effective RPC value, corrected by measured pressure and temperature values using equation:

$$HV_{\text{eff}} = HV_{\text{set}} \cdot \frac{T}{T_0} \frac{p_0}{p} \quad (52)$$

being  $T$ ,  $p$  expressed in Kelvin and millibar respectively,  $T_0 = 293.15\text{K}$  and  $p_0 = 965\text{mbar}$ ;

- **HVgap** is the voltage drop between the electrodes, equal to the effective voltage minus the  $R \cdot I$  drop.

The correction formula has been inverted in order for the effective voltage to constant and equal to 11300V;  $HV_{\text{set}}$  is then corrected real time using pressure and temperature values inside the bunker using the Formula:

$$HV_{\text{set}} = HV_{\text{eff}} \cdot \frac{T_0}{T} \frac{p}{p_0} \quad (53)$$

### 5.5.2 Detector resistance measure

Being  $X$  a measure of the irradiation flux, we expect that both  $D_0$  and  $\beta$  have positive value, in order to have  $X$  increase when a higher dose is collected. In the limit of infinite flux

$$R_{\text{eff}} = \frac{1 + X}{X} R \longrightarrow R \quad \text{for } X \longrightarrow +\infty$$

An estimate of the electrodes' resistance can be derived by doing several HV scans at different ABS filters, by extracting the effective resistance value and then by taking as  $R$  value the one to which  $R_{\text{eff}}$  converges for increasing flux. Thus, HV scan with detectors filled both with standard gas mixture and EcoHe20 mixture have been done. A plot for the currents measured with two RPCs installed at the GIF++ facility and operated with standard gas mixture can be seen in Figure (5.7).

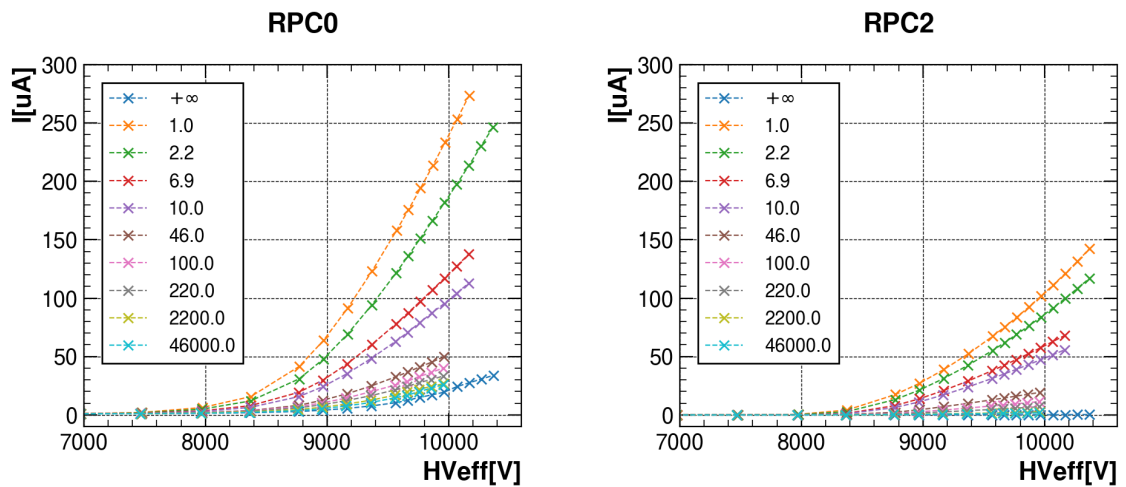


Figure 5.7: Current measured at different attenuation filters for RPC0 (left) and RPC2 (right). RPCs operated with standard gas mixture.

From the plots in Figure (5.7) it can be observed that:

- the angular coefficient of the  $(HV_{\text{eff}}, I)$  curves increases with decreasing the ABS filter, i.e. when the photon flux gets more intense. This means that the effective resistance  $R_{\text{eff}}$  decreases when the flux intensity gets higher, in accordance with equation (48);
- for a fixed  $(HV_{\text{eff}}, \text{ABS})$  condition and voltage values higher than the threshold value, the current flowing through RPC2 is roughly half of the current through RPC0. This, as will be explained in the following section, is due to the difference between RPC0 and RPC2's electrode resistances.

Fit results for the HV scans with different absorption filters for both RPC0 and RPC2 filled with standard mixture are shown in Tables (5.2) and (5.3). For both RPCs, data corresponding to source OFF condition and to the highest ABS filters could not be fit; this is not unexpected: equation (49) holds under high irradiation conditions, and doesn't provide a good description of low irradiation cases.

ABS	dose [ $\mu\text{Sv/h}$ ]	$V_t$ [V]	$\sigma_t$ [V]	$R_{\text{eff}}$ [ $\Omega$ ]
1.0	8878	$8823 \pm 17$	$596 \pm 17$	$(4.92 \pm 0.07) \cdot 10^6$
2.2	4143	$8862 \pm 14$	$598 \pm 15$	$(6.11 \pm 0.07) \cdot 10^6$
6.9	1557	$8874 \pm 29$	$597 \pm 27$	$(9.39 \pm 0.23) \cdot 10^6$
10	1056	$8907 \pm 33$	$617 \pm 29$	$(1.12 \pm 0.03) \cdot 10^7$
46	285.9	$9097 \pm 127$	$740 \pm 76$	$(1.81 \pm 0.02) \cdot 10^7$

Table 5.2: RPC0 - effective resistance at different ABS values.

ABS	dose [ $\mu\text{Sv/h}$ ]	$V_t$ [V]	$\sigma_t$ [V]	$R_{\text{eff}}$ [ $\Omega$ ]
1.0	8878	$8961 \pm 33$	$646 \pm 31$	$(1.00 \pm 0.03) \cdot 10^7$
2.2	4143	$8933 \pm 25$	$595 \pm 26$	$(1.24 \pm 0.03) \cdot 10^7$
6.9	1557	$8927 \pm 15$	$470 \pm 19$	$(1.98 \pm 0.03) \cdot 10^7$
10	1056	$8807 \pm 12$	$440 \pm 16$	$(2.45 \pm 0.03) \cdot 10^7$
46	285.9	$8744 \pm 10$	$337 \pm 11$	$(6.34 \pm 0.05) \cdot 10^7$
100	155.3	$8755 \pm 10$	$343 \pm 12$	$(1.07 \pm 0.01) \cdot 10^8$
220	95.19	$8745 \pm 13$	$333 \pm 19$	$(1.76 \pm 0.02) \cdot 10^8$

Table 5.3: RPC2 - effective resistance at different ABS values.

The resistance value can be derived by fitting the  $(\text{dose}, R_{\text{eff}})$  curve using Formula (50), leaving  $R$ ,  $D0$  and  $\beta$  as a fit parameters. Results are shown in Figure (??). The resistance values for RPC0 and RPC2 under high irradiation condition are

$$R_{0,fit} = (2.5 \pm 0.9) \cdot 10^6 \Omega \quad R_{2,fit} = (7.58 \pm 0.02) \cdot 10^6 \Omega$$

The resistance error for RPC0 is very high (approximately one third of the estimated resistance value): this is due to the fact that the fit (applied voltage, current) curves only succeeded for  $\text{ABS} \leq 46$  for that specific RPC, so that only five (dose, effective resistance) value could be fed to fit function (50). Both values significantly differ from the first estimate value for the detectors' resistance.

### 5.5.3 The $R \cdot I$ drop

The electrodes' resistance is a fundamental parameter that plays a key role on the actual  $\Delta V$  of the gap. As discussed in chapter two, if a current  $I$  flows through the RPC gap, the applied voltage is reduced by a quantity

$$HV_{\text{drop}} = R \cdot I$$



being  $R$  the total electrodes resistance. A good knowledge on the resistance value is therefore necessary in order to evaluate the voltage drop and to establish the operative condition of the detector. The voltage drop, negligible when it comes to laboratory tests for which the flowing currents are of the order of  $0.1\mu A$ , can't be neglected for the RPCs at the GIF++ facility, since the flowing currents are of the order of  $100\mu A$ . For every ABS filter, a plot of the voltage drop versus the applied voltage is shown in Figure (5.8).

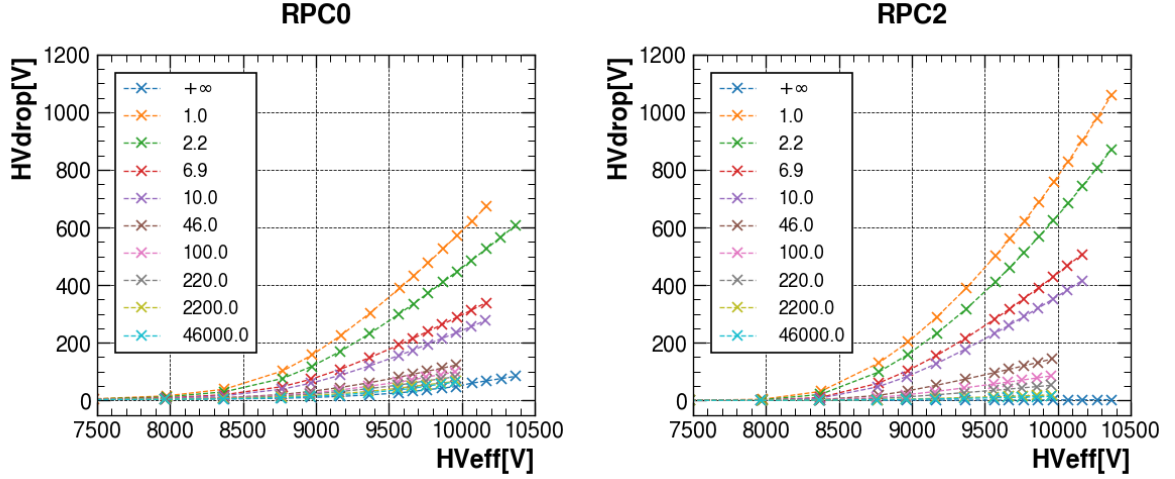


Figure 5.8: Voltage drop versus applied voltage at different attenuation filters.

The voltage drop is almost-zero for voltage values below the voltage threshold  $V_t$  for all attenuation filters; in this case, the  $HV_{gap} \sim HV_{eff}$  approximation holds. At voltage above  $V_t$ , current starts flowing, and the voltage drop can't be neglected anymore. The gap voltage is significantly different from the applied voltage, as can be seen in Figure (5.11). The blue line corresponds to the source OFF case: currents are negligible, and so is the voltage drop.  $HV_{gap}$  deviates from the blue straight line when the source is turned ON, the more deviation corresponding to the higher irradiation.

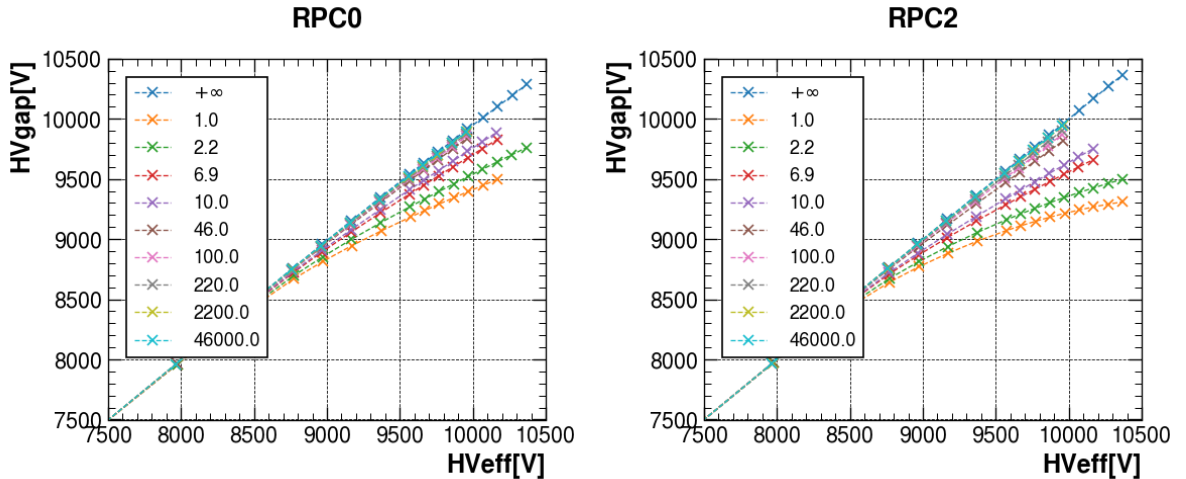


Figure 5.9:  $HV_{gap}$  value versus applied voltage at different attenuation filters.

#### 5.5.4 EcoHe20 mixture

The same filter scan operation has been performed also with the EcoHe20 gas mixture. Measured effective resistance

values are reported in Table (5.4) and (5.4). The detectors' total resistance for both RPCs is:

$$R_{0,\text{fit}} = (3.0 \pm 0.1) \cdot 10^6 \Omega$$

$$R_{2,\text{fit}} = (8.9 \pm 0.2) \cdot 10^6 \Omega$$

The results are not in perfect agreement with the standard mixture's ones; it is however worthwhile to remember that the resistivity on the bakelite electrodes depends on environmental parameters such as temperature and humidity, and that a small change in those parameters may easily induce the observed difference.

ABS	dose [ $\mu\text{Sv/h}$ ]	$V_t$ [V]	$\sigma_t$ [V]	$R_{\text{eff}}$ [ $\Omega$ ]
1.0	8778	$10146 \pm 34$	$649 \pm 29$	$(4.69 \pm 0.01) \cdot 10^6$
1.5	6990	$10158 \pm 35$	$639 \pm 30$	$(4.99 \pm 0.01) \cdot 10^6$
2.2	4137	$10152 \pm 27$	$626 \pm 28$	$(5.91 \pm 0.01) \cdot 10^6$
6.9	1573	$10224 \pm 38$	$668 \pm 35$	$(5.91 \pm 0.02) \cdot 10^6$
10	1084	$10341 \pm 49$	$733 \pm 38$	$(7.92 \pm 0.03) \cdot 10^6$

Table 5.4: RPC0 - effective resistance at different ABS values - EcoHe20 mixture.

ABS	dose [ $\mu\text{Sv/h}$ ]	$V_t$ [V]	$\sigma_t$ [V]	$R_{\text{eff}}$ [ $\Omega$ ]
1.0	8778	$10230 \pm 19$	$632 \pm 35$	$(1.05 \pm 0.03) \cdot 10^7$
1.5	6990	$10225 \pm 21$	$617 \pm 33$	$(1.12 \pm 0.03) \cdot 10^7$
2.2	4137	$10224 \pm 30$	$591 \pm 30$	$(1.26 \pm 0.03) \cdot 10^7$
6.9	1573	$10180 \pm 34$	$524 \pm 25$	$(1.78 \pm 0.03) \cdot 10^7$
10	1084	$10165 \pm 37$	$505 \pm 24$	$(2.14 \pm 0.03) \cdot 10^7$
46	301	$10119 \pm 33$	$422 \pm 18$	$(4.99 \pm 0.07) \cdot 10^7$
100	173	$10159 \pm 33$	$460 \pm 19$	$(7.8 \pm 0.1) \cdot 10^7$
220	114	$10215 \pm 31$	$499 \pm 23$	$(1.15 \pm 0.03) \cdot 10^8$

Table 5.5: RPC2 - effective resistance at different ABS values - EcoHe20 mixture.

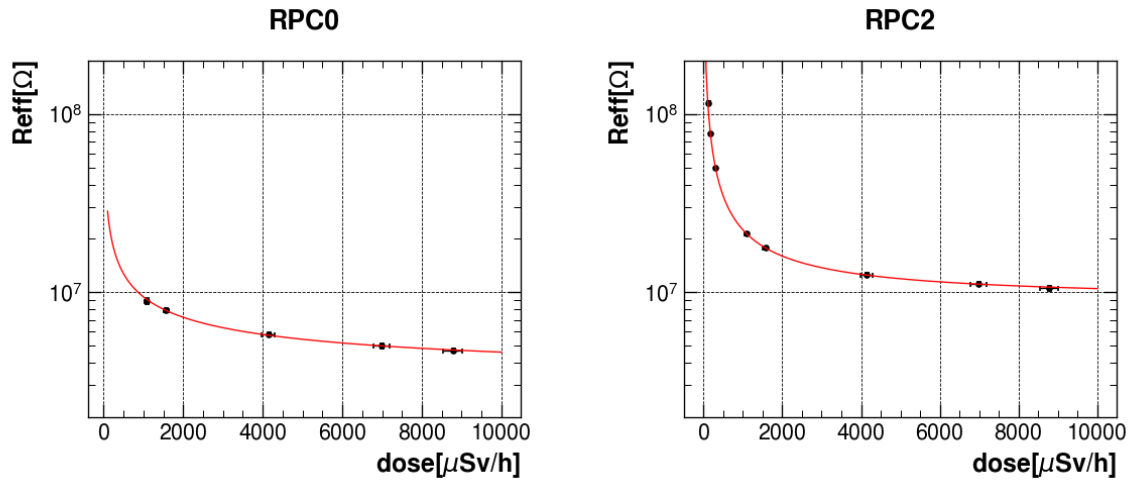


Figure 5.10: Effective resistance fit for RPC0 (left) and RPC2 (right).

EcoHe20 mixture working point, as was seen in chapter 4, is around 10800V. Both RPCs can't reach the working point value for maximum applied voltage of 11400V if nominal ABS below 6.9 are applied. In the standard operating conditions ( $HV_{\text{eff}} = 11300\text{V}$ , ABS 2.2) RPCs are working at  $\sim 100\text{V}$  below the working point, i.e. close to the knee voltage value. The  $R \cdot I$  drop is higher on RPC2, which has lower currents but a higher resistance value.

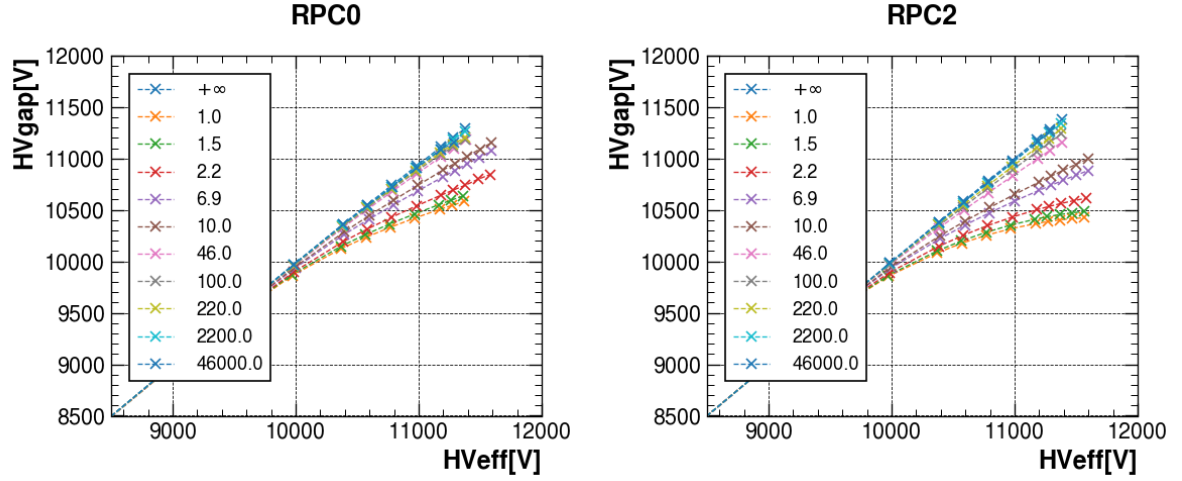


Figure 5.11:  $HV_{gap}$  value versus applied voltage at different attenuation filters.

### 5.6 Performance stability

In order to check the detector's performance stability over time, both chambers were kept ON at the same effective voltage

$$HV_{\text{eff,EcoHe20}} = 11300V$$

which results in effective gap voltages  $HV_{\text{gap},0} \sim 10700V$  and  $HV_{\text{gap},2} \sim 10600V$  for RPC0 and RPC2 respectively.

In the next paragraphs, a detector will be referred to as **ON** if its effective voltage is 11300V.

A raw plot of the current collected by RPC2 over a two month period of operation is reported in Figure (5.12). No filters have been applied, so that the plotted current corresponds to a variety of different situations: detector ON, detector OFF, source OFF, source ON, different ABS filters. The plot is reported just as an example, as no information can be extracted without selecting data corresponding to the same operative conditions.

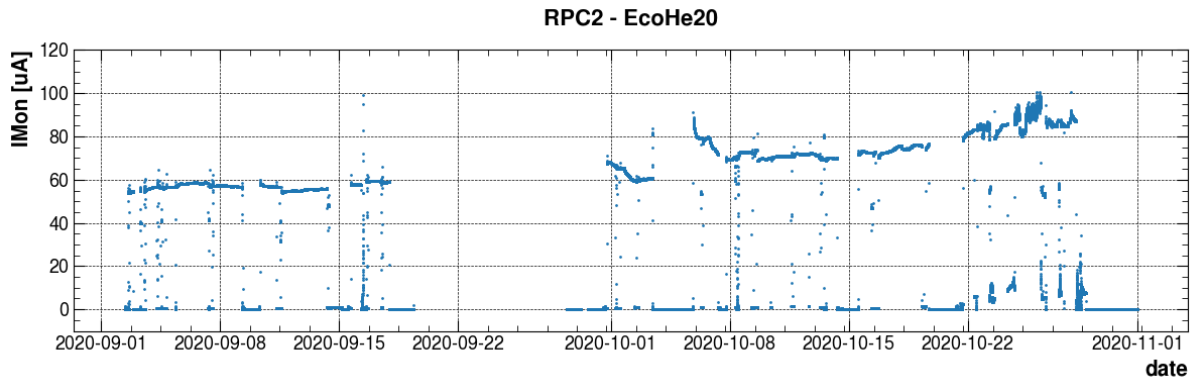


Figure 5.12: Current flowing through RPC2 - EcoHe20 mixture - no data filter applied.

### 5.7 Source ON - detector ON - ABS 2.2

The same plot, with applied filters (source ON, detector ON, ABS = 2.2) is shown in Figure (5.13). Interruptions in the current curve correspond mainly to source OFF periods for short bunker accesses for inside bunker operation (new detectors installation by other groups, maintenance procedures; long stop for facility maintenance in the second half of September). Three things can be noticed by the ON-ON-2.2 currents plot:

- an average current increase, from  $\sim 55\mu A$  to  $\sim 85\mu A$ ; this phenomenon, which is as a matter of fact the ageing problem of interest, will be addressed last, as it requires more attention;
- small drops and jumps ( $\sim 2-3\mu A$ ) after a source OFF period; this, as will be better explained shortly, is due to the change in the shadowing of the detector by other setups placed between the source and the detector itself;
- small oscillations ( $\sim 2-3\mu A$ ) in the same source ON window; these oscillation are the effect of changes of environmental value, which affect the gap voltage drop.

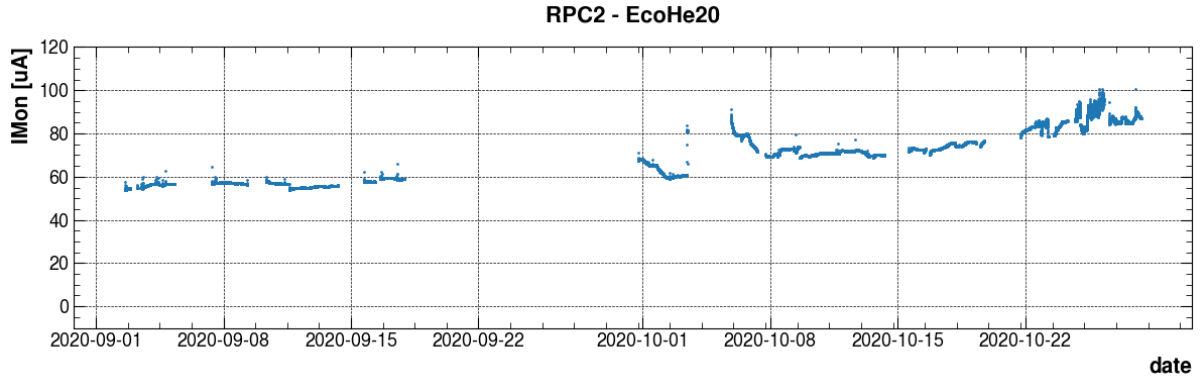


Figure 5.13: Current flowing through RPC2 - EcoHe20 mixture - source ON, detector ON, ABS = 2.2.

### 5.7.1 Shadowing from other setups

To better address shadowing and environmental related changes in the RPCs current, a shorter time window has been selected (2020/09/08 to 2020/09/15). A drop in the flowing current can be seen on 2020/09/11, with currents dropping from  $57\mu A$  to  $54\mu A$  after a short bunker access. During the access, the setup between the source and RPC2 changed, as it can be seen in Figure (5.15): the source, located on the left border of the pictures, emits in the left-to-right direction; RPCs under irradiation are highlighted with a red square; the setup between the source and the RPCs (green square) changed significantly during the bunker access. Changes in the setup, and therefore in measure currents, could not be avoided since the GIF++ bunker is a shared space, where multiple tests from different groups are performed at the same time. An increase in the shadowing results in a lower photon flux intensity, i.e. in the observed current drop.

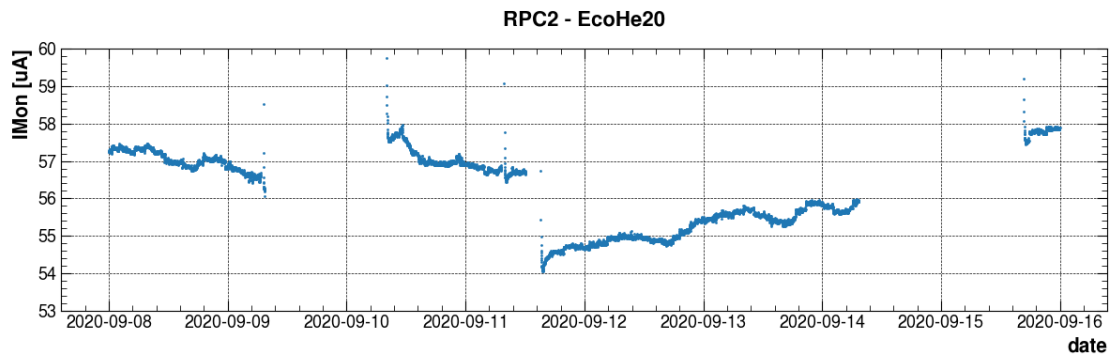


Figure 5.14: Effects of different shadowing on RPC2 current - EcoHe20 mixture - source ON, detector ON, ABS = 2.2.

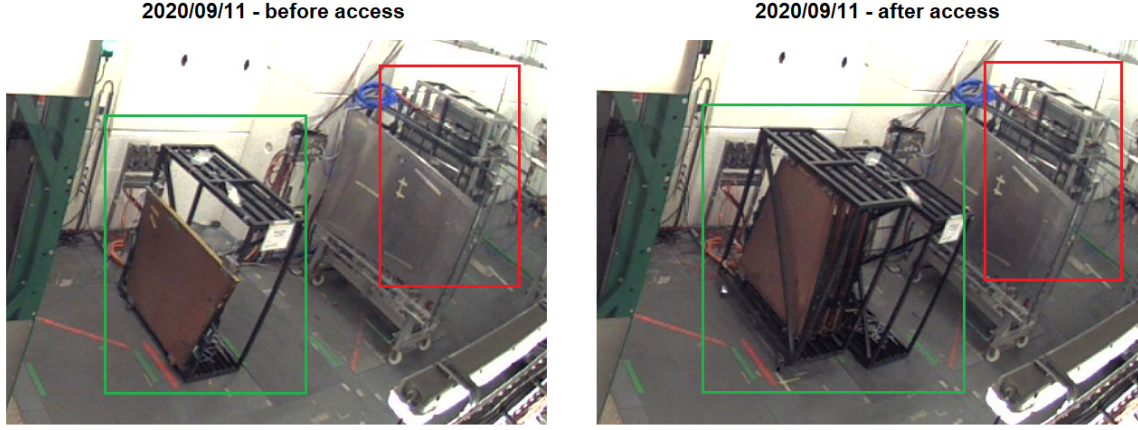


Figure 5.15: Change of setup between the source and the detectors after a bunker access.

### 5.7.2 Environmental effects

An even shorter time window (2020/09/11 after access, 2020/09/14) will be used to describe the environment-related oscillation in the observed current. The temperature inside the GIF++ bunker is controlled, with maximum variation of the order of 0.1 K. Pressure variations, on the other hand, are of the order of 10 mbar over time. A rough estimate of the temperature and pressure effects magnitude in Formula (53) can be done by evaluating the maximum relative change in the environmental parameters, which for the selected time window is:

$$\frac{\max(\Delta T)}{T_0} = \frac{0.1}{293.15} = 3 \cdot 10^{-4} \quad \frac{\max(\Delta p)}{p_0} = \frac{10}{965} = 1 \cdot 10^{-2}$$

The pressure change inside the bunker usually has a magnitude 30 times higher than the temperature effect, which can be neglected in a first approximation. Figure (5.16) shows the current change in the selected time window. Current, pressure and applied voltage follow the same trend. The pressure change influences the RPC current the following way:

- a pressure change in the bunker pressure is detected;
- the applied voltage is corrected using Formula (53), in order to have a constant effective voltage;
- an increase in the measured current is seen, since the flowing current is linear in the applied voltage (the RPC is in the saturation region after the threshold value  $V_t$ ).

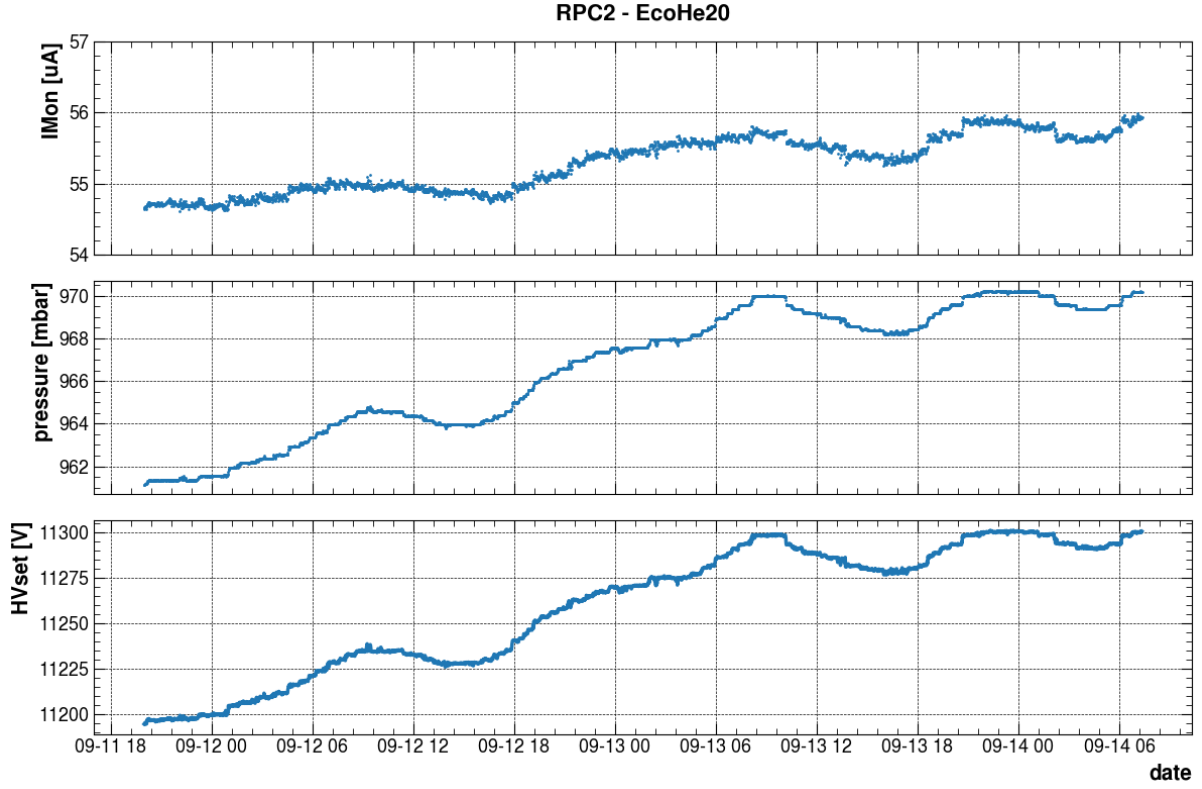


Figure 5.16: Pressure effect on RPC2 voltage and current - EcoHe20 mixture - source ON, detector ON, ABS = 2.2.

### 5.7.3 Current stability - RPC2

The current variation over time, plotted as a current versus date line as done before, gives a limited overview on the effective time for which the detector has been ON. A better measure of the amount of operational time a detector was operated with a certain mixture is given by the integrated charge, defined as

$$Q_{int}(t) = \left( \int_0^t I_{Mon}(t') dt' \right) / A \quad (54)$$

being  $A$  the detector's area. A comparison between the ageing with different mixtures is usually done in terms of current variation versus the integrated charge. The measured current versus integrated charge is shown in Figure (5.17). Starting from  $I_2 = 56.16 \mu\text{A}$ , the observed current grows linearly up to  $I_2 = 87.16 \mu\text{A}$  over a  $22.44 \text{ mC/cm}^2$  integrated charge span. A discontinuity in the linear trend can be seen for  $Q_{int}$  between 8.5 and 10  $\text{mC/cm}^2$ , but it corresponds to a two-days long test during which the voltage correction was removed, fixing the value of  $HV_{set}$  to 11300 V, which resulted in  $HV_{eff} \sim 11450 \text{ V}$  for all the short test length. The average current increase per integrated charge is:

$$\overline{\Delta I_2} = \frac{\Delta I_2}{\Delta Q_2} = \frac{87.16 - 56.16}{22.44} \frac{\mu\text{A}}{\text{mC/cm}^2} = 1.29 \frac{\mu\text{A}}{\text{mC/cm}^2} \quad (55)$$

### 5.7.4 Current stability - RPC0

The opposite trend is observed for RPC0, as it can be seen from Figure (5.18). The trend is again linear, with the same deviation from linearity corresponding to the short test mentioned before (which corresponds to  $\sim 200 \text{ mC/cm}^2$  for RPC0) and with almost vertical current variations occurring from time to time this vertical variations correspond to a rapid increase in currents when the source status is changed from OFF to ON; they happen every

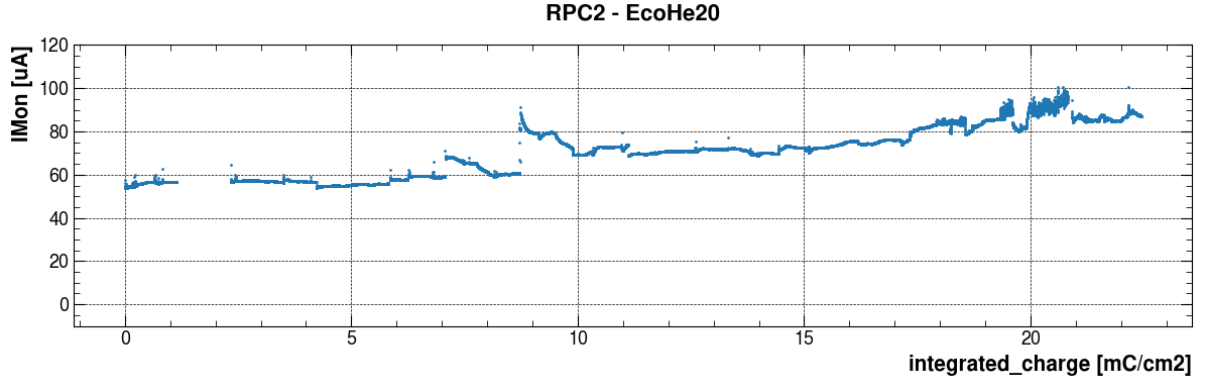


Figure 5.17: Current flowing through RPC2 - EcoHe20 mixture - source ON, detector ON, ABS = 2.2.

time the source is turned ON and the detector is already ON too, but the corresponding data was filtered to achieve a better interpretability of the plot. Given the particular data structure in which GIF++ parameters are saved, it is however very difficult to filter turn-ON currents when the ON-OFF-ON transition is too fast. The measured current decreases in time, with an average decrease of

$$\overline{\Delta I_0} = \frac{\Delta I_0}{\Delta Q_0} = \frac{260.8 - 349.5}{289.5 - 102.1} \frac{\mu A}{mC/cm^2} = -0.47 \frac{\mu A}{mC/cm^2} \quad (56)$$

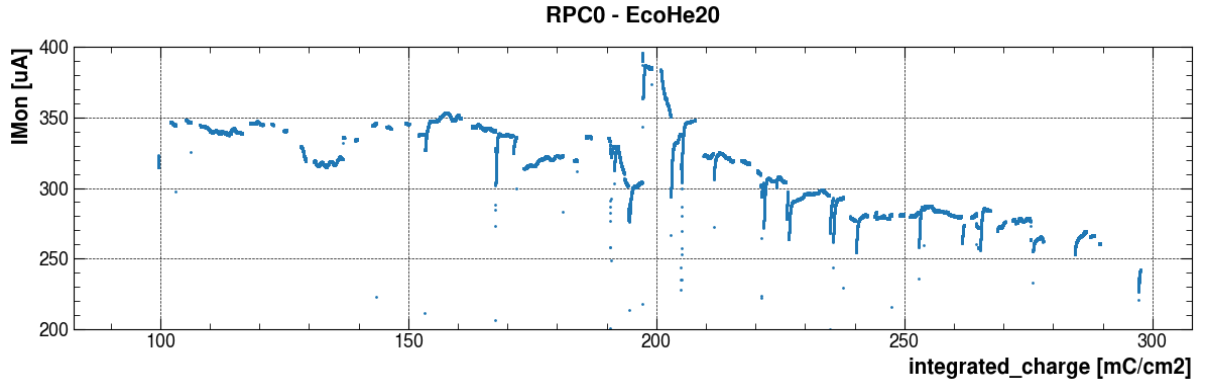


Figure 5.18: Current flowing through RPC0 - EcoHe20 mixture - source ON, detector ON, ABS = 2.2.

Firstly, RPC0 and RPC2 have different electrodes with different properties; the electrodes' resistance, for instance, was shown to be  $\sim 3$  times higher for RPC2. Secondly, RPC2 was installed in the GIF++ bunker when measurements with EcoHe20 mixture began, while RPC0 had already been in place for years, and has nonzero starting integrated charge. Both RPCs behaviour is still under investigation.

### 5.8 Performance stability - source OFF

Voltage scans were done weekly to check the detector status. The procedure is exactly the same one followed during the filter scans done to measure the detectors' resistance, with the difference that the source is OFF and the model for RPCs in high irradiation condition doesn't hold in this case. The current versus voltage curve, however, has roughly the same shape as the high rate model, with a flat part corresponding to voltages under a certain threshold value and growing linearly with the applied voltage if the applied voltage is high enough. Two different quantities were monitored:



- **ohmic currents**, measured at a voltage value well below the threshold value; the gas mixture can be considered as: totally insulant, so that the measured current (if it existed) was totally flowing through the spacers; in order to check the stability of ohmic currents, currents measured a fixed value of applied voltage (HV = 4000V) were taken as a reference value;
- **physics current**, measured at HV = 11000V for the EcoHe20 mixture, so that the detector was ON and the gas resistivity was lower than the spacers' one.

### 5.8.1 Ohmic current

A plot of the Ohmic current value over time for RPC0 is shown in Figure (5.19). The measured value is not constant, but spans a  $3\mu A$  range. Several attempts to correlated the ohmic current value to all the measured environmental parameters (pressure, temperature, humidity) were done, but the change reason could not be found and it is still under investigation.

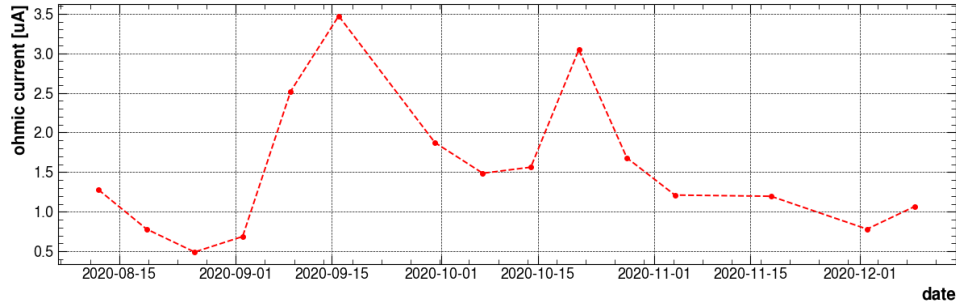


Figure 5.19: Ohmic current RPC0 - EcoHe20 mixture - source OFF, weekly scan.

As for RPC2, ohmic currents were observed to have a stable zero value for all the HVscans.

### 5.8.2 Physics current

RPC2 physics currents were stable, with a stable at  $I=0.6\mu A$  in all the source OFF scans.

Physics current for RPC0 were found to be somehow correlated with the irradiation. Figure (5.20) shows the measured physics current and the *weekly irradiation*, defined as the sum over a week (between consequent source OFF scans) of the irradiation time with detector ON, weighted by the effective attenuation:

$$w.i.(week(n)) = \left( \sum_{ABS} \frac{time\_ON(ABS)}{effective\_attenuation(ABS)} \right) |_{week(n-1)} \quad (57)$$

The difference between physics currents measured in consecutive weeks were found to be correlated to the difference between the corresponding week irradiation, as shown in Figure (5.20): a linear correlation can be seen, with the only point off-correlation corresponding to the first week of EcoHe20 operation.



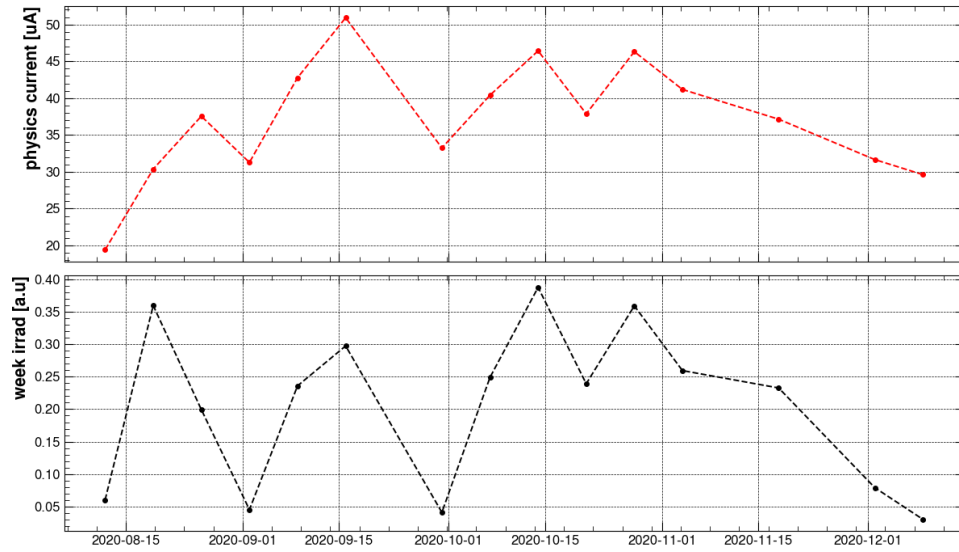


Figure 5.20: Physics current RPC0 - EcoHe20 mixture - source OFF, weekly scan (above); weekly irradiation (below).

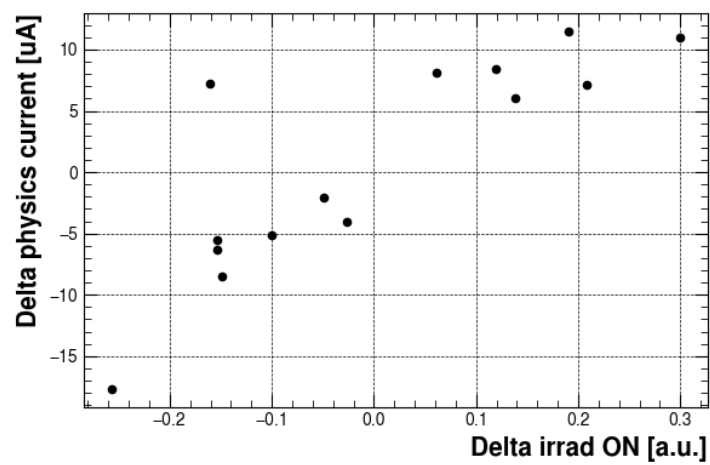


Figure 5.21: Correlation between physics current and weekly irradiation - RPC0 - EcoHe20 mixture.

## CONCLUSIONS

---

Gaseous detectors are widely used in the LHC experiments for tracking, trigger and particle identification. Among all the used gaseous detectors, Resistive Plate Chambers (RPC) dominate the overall greenhouse gas (GHG) emissions from particles detectors at CERN, because of their total volume ( $15 \text{ m}^3$ ) and presence of leaks at the detector level that are being repaired in LS2. Indeed, the RPC detector systems at LHC are operated with a gas mixture made of three components:  $\sim 95\%$   $\text{C}_2\text{H}_2\text{F}_4$  (also known as R-134a),  $\sim 4.5\%$   $\text{iC}_4\text{H}_{10}$  and  $\sim 0.3\%$   $\text{SF}_6$ . The  $\text{C}_2\text{H}_2\text{F}_4$  and  $\text{SF}_6$  are greenhouse gases with a Global Warming Potential (GWP) of 1430 and 23900 respectively. Such gases are subjected to European regulations aiming at reducing their emission either by limiting the amount of F-gases that can be sold in the European Union and by banning their use where lower GWP alternatives are available. The search for new environmentally friendly gas mixtures that are compatible with the current ATLAS and CMS RPC systems is therefore determined by the need of lowering GHG emissions and, obviously, of finding alternatives to gases that could disappear in the future. The work presented in this thesis concerns the characterization of the RPC performance with new environmentally friendly gas mixtures with a low GWP.

In the first part of the work, low GWP mixtures were characterized in laboratory conditions. The  $\text{C}_2\text{H}_2\text{F}_4$  was partially replaced either by an inert gas (He) or by  $\text{C}_3\text{H}_2\text{F}_4$  (also known as R-1234ze), a gas in the family of the HydroFluoroOlefin (HFO), which has already been identified by the refrigerant industry as a suitable low GWP alternative to the R-134a. A second test was performed by replacing the  $\text{SF}_6$  in the R-134a based mixtures with two gases of the Novec family:  $3\text{M}^{\text{TM}}$  Novec $^{\text{TM}}$ 4710 (N4710) and  $3\text{M}^{\text{TM}}$  Novec $^{\text{TM}}$ 5110 (N5110), which have high electronegativity and low GWP (2100 and less than 1, respectively). The main results obtained are:

- The two promising low GWP gas mixture mixtures are made of 20% or 30% He, 4.5%  $\text{iC}_4\text{H}_{10}$ , 0.6%  $\text{SF}_6$  and the rest  $\text{C}_2\text{H}_2\text{F}_4/\text{C}_3\text{H}_2\text{F}_4$  in equal proportions. These gas mixtures show a shift in the mixture's working point and streamer probabilities higher than the standard one, but still in an acceptable range.
- Novec4710 was proven to be a valid alternative to  $\text{SF}_6$  in laboratory conditions. N4710 based mixtures show streamer probabilities comparable to the standard one for N4710 concentrations between 0.1% and 0.7%. In such a range, the RPC's foremost parameters don't show a clear dependence on the concentration, with the exception of the mixture working point, which increases with the N4710 concentration. The  $\text{C}_2\text{H}_2\text{F}_4/\text{iC}_4\text{H}_{10}/\text{N4710}$  95.4/4.5/0.1 mixture has a working point very close to the one of the standard mixture and most of the RPC performances are very similar to the ones of the standard mixture.
- Novec5110, with GWP lower than 1, is the most effective for the GHG emission reduction scope. Nevertheless, it is liquid at room temperature and it is therefore difficult to handle, as it requires a pre-heating process before it can be injected into the mixture. N5110 was tested with concentrations between 0.3% and 2.0%. The best results in terms of streamer probability are obtained with the highest concentration, but the streamer probability is still two times higher than the standard mixture's one. Further increase in concentration is limited by the mixture's working point, which increases of  $\sim 500\text{V}$  per N5110 percentage point.

The second part of the work consisted in the validation of long-term operation of RPC detectors operated with the  $\text{C}_2\text{H}_2\text{F}_4/\text{C}_3\text{H}_2\text{F}_4/\text{He}/i\text{C}_4\text{H}_{10}/\text{SF}_6$  37.45/37.45/20/4.5/0.3 mixture in high irradiation conditions at the Gamma Irradiation Facility (GIF++), where a 12.2 TBq  $^{137}\text{Cesium}$  source provides an intense gamma background field, allowing to accumulate doses equivalent to the ones expected for the High Luminosity phase of LHC in reasonable time. Two detectors were installed and tested with this gas mixture.

- The first RPC was already installed in the GIF++ bunker before this test started and it was already operated with high irradiation background for a few years with different gas mixtures. At the start of the test, detector currents were already a factor 4 higher than the ones of the other RPC tested. The trend of the currents show a decrease over time of about 20%, which is still not completely understood. An interesting behaviour can be seen in the physics currents obtained during the source OFF scans: these currents highly depend on the irradiation condition of the last period.
- The second RPC was installed in the GIF++ at the beginning of the validation process of the gas mixture. Currents were stable in a first period. After an operation period of about one month a slight increase was observed, but the ohmic and physics current measured during source OFF remained stable.

The detector operation with the He-HFO based gas mixture will continue during the next months at the GIF++. Given the limited time period of the test and the accumulated charge, it is too early to draw any conclusion.



## References

- [1] E. Mobs, “The CERN accelerator complex - August 2018. General Photo. URL: <https://cds.cern.ch/record/2636343>.
- [2] D. Barney, “CMS Detector Slice”. CMS Collection. January 2016. URL: <https://cds.cern.ch/record/2120661>.
- [3] D. Griffiths, Introduction to Elementary Particles, 2nd Revised Edition, October 2008.
- [4] The CMS Collaboration. “Observation of the diphoton decay of the Higgs boson and measurement of its properties”, In: (2014) URL: <https://doi.org/10.1088/1748-0221/9/01/C01053>.
- [5] The ATLAS Collaboration. “Observation of a new particle in the search for the Standard Model Higgs boson with the ATLAS detector at the LHC”. In: (2012). URL: <https://doi.org/10.1016/j.physletb.2012.08.020>.
- [6] R. Guida et al. “The gas systems for the LHC experiments”. In: IEEE Nuclear Science Symposium Conference Record (January 2013). URL: <https://doi.org/10.1109/NSSMIC.2013.6829415>
- [7] C. De Melis. “Timeline for the LHC and High-Luminosity LHC. Frise chronologique du LHC et du LHC haute luminosité”. In: (October 2015). General Photo. URL <http://cds.cern.ch/record/2063307>
- [8] C. Gemme. “The ATLAS upgrade program”. In: Proceedings, 2nd Conference on Large Hadron Collider Physics Conference (LHCP 2014): New York, USA, June 2-7, 2014. URL: <http://www.slac.stanford.edu/econf/C140602.2/papers/1409.5002v1.pdf>
- [9] CMS Collaboration. The Phase-2 Upgrade of the CMS Muon Detectors, CERN-LHCC-2017-012; CMS-TDR-016 22/10/2018. URL: <http://cds.cern.ch/record/2283189?ln=en>
- [10] J. Andrews, N. Jelley, Energy science: principles, technologies, and impacts, Third Edition, June 2017.
- [11] R Guida, M Capeans, B. Mandelli. “Gas Systems for Particle Detectors at the LHC Experiments: Overview and Perspectives”. In: Springer Proc. Phys. 212 (2018). URL: <http://cds.cern.ch/record/2649531>
- [12] Regulation (EU) No 517/2014 of the European Parliament and of the Council of 16 April 2014 on fluorinated greenhouse gases and repealing Regulation (EC) No 842/2006 Text with EEA relevance”. In: (May 2014).
- [13] M. Corbetta, R. Guida, B. Mandelli, G. Rigoletti. "Gas RD on gas recirculation and recuperation for the Resistive Plate Chamber detectors", October 2020. URL: <https://iopscience.iop.org/article/10.1088/1748-0221/15/10/C10028>
- [14] URL: <https://cds.cern.ch/record/117989> F. Sauli. “Principle of operation of multiwire proportional and drift chamber”, Lectures given in the academic training program of CERN, 1977
- [15] H. Raether. Electron Avalanches and Breakdown in Gases, 1964.
- [16] W. Riegler, C. Lippmann, R. Veenhof. Detector Physics and Simulation of Resistive Plate Chambers, Nucl. Instrum. Methods Phys. Res., A 500 (2003) URL: <http://cds.cern.ch/record/570462>
- [17] M. Abbrescia, V. Peskov, P. Fonte, Resistive Gaseous Detectors, Designs, Performance and Perspectives, April 2018.
- [18] M .Abbrescia et al., “Resistive Plate Chambers in avalanche mode: a comparison between model prediction and experimental results”, Nucl. Instr. and Meth. A409 (1998).

- [19] V. Koreshev et al. "Operation of narrow gap RPC with tetrafluoroethane-based mixtures". In: Nucl. Instrum. Meth. A456 (2000)
- [20] G. Carboni et al., "A model for RPC detectors operating at high rate URL: [https://doi.org/10.1016/S0168-9002\(02\)02082-X](https://doi.org/10.1016/S0168-9002(02)02082-X)
- [21] R. Santonico. "Topics in resistive plate chambers". In: Resistive plate chambers and related detectors. Proceedings, 3rd International Workshop, Pavia, Italy, October 1995.
- [22] McKinney W et al., Data structures for statistical computing in python. In: Proceedings of the 9th Python in Science Conference (2010).
- [23] M. Abbrescia et al., Cosmic ray tests of double-gap resistive plate chambers for the CMS experiment, Nucl. Instrum. Meth. A 550 (2005) 116.
- [24] 3M<sup>TM</sup> Novec<sup>TM</sup> 4710 datasheet. <https://multimedia.3m.com/mws/media/11321240/3m-novec-4710-insulating-gas.pdf>
- [25] 3M<sup>TM</sup> Novec<sup>TM</sup> 5110 datasheet. <https://multimedia.3m.com/mws/media/11321230/3m-novec-5110-insulating-gas.pdf>
- [26] Mirion Dosimeter Datasheet. URL: [https://mirion.s3.amazonaws.com/cms4\\_mirion/files/pdf/spec-sheets/20996078\\_rds31\\_en\\_f.pdf?1560783263](https://mirion.s3.amazonaws.com/cms4_mirion/files/pdf/spec-sheets/20996078_rds31_en_f.pdf?1560783263)
- [27] "RPC  $\gamma$  sensitivity simulation, Nuclear Instruments and Methods in Physics Research Section A: Accelerators, Spectrometers, Detectors and Associated Equipment Volume 456, 21 December 2000